Bio-optical characterization of the Salish Sea, Canada, towards improved chlorophyll algorithms for MODIS and Sentinel-3

by

Stephen Robert Phillips
BSc, University of Victoria, 2008
BSc, University of Victoria, 2013

A Thesis Submitted in Partial Fulfillment
of the Requirements for the Degree of

Master of Science

in the Department of Geography

Bio-optical characterization of the Salish Sea, Canada, towards improved chlorophyll algorithms for MODIS and Sentinel-3

by

Stephen Robert Phillips
BSc, University of Victoria, 2008
BSc, University of Victoria, 2013

Supervisory Committee

Dr. Maycira Costa (Department of Geography)
Supervisor

Dr. David Atkinson (Department of Geography)
Committee Member

Abstract

Supervisory Committee

Dr. Maycira Costa (Department of Geography)
Supervisor

Dr. David Atkinson (Department of Geography)
Committee member

The goal of this research was to improve ocean colour chlorophyll a (Chl$a$) retrievals in the coastal Case 2 waters of the Salish Sea by characterizing the main drivers of optical variability and using this information to parameterize empirical algorithms based on an optical classification. This was addressed with three specific objectives: (1) build a comprehensive spatio-temporal data set of *in situ* optical and biogeochemical parameters, (2) apply a hierarchical clustering analysis to classify above-water remote sensing reflectance (R_{rs}) and associated bio-optical regimes, (3) optimize and validate class-specific empirical algorithms for improved Chl$a$ retrievals.

Biogeochemical and optical measurements, acquired at 145 sites, showed considerable variation; Chl$a$ (mean=1.64, range: 0.10 – 7.20 µg l^{-1}), total suspended matter (TSM) (3.09, 0.82 – 20.69 mg l^{-1}), and absorption by chromophoric dissolved organic matter ($a_{cdom}(443)$) (0.525, 0.007 – 3.072 m^{-1}), thus representing the spatial and temporal variability of the Salish Sea. A comparable range was found in the measured optical properties; particulate scattering ($b_p(650)$) (1.316, 0.250 – 7.450 m^{-1}), particulate backscattering ($b_{bp}(650)$) (0.022, 0.005 – 0.097 m^{-1}), total beam attenuation coefficient ($c_t(650)$) (1.675, 0.371 – 9.537 m^{-1}), and particulate absorption coefficient ($a_p(650)$) (0.345, 0.048 – 2.020 m^{-1}). Empirical orthogonal function (EOF) analysis revealed 95% of the R_{rs} variance was highly correlated to b_p (r = 0.90), b_{bp} (r = 0.82), and TSM concentration (r = 0.80), suggesting a strong influence from riverine systems in this region. Hierarchical clustering on the normalized R_{rs} revealed four spectral classes. Class 1 is defined by high overall R_{rs} magnitudes in the red, indicating more turbid waters, Class 2 showed high R_{rs} values in the red and well defined fluorescence and absorption features, indicated by a high Chl*a* and TSM presence, Class 3 showed low TSM influence and more defined Chl*a* signatures, and Class 4 is characterized by overall low R_{rs} values, suggesting more optically clear oceanic waters. Spectral similarities justified a simplification of this classification into two dominant water classes – (1) estuarine class (Classes 1 and 2) and (2) oceanic class (Classes 3 and 4) – representing the dominant influences seen here.

In situ Chl*a* and above-water remote sensing reflectance measurements, used to validate and parameterize the OC3M/OC3S3, two-band ratio, FLH and, modified FLH (ModFLH) empirical algorithms, showed a systematic overestimation of low Chl*a* concentrations and underestimation of higher Chl*a* values for all four algorithms when tuned to regional data. FLH and ModFLH algorithms performed best for these data (R^2 ~ 0.40; *RMSE* ~ 0.32). Algorithm accuracy was significantly improved for the class-specific parametrizations with the two-band ratio showing a strong correlation to the Chl*a* concentrations in the estuarine class (R^2 ~ 0.71; *RMSE* ~ 0.33) and the ModFLH algorithm in the oceanic class (R^2 ~ 0.70; *RMSE* ~ 0.26). These results demonstrated the benefit of applying an optical classification as a necessary first step into improving Chl*a* retrievals from remotely sensed data in the contrasted coastal waters of the Salish Sea. With accurate Chl*a* information, the health of the Salish Sea can be viably monitored at spatial and temporal scales suitable for ecosystem management.

Table of Contents

Supervisory Committee **ii**

Abstract **iii**

Table of Contents **v**

List of Tables **vi**

List of Figures **vii**

List of Symbols **ix**

Acknowledgments **xii**

Dedication **xiii**

1 Introduction **1**

2 Optical Classification of Coastal Waters in the Salish Sea, Western Canada **6**

2.1 Abstract 6

2.2 Introduction 7

2.3 Methods 13

2.4 Results 24

2.5 Discussion 38

2.6 Conclusion 46

3 Regional chlorophyll-a algorithm evaluation for MODIS-Aqua and Sentinel-3 in the Salish Sea, Western Canada **49**

3.1 Abstract 49

3.2 Introduction 50

3.3 Data collection and methods 57

3.4 Results 64

3.5 Discussion 80

3.6 Conclusion 88

4 General Conclusion **91**

5 Bibliography **96**

List of Tables

Table 2-1 Summary of *in situ* data collected during field cruises and associated equipment. 15

Table 2-2 *In situ* bio-optical parameters separated into spring (Feb – May), summer (June – Sept) and fall (Oct – Nov) seasons. Average in bold, standard deviation in brackets, and minimum and maximum values in square brackets. 26

Table 2-3 *In situ* bio-optical variables separated into classes 1 - 4. Average in bold, standard deviation in brackets, and minimum and maximum values in square brackets. Largest average bio-optical variable is highlighted for each class. 36

Table 3-1 Empirical algorithms tested in this study. 61

Table 3-2 Summary of in situ bio-optical variables measured and separated into estuarine and oceanic classes. Average in bold, standard deviation in brackets, and minimum and maximum values in square brackets. 65

Table 3-3 Summary of the empirical models developed using regional data (n = 142) to form regression equations (X) with in situ Chl*a*. The resulting best fit non-linear equation produces the derived Chl*a* equation shown. 68

Table 3-4 Summary of the empirical algorithms developed using class specific data sets for estuarine (n = 19) and oceanic class (n = 124) data to form the regression equation (X) with *in situ* Chl*a*. The resulting non-linear best fit equation produces the Chl*a* equation shown. 70

Table 3-5 Statistical results of the empirical algorithms using the regional data. .. 72

Table 3-6 Statistical results of the empirical algorithms using the class specific data. 77

List of Figures

Figure 2-1 Map showing the spatial distribution of the current data set in the Salish Sea. ... 11

Figure 2-2 Flow chart outlining the methods for (a) data collection and (b) data analysis. ... 14

Figure 2-3 Fraser River discharge for September 2012 - December 2013 (Environment Canada, 2014) with field sampling shown as solid red bars. ... 25

Figure 2-4 Inherent optical properties (IOPs) for typical (a) plume water (Stn 073), (b) transitional water (Stn 069), and (c) oceanic water (Stn 081) all measured in June 2013. ... 27

Figure 2-5 (a) Remote sensing reflectance, $R_{rs}(\lambda)$, in sr^{-1} for the five DFO cruises, bi-weekly ferry cruises and modelled values, (b) Normalized $R_{rs}(\lambda)$ to the integral. *In situ* values are in grey, Hydrolight modelled values are dashed, and average values are shown in red. ... 28

Figure 2-6 Correlation between measured in situ $R_{rs}(\lambda)$ spectra and modelled $R_{rs}(\lambda)$ using Hydrolight. R^2 is shown as closed circles and slopes are triangles. ... 29

Figure 2-7 Loadings and percent variance for the first three modes of the EOF analysis of R_{rs}. ... 30

Figure 2-8 Correlation coefficients calculated between the EOF amplitude factors and the measured *in situ* biogeochemical and bio-optical parameters for EOF modes 1-3. ... 31

Figure 2-9 $R_{rs}(\lambda)$ spectra derived from an unsupervised hierarchical classification of *in situ* and simulated data with 4 classes (a-d). For each class (e) average normalized $R_{rs}(\lambda)$ and (f) average $R_{rs}(\lambda)$. ... 34

Figure 2-10 Spatial distribution of Classes 1-4 for spring, summer and fall. ... 36

Figure 3-1 Sample R_{rs} spectra showing the fluorescence line height (FLH) and bands centered around the fluorescence peak, which were used in the modified FLH algorithm. Grey vertical bars denote the minimum and maximum boundaries for the bands of Sentinel-3 (S) and MODIS (M). ... 56

Figure 3-2 Study area map showing spatial distribution of the Chl*a* data set in the Salish Sea. Values for Chl*a* concentrations are shown as proportional symbols. 58

Figure 3-3 $R_{rs}(\lambda)$ spectra for (a) estuarine class and (b) oceanic class. Averages for each class are shown as red dashed lines. 66

Figure 3-4 Class-specific reflectance-based algorithm results for (a) estuarine class waters and (b) oceanic class waters. MODIS values are shown in gray, Sentinel-3 values in black. Note the shown relationships are the most significant relationships and do not include all algorithms in the analysis. 69

Figure 3-5 Linear regression between measured in situ Chl*a* values and modelled Chl*a* values that were derived with the regional data set using the four algorithms for (a-d) MODIS and (e-h) Sentinel-3. TSM concentrations for each point are shown as proportional gray symbols. 73

Figure 3-6 Linear regression between measured in situ Chl*a* values and modelled Chl*a* values that were derived with the regional data set using the four algorithms for (a-d) MODIS and (e-h) Sentinel-3. $a_{cdom}(443)$ coefficients for each point are shown as proportional symbols. 74

Figure 3-7 Error plots showing the difference between modelled Chl*a* and in situ Chl*a* for (a) OC3M/OC3S3, (b) 2-band ratio, (c) FLH and (d) ModFLH regional algorithms. 75

Figure 3-8 Linear regression between measured *in situ* Chl*a* values and modelled Chl*a* values that were derived with the *estuarine class* data set using (a) OC3M/OC3S3, (b) 2-Band Ratio, (c) FLH and (d) the Modified FLH algorithms. Corresponding error plots are shown for each algorithm (e-h). MODIS results are shown as grey circles and Sentinel-3 as black squares. 78

Figure 3-9 Linear regression between measured *in situ* Chl*a* values and modelled Chl*a* values that were derived with the *oceanic class* data set using (a) OC3M/OC3S3, (b) 2-Band Ratio, (c) FLH and (d) the Modified FLH algorithms. Corresponding error plots are shown for each algorithm (e-h). MODIS results are shown as grey circles and Sentinel-3 as black squares. 79

List of Symbols

Symbol	Name	Units
λ	wavelength	nm
a_{CDOM}	CDOM absorption coefficient without water absorption coefficient	m^{-1}
a_{cdom}	CDOM absorption coefficient	m^{-1}
a_c	CDOM absorption coefficient measured with ac-S meter	m^{-1}
a_T	measured total absorption coefficient	m^{-1}
a_t	measured total absorption coefficient without water absorption coefficient	m^{-1}
a_p	particle absorption coefficient	m^{-1}
a_w	water absorption coefficient	m^{-1}
A	absorbance	
b	scattering coefficient	m^{-1}
b_o	empirical value to describe particle scattering coefficient	
b_p	particulate scattering coefficient	m^{-1}
b_{bp}	backscattering coefficient	m^{-1}
b_0	reference scattering coefficient	m^{-1}
b_{bp}/b_p	backscattering ratio	
β	volume scattering function	$sr^{-1}m^{-1}$
β_p	particle volume scattering function	$sr^{-1}m^{-1}$
β_t	total volume scattering function	$sr^{-1}m^{-1}$
c_T	measured total beam attenuation coefficient	m^{-1}

Symbol	Name	Units
c_t	measured total beam attenuation coefficient without water beam attenuation coefficient	m^{-1}
c_w	pure water beam attenuation coefficient	m^{-1}
c_p	particulate beam attenuation coefficient	m^{-1}
d	cosine distance function	
l	path length	m
L_s	sky radiance	$\mu Wcm^{-2}sr^{-1}nm^{-1}$
L_t	total water-surface radiance	$\mu Wcm^{-2}sr^{-1}nm^{-1}$
E_s	downwelling ski irradiance	$\mu Wcm^{-2}nm^{-1}$
R_{rs}	remote sensing reflectance	sr^{-1}
r_{rs}	remote sensing reflectance below the air-water interface	sr^{-1}
S_{cdom}	CDOM absorbance slope	nm^{-1}
ρ_{sky}	proportion of sky radiance	
W	wind speed	$m\ s^{-1}$
χ_p	scaling factor to estimate particle backscattering	
θ	scalar angle	
Chl*a*	chlorophyll *a* concentration	$\mu g\ l^{-1}$
Chl*b*	chlorophyll *b* concentration	$\mu g\ l^{-1}$
$\mathrm{Chl_{alg}}$	algorithm estimated Chlorophyll *a* concentration	$\mu g\ l^{-1}$
$\mathrm{Chl_{meas}}$	measured Chlorophyll *a* concentration	$\mu g\ l^{-1}$
PIM	particulate inorganic matter	$mg\ l^{-1}$
POC	particulate organic carbon (non-elemental)	$mg\ l^{-1}$

Symbol	Name	Units
POM	particulate organic matter	mg l^{-1}
TSM	total suspended matter	mg l^{-1}
SRF	signal response function	
$RMSE_{log}$	log root mean square error	
δ	relative error	
S	slope	
I	intercept	µg l^{-1}
R^2	coefficient of determination	
R	correlation coefficient	
B	satellite sensor band	

Acknowledgments

Firstly, I would like to express my sincere gratitude to my supervisor Dr. Maycira, Costa for the opportunity to undertake this research and for her continuous support, patience and motivation during my masters study. Her guidance helped encourage me through countless aspects of this research and I have grown tremendously because of it.

Thank you to Rustin Sweeting, Chrys Neville, and Rick Beamish for generously allowing me to conduct my work on their research cruises. I would also like to thank Brian Recalma and the entire crew of the W.E. Ricker for their assistance during sampling. I learned a tremendous amount on those cruises.

I would like to extend my sincere appreciation to the various members of the Spectral Lab, including Tyson, Justin, Felipe, Jeane, and Adriana who provided an amazing support network from the very beginning of this project. Their passed down knowledge and guidance was invaluable and immensely appreciated, and I'll always remember the fun we had over the years.

Thank you to my family and friends who motivated me to pursue this academic path. A special thanks to my mother, Pamela, who kept me going through the thick and the thin. I would especially like to thank my partner Owen for his unwavering support and patients during this process. He grounded me countless times and helped me endure the more stressful moments of this project.

Funding for this research was generously provided by the joint contribution from the BCFRST NRAS Program and MEOPAR. Field and lab equipment funding was provided by the Canadian Foundation for Innovation.

Dedication

I would like to dedicate this thesis to my brother Scott. You always knew how to push me to make that leap to the unknown. You taught me to appreciate every moment, even the bad ones, and to never take anything for granted. You were my light at the end of this tunnel.

Chapter 1 **Introduction**

Coastal zones are among the most productive ecosystems in the global oceans and represent an important boundary between terrestrial and ocean ecosystems (Bierman et al., 2011; Gattuso et al., 2003). These highly productive regions serve a large portion of the earth's population (Small & Nicholls, 2003) and represent a large resource for societies, supporting 90% of the world's fisheries (Pauly et al., 2002). Consequently, these regions are under increasing pressure from anthropogenic influences such as intense fishing (Halpern et al., 2015) and invading species. Nutrient inputs from waste water discharge (Swaney et al., 2012) is another problem; this can lead to eutrophication and hypoxia (Diaz & Rosenberg, 2008; Voss et al., 2011). These problems are further compounded by rising atmospheric CO_2 levels and climate change influencing shifts in temperatures, stratification, circulation, oxygen content, and ocean acidification (Doney et al., 2012). These changes have been shown to have profound effects on phytoplankton species distributions, especially in the mid to low latitudes, where declines in phytoplankton abundance have been reported (Antoine, 2005; Behrenfeld et al., 2006; Boyce et al., 2010; Steinacher et al., 2010). It is therefore vital to monitor coastal marine ecosystems to improve our understanding of their dynamics and how they are responding to a changing human influenced environment.

Chlorophyll *a* concentration (Chl*a*) is a useful indicator of ecosystem health in the ocean and, as a major light absorbing pigment, Chl*a* is used as a proxy for phytoplankton biomass (Sauer et al., 2012) and primary productivity (Oliver, 2004). Thus, accurately measuring Chl*a* is a priority because it is an important indicator used to explain fish presence and abundance in ocean waters (Chassot et al., 2011). Traditionally, Chl*a* is measured through *in situ* sampling, which is difficult to obtain on spatial and temporal time scales suitable for research activities (Harvey et al., 2015; Masson & Peña, 2009; Mélin & Vantrepotte, 2015). One way to fill this gap in information acquisition is to employ remote sensing techniques; in particular through ocean colour (Brewin et al., 2015).

The launch of the Coastal Zone Color Scanner (CZCS) (1978-1986) initiated the use of sunlight reflected from the surface layers of sea water to gather information about ocean colour (McCain et al., 2006). Since then, efforts have gone into improving radiometric, spatial, spectral, and temporal resolutions, beginning in the United States with the Sea-viewing Wide Field-of-view Sensor (SeaWiFS), (Hooker & McClain, 2000). Following this, the Moderate Resolution Imaging Spectroradiometer (MODIS) instrument, with 1000 m spatial resolution for ocean colour, was launched on board the Earth Observing System (EOS) satellite Aqua in 2002 (Esaias et al., 1998). Also in 2002, the European Space Agency (ESA) launched the Medium Resolution Imaging Spectrometer (MERIS) on-board the ENVISAT satellite. This sensor, operational until 2012, had a spatial resolution down to 300m. A follow-up mission, the Ocean Land Colour Instrument (OLCI) onboard the Sentinel-3 satellite, is scheduled to launch in January, 2016 (Berger et al., 2012; Donlon et al., 2012).

Remotely-sensed ocean colour information is determined by relating water-leaving radiometric measurements to inherent optical properties (IOPs) and corresponding constituents within the water (Kirk, 2011). This follows radiative transfer theory which describes how energy propagates in a scattering and absorbing medium

(Mobley, 2010). The absorption and scattering properties of a medium are described by their IOPs, which are defined as properties of the medium that are inherent to the medium and do not depend on the light field. To describe the bulk optical properties, apparent optical properties (AOPs) can be measured, which are defined as properties that depend on both the IOPs of a medium and the geometric structure of the measured radiance distribution (Morel & Prieur, 1977). AOPs are related to the IOPs and corresponding constituents of a medium through the inverse solution to radiative transfer theory. In open ocean waters, referred to as Case 1, the optical properties are dominated by phytoplankton, but in optically complex coastal waters, referred to as Case 2, other constituents, such as chromophoric dissolved organic matter (CDOM) and inorganic particulates, cause significant shifts in the optical properties that are difficult to categorize because they can potentially all vary independently (Carder et al., 1999; Morel & Prieur, 1977; Tilstone et al., 2011). This has made it particularly difficult to estimate Chl*a* concentrations in turbid coastal and inland waters using spaceborne remote sensing data (Frette et al., 1998; Chen et al., 2013).

Typically, empirical algorithms based on blue/green reflectance ratios have been used as input to retrieve Chl*a* in Case 1 waters with reasonable accuracy on a global scale (e.g. Gordon & Morel, 1983; O'Reilly et al., 1998). For Case 2 waters, this approach is limited and tends to produce inaccurate results, particularly when waters are turbid (Dall'Olmo et al., 2005; Komick et al., 2009; Lavender et al., 2004; Sathyendranath et al., 1999). To overcome these limitations, regionally specific algorithms have been optimized by parameterizing and validating the AOP/IOP relationships with locally specific *in situ* bio-geochemical and optical data (e.g., Garcia et al., 2005; Gitelson et al., 2007; Le et al., 2013a; Mustapha et al., 2012; Shen et al., 2010). In these examples, the red and near-infrared spectral bands are used instead of the typical blue and green bands to minimize atmospheric interference and CDOM absorption, which are typically responsible for inaccuracies for coastal waters (Le et al., 2013b; Moses et al., 2009b). These algorithms are then parameterized with regional data to calibrate the algorithms to the localized Case 2 conditions, such as in the presence of high turbidity. This approach, however, still presents limitations such as inaccuracies due to numerous high frequency events, such as wind and tidal mixing of riverine sediments, in coastal environments and a potentially limited regional extent to match the conditions in which these data were acquired (Lubac & Loisel, 2007; Vantrepotte et al., 2012).

A more recent approach to resolve the inversion of remotely sensed data in optically complex waters is through optical classification (Le et al., 2011; Lubac & Loisel, 2007; Moore et al., 2014; Vantrepotte et al., 2012). By grouping waters with similar optical traits, or classes, algorithms can be parameterized on a class basis to reduce the inaccuracies which arise from variations in the marine optical properties (Loisel et al., 2010; Szeto et al., 2011; Woźniak et al., 2010). Through this approach it is implicitly assumed that similar optical water conditions can exist in different coastal regions, which will translate into similar reflectances (Vantrepotte et al., 2012). Therefore by developing class-based algorithms, this approach can be applied to other coastal regions with similar classifications, and extend the applicability of regionally specific algorithms to a global scale (Mélin & Vantrepotte, 2015; Vantrepotte et al., 2012).

The goal of this research was to characterize the main drivers of optical variability in the Salish Sea and use this information to improve remote-sensing retrievals of Chl*a* concentrations. Three objectives support this goal:

1. Build a comprehensive spatial and temporal *in situ* optical and biogeochemical data set for the surface waters of the Salish Sea.
2. Apply a hierarchical clustering analysis to classify above-water remote sensing reflectance data and associated bio-optical regimes.
3. Validate and parameterize class-specific empirical algorithms for deriving Chl*a* with improved accuracy in the Salish Sea.

To achieve these objectives, *in situ* IOPs (absorption, attenuation, scattering, and backscattering) were collected in the surface waters of the Salish Sea during spring, summer, and fall conditions in conjunction with water constituent concentrations from *in situ* samples. A hierarchical clustering analysis, performed on $R_{rs}(\lambda)$, defined four classes. An empirical orthogonal analysis was then applied to the bio-geochemical regimes for each class to understand the drivers of variability. These are addressed in Chapter 2. This information was then used as input in the development of class-specific reflectance-based algorithms, for MODIS-Aqua and Sentinel-3, for the retrieval of Chl*a* in which standard algorithms were parameterized to each class as a way to improve algorithm performance, shown in Chapter 3. Finally, Chapter 4 offers general conclusions and final recommendations from this research.

Chapter 2 Optical Classification of Coastal Waters in the Salish Sea, Western Canada

2.1 Abstract

Bio-optical data from the fall of 2012 to 2013 were collected from five field campaigns and bi-weekly trips aboard a ship of opportunity in the Salish Sea, west coast of Canada, to assess the spatial and temporal variability of ocean colour in this contrasted coastal environment. Biophysical and *in situ* optical measurements were collected in conjunction with above-water hyperspectral remote sensing reflectance (R_{rs}) at 145 stations to understand the mechanisms driving ocean colour variability. The concentrations of measured biophysical data varied considerably; chlorophyll a (Chl$a$) (mean=1.64, range: 0.10 – 7.20 µg.l^{-1}), total suspended matter (TSM) (3.09, 0.82 – 20.69 mg.l^{-1}), and absorption by chromophoric dissolved organic matter ($a_{cdom}(443)$) (0.525, 0.007 – 3.072 m^{-1}), thus representing the spatio-temporal variability of the Salish Sea. Optically, a similar range was found; particulate scattering ($b_p(650)$) (1.316, 0.250 – 7.450 m^{-1}), particulate backscattering ($b_{bp}(650)$) (0.022, 0.005 – 0.097 m^{-1}), total beam attenuation coefficient ($c_t(650)$) (1.675, 0.371 – 9.537 m^{-1}) and particulate absorption coefficient ($a_p(650)$) (0.345, 0.048 – 2.020 m^{-1}). An empirical orthogonal function (EOF) analysis revealed that 95% of the total R_{rs} variability was highly correlated to b_p (r = 0.90), b_{bp} (r = 0.82) and TSM concentrations (r = 0.80) which highlighted the dominant role of riverine systems in this region. Hierarchical clustering analysis was applied to the normalized R_{rs} spectra to further refine the data into four distinct spectral classes. Class 1 was defined by high reflectance between 500-700 nm, indicating more turbid waters, Class 2 was dominated by high Chl$a$ and TSM concentrations which is shown by high reflectance signals at 570 nm and fluorescence and absorption peaks, Class 3 shows strong fluorescence signatures accompanied by low TSM influence and Class 4 is most representative of clear waters with a less defined absorption peak around 440 nm. By understanding the bio-optical factors which control the variability of the R_{rs} spectra this study aims to develop a sub-regional characterization of this coastal region aiming to improve bio-optical algorithms in this complex coastal area.

2.2 Introduction

2.2.1 Background

The Salish Sea, which includes the coastal waters of the Strait of Georgia (SoG) and Puget Sound (Figure 2-1), is home to the most important rearing ground for juvenile Pacific salmon on Canada's West Coast (Beamish et al., 2012; Preikshot et al., 2012). There is increasing evidence to suggest the survivability of juvenile salmon, when they first enter the Salish Sea, is dependent upon ocean productivity, or the production of energy in organic compounds by living organisms, and the time spent in these nutrient rich waters (Andres et al., 2013; Thomson et al., 2012). The occurrence of large zooplankton and phytoplankton blooms has been shown to be highly variable in the region, a result of a combination of biophysical factors such as, ocean temperature, wind speed, cloud cover, and ocean surface stratification caused by riverine inputs (Allen & Wolfe, 2013; Mackas et al., 2013). This variability creates a large opportunity for a timing mismatch between the spring bloom and early marine entry of juvenile salmon when mortality can be quite high (Beamish et al., 2012; Preikshot et al., 2012). Recent work, using a one-dimensional coupled bio-physical model for the central SoG, has shown long-term variations in bloom timing – on the order of decades – but there is still a need for direct sampling of these waters, at high spatial and temporal frequency, to accurately characterize the start of these blooms and to verify model results (Allen & Wolfe, 2013). This can be achieved using daily measurements of chlorophyll *a* (Chl*a*), which is a proxy for phytoplankton production (Sauer et al., 2012).

In the Salish Sea, Chl$a$ data are mostly available from research cruises (Loos et al., 2009; Masson & Peña, 2009; Pawlowicz et al., 2007) and more recently from automated data collection systems, such as those installed on two BC ferry routes in the SoG (Macoun et al., 2010). These data sets still lack the spatial and temporal coverage required to fully represent the dynamics of the entire Salish Sea. One way to fill these knowledge gaps is with spaceborne ocean colour imagery. Ocean colour data works well in Case 1 waters, where Chl$a$ is assumed to be the dominant optical property, but in coastal Case 2 waters with terrestrial influences, other optical constituents, such as suspended matter and chromophoric dissolved organic matter (CDOM), can vary independently and reduce the accuracy of satellite estimates of Chl$a$ (Chen et al., 2012; Darecki & Stramski, 2004; Garcia et al., 2006; Joergensen, 2004; Le et al., 2013a). For the Salish Sea, which is generally considered a Case 2 water body (Komick et al., 2009; Loos & Costa, 2010), the high spatio-temporal variability of the biological and hydrologic processes (Riche et al., 2014) still limits our ability to achieve accurate Chl$a$ retrievals from satellite data (Carswell et al., 2015; Komick et al., 2009).

Significant advances have been made in recent years in resolving Chl$a$ concentrations in Case 2 waters by using regionally specific data to modify standard Chl$a$ algorithms (e.g., Garcia et al., 2006; Komick et al., 2009; Le et al., 2013a; Loisel et al., 2010; Lubac & Loisel, 2007; Werdell et al., 2009). These techniques are often based on an empirical relation between Chl$a$ and remote sensing reflectance, $R_{rs}(\lambda)$, such as the ocean colour three-band algorithm for MODIS (OC3M), which capitalizes on the maximum band ratio of either $R_{rs}(443)$ or $R_{rs}(488)$ normalized to $R_{rs}(547)$ (O'Reilly, 2000), or through a semi-analytical approach that relates remote sensing reflectance below the air-water interface, $r_{rs}(\lambda)$, to the inherent optical properties (IOPs) of the water such as the standard semi-analytical Garver-Siegel-Maritorena version 1 (GSM01) (Gordon et al., 1988; Maritorena, Siegel, & Peterson, 2002). These studies, however, show limited applicability for coastal waters due to a lack of characterization of the optical properties in such conditions, such as the case of the Salish Sea (Komick et al., 2009). Alternatively, work has focused on the fluorescence signal from phytoplankton near 685nm, by using a linear interpolated baseline a fluorescence line height (FLH) and related to Chl*a* concentrations (Gower et al., 1999, 2004).

Previous studies in the Salish Sea, with limited data to April and July conditions, have demonstrated the need for optical classification to improve satellite derived Chl*a* retrievals (Komick et al., 2009). In a preliminary optical water classification, based on measured inherent optical properties (IOPs) including beam attenuation coefficient and absorption to scattering ratios, three spatially distinct water masses were defined in the SoG (Loos & Costa, 2010). Studies from different regions have also used the apparent optical properties (AOPs), such as $R_{rs}(\lambda)$, over various seasons to provide optical classification of surface waters (Lubac & Loisel, 2007; Vantrepotte et al., 2012). Both approaches, using IOPs and AOPs, demonstrated the usefulness of developing a class-based simplification of optically diverse coastal waters for the development and success of class specific inversion algorithms.

The objective of this study was to improve the spatio-temporal bio-optical characterization of the surface waters of the Salish Sea and group regions with similar optical traits towards improving a sub-regional inversion model for retrieving Chl*a* (addressed in Chapter 3). We implicitly assume that waters with similar marine constituents will possess similar $R_{rs}(\lambda)$ spectral signature and thus demonstrate a spatial and or temporal component based on the hydrodynamics of the Salish Sea.

2.2.2 Study area

The study area for the research encompassed the body of water known as the Salish Sea, which includes the estuarine system of the Strait of Georgia, Puget Sound, and the Juan de Fuca Strait. Within the Salish Sea the Strait of Georgia, located between Vancouver Island and mainland British Columbia on the Pacific continental shelf of North America (Figure 2-1), is the largest partially enclosed sea in the region, extending over 200 km in length and reaching depths beyond 350 m within its central region (Masson & Peña, 2009). Connections to the Pacific Ocean are through the Juan de Fuca Strait in the south, and the Johnstone Strait in the north. The region is highly productive and heavily influenced by terrestrial runoff from the Fraser River (Johannessen et al., 2003), which drives an estuarine circulation, subject to wind and tidal mixing (Li et al., 2000; Sutherland et al., 2011). Outflow of the Fraser River typically peaks with a freshet in June, where flow can often be seven times greater than that of low winter values (Masson, 2002). In the Puget Sound, the Skagit and Snohomish river systems provide a similar freshwater influx (average ~ 7000 m^3s^{-1}) peaking around June (Sutherland et al., 2011; USGS, 2015). Because the northern Johnstone Strait is constricted by narrow channels, most of the estuarine exchange flows through the Juan de Fuca Strait (Masson, 2002).

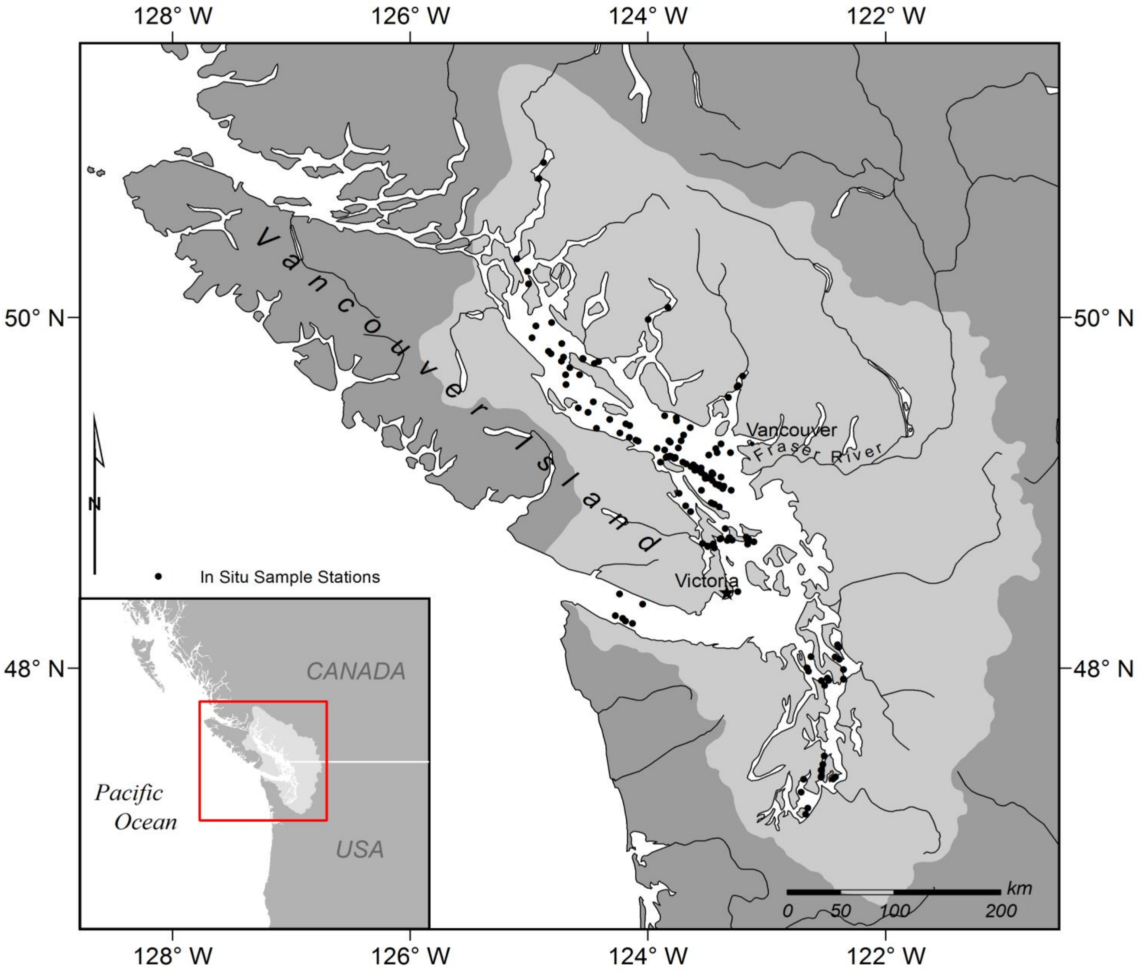

Figure 2-1 Map showing the spatial distribution of the current data set in the Salish Sea.

Phytoplankton abundance in the SoG has been shown to vary with the influence of the Fraser River plume and tidal mixing, with a maximum bloom in the spring typically followed by a smaller fall bloom (Carswell et al., 2015; Masson & Peña, 2009). The dominant phytoplankton species during blooms are diatoms, with *Thalassiosira* species (spp.) and *Skeletonema* spp. being the most common, followed by *Chaetoceros* spp. (Collins et al., 2009; Harrison et al., 1983). The onset of the bloom is primarily a function of wind speed strength and cloud cover, with a lesser dependence on water temperature and freshwater flux (Allen & Wolfe, 2013; Collins et al., 2009). A strong growth of diatoms occurs as light becomes less limited due to decreasing cloud cover and a high near-surface vertical stratification, due to the significant freshwater flux, confining phytoplankton to a shallow well-lit surface layer (Masson & Peña, 2009). Growth continues as a function of light or nutrient levels and ends when nitrate is depleted (Allen & Wolfe, 2013). The vertical structure of the mean Chl*a* distributions also varies seasonally, with the near-surface maximum generally deeper in the summer months when solar radiation is the strongest (Masson & Peña, 2009). Chl*a* concentrations have been found to range from < 1.00 μg l^{-1} in the winter up to 10.00 to 50.00 μg l^{-1} during early spring (Carswell et al., 2015; Harrison et al., 1983; Li et al., 2000; Masson & Peña, 2009).

The optical variability of the SoG has been shown to correlate with the discharge of the Fraser River as well as the oceanographic conditions within the Strait (Loos & Costa, 2010). During high summer river discharge, high loads of fine inorganic particles enter the Strait, (Johannessen et al., 2006), resulting in high, wavelength independent, particulate scattering in plume waters (Loos & Costa, 2010). This is consistent with high concentrations of TSM (1.53 – 15.24 mg l^{-1}) and Chl*a* (1.55 – 6.48 μg l^{-1}) found in the central regions, where TSM has also been shown to dominate total attenuation (Komick et al., 2009). Away from direct river influenced waters, an estuarine circulation exists for much of the SoG where absorption and scattering show spectral dependence. In these waters, absorption was shown to be equally influenced by CDOM and particles, contrary to plume waters where CDOM had a minimal role on total absorption (Loos & Costa, 2010). Higher concentrations of Chl*a* were also found in the spring and summer, west of the Fraser River plume (5.99 – 8.46 µg l^{-1}) (Komick et al., 2009). In northern waters of the SoG, CDOM was shown to dominate total absorption ($a_{cdom}(411) = 0.18 – 1.58$ m^{-1}) and significantly contributed to attenuation of light as these waters are less influenced by the Fraser River (Loos & Costa, 2010).

2.3 Methods

In situ data were collected during five field cruises aboard the W.E. Ricker and bi-weekly trips aboard a ship of opportunity BC Ferry Queen of Alberni, from Duke Point, Nanaimo to Tsawwassen, Vancouver occurring from September, 2012 until October, 2013, covering different seasonal and water conditions (Table 2-1). Measurements were acquired between 11 am and 2 pm to optimize synchronization with any available satellite imagery and optimized sun illumination conditions. Water samples and optical measurements were collected and post processed in a laboratory (Figure 2-2). A detailed sampling regime for each parameter follows.

2.3.1 Discrete water samples

Discrete water samples representing surface waters were acquired at depths < 0.5 m on the research cruises using a high capacity water pump fixed at depth and from a seawater intake pump on the Queen of Alberni as part of a SeaKeeper 1000^{TM} system. Triplicate water samples were collected at each location and stored in dark conditions for a maximum of four hours following acquisition to minimize degradation of water constituents and potential composition changes before filtering for TSM, Chl*a*, and CDOM analysis (Mueller et al., 2003).

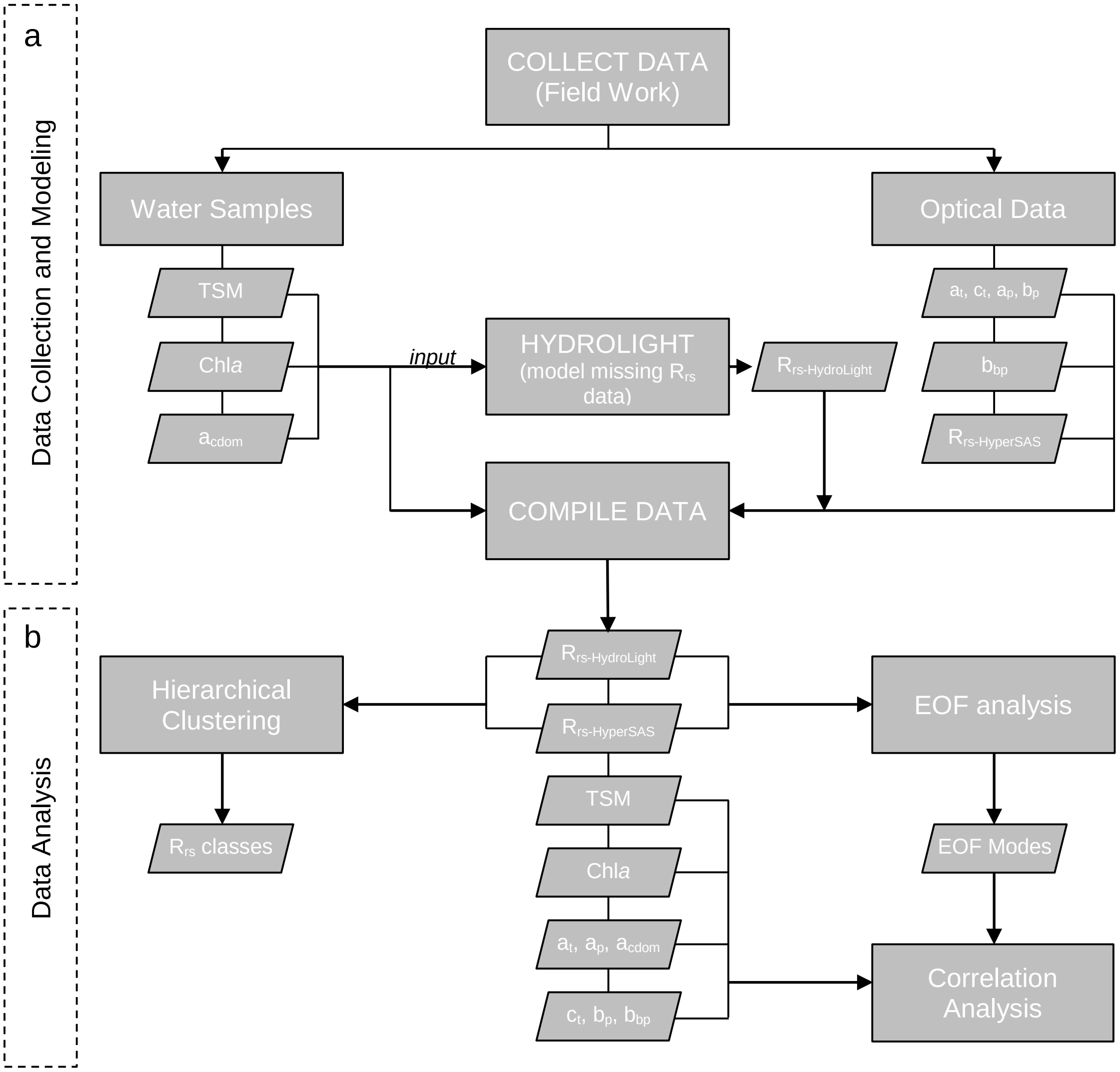

Figure 2-2 Flow chart outlining the methods for **(a)** data collection and **(b)** data analysis.

Water samples were filtered for TSM concentrations through pre-combusted and pre-weighed 0.7 µm Whatman GF/F 47 mm filters. To minimize salt contamination on the filter papers, 300 mL of de-ionized water was used to wash salt residue from the filters following filtration (Stavn et al., 2009). After filtration, the filters were dried at 60°C for six hours then weighed. This process was repeated until a constant weight was achieved and TSM could be calculated (Eaton et al., 2005). To remove organic matter, the filters were combusted at 450°C for one hour and then weighed to determine the particulate inorganic matter (PIM), which is the weight after combustion minus the pre-weighed filter weight (Barille-Boyer et al., 2003). Particulate organic matter (POM) was calculated as POM = TSM – PIM. Weights were normalized for volume of water filtered and then converted to a percentage. Further analysis was done with a Shimadzu SSM-5000A Total Organic Carbon Analyzer to determine the Particulate Organic Carbon (POC) concentrations within each sample by combusting the samples at 450ºC (Bisutti et al., 2004).

Table 2-1 Summary of *in situ* data collected and or derived during field cruises and associated equipment.

Field Data	**Parameter**	**# of Samples**	**Instrument**	**Wavelengths (nm)**
Water Samples	[Chl$a$] (µg l^{-1})	142	Dionex HPLC Analyzer	436, 450
	[TSM] (g m^{-3})	143		na
	[PIM] (%)	141		na
	[POM] (%)	142		na
	[POC] (%)	141	Shimadzu SSM-5000A Total Carbon Analyzer	na
IOPs	$b_p\ (\lambda)$ (m^{-1})	37	WET Labs ac-S	400-737, 4 nm resolution
	$b_{bp}\ (\lambda)$ (m^{-1})	33	WET Labs ECO-BB3	462, 532, 650
	$a_T\ (\lambda)$ (m^{-1})	37	WET Labs ac-S	400-737, 4 nm resolution
	$c_T\ (\lambda)$ (m^{-1})	37	WET Labs ac-S	400-737, 4 nm resolution
	$a_{cdom}\ (\lambda)$ (m^{-1})	143	Ocean Optics USB 4000 Sectrophotometer	300-850, 2 nm resolution
AOPs	$R_{rs}\ (\lambda)$ (sr^{-1})	93	Satlantic HyperSAS	351-797, 1 nm resolution
	$R_{rs}\ (\lambda)$ (sr^{-1})	52	Hydrolight 5 Model	400-750, 10 nm resolution

To measure Chl$a$ and associated pigment concentrations, water samples were filtered through 0.7 µm Whatman GF/F 47mm filters and rinsed with 100 mL of deionized (DI) water before being stored at -20°C. Once in the laboratory, the samples were extracted in 10 mL of 90% acetone solution under low light conditions, stored for

24 h at -4°C, and centrifuged to minimize cellular debris (Arar, 1997). A syringe, fitted with a 0.45 µm inline filter, was then used to remove 2mL of extract into amber vials. Samples were then placed into a Dionex HPLC analyzer and processed with eluent gradients (Eluent A – 75% (v/v) methanol, 25% 0.5 M ammonium acetate, Eluent B – 85% (v/v) acetonitrile, 15% DI water, Eluent C – 100% ethyl acetate) to determine Chl*a* and other pigment concentrations. Standard stocks of Chl*a* and Chl*b*, obtained from DHI Water & Environmental (Denmark), were used to calibrate the measurements, along with multiple pigment standards with an additional certified Chl*a* value.

For CDOM analysis, sample water was filtered through 0.2 µm PALL Supor® membrane disk filters and then stored in 100 mL amber bottles that were pre-rinsed with DI water and pre-combusted at 450°C for one hour. The samples were then analyzed for CDOM absorption using an Ocean Optics USB 4000 spectrophotometer (300-850 nm, 0.2 nm resolution). DI water was used to create a baseline and calibrate the instrument. To correct for residual offsets in the spectra, the average absorption coefficient from 790 to 800 nm was subtracted from all wavelengths (Mitchell et al., 2002). Absorbance values were then converted in to CDOM absorption using Beer-Lambert's Law,

$$a_{cdom}(\lambda) = 2.303\frac{A(\lambda)}{l}, \quad (m^{-1}) \tag{2.1}$$

where $A(\lambda)$ is spectral absorbance and l is the length of the cuvette (0.1m) (Pegau et al., 2003). The slope of the absorbance spectrum, S_{cdom}, was calculated by fitting a single exponential decay function to the absorption spectra in the range of 400 to 700 nm (Del Vecchio & Blough, 2002).

2.3.2 Optical measurements

Reflectance

In conjunction with water measurements, above-water spectral water-surface radiance, $L_t(\lambda)$, sky radiance, $L_s(\lambda)$, and sky irradiance, $E_s(\lambda)$, were measured at 93 stations using a Satlantic HyperSAS sensor array mounted on a mobile platform aboard the Queen of Alberni and a fixed platform aboard the W.E Ricker. The $E_s(\lambda)$ sensor was mounted on a 2 m pole to avoid shadowing. A fixed geometry with the instrument pointed at a 90° azimuth, and the $L_t(\lambda)$ sensor at a 40° angle from nadir was maintained during radiometric measurements (Hooker & Morel, 2003). Data were acquired at stations for 2-5 minutes. Following measurement, the lowest 5% values in the NIR were used to produce an average reflectance spectrum aiming to avoid potential glint contaminated measurements (Hooker and Morel, 2003). Values were converted to above-water remote sensing reflectance, $R_{rs}(\lambda)$, according to Ruddick et al. (2006),

$$R_{rs}(\lambda) = \frac{L_t(\lambda) - \rho_{sky} L_s(\lambda)}{E_s(\lambda)}, \quad (sr^{-1}) \tag{2.2}$$

$$\rho_{sky} = 0.0256 + 0.00039W + 0.000034W^2, when \ \frac{L_s(750)}{E_s(750)} < 0.05 \tag{2.3}$$

$$\rho_{sky} = 0.0256, when \ \frac{L_s(750)}{E_s(750)} \geq 0.05 \tag{2.4}$$

where ρ_{sky} is the proportion of sky radiance that is reflected off the surface of the water, dependent on wind speed, W, and the proportion of cloud cover identified by the sky radiance measurements.

IOPs

In-water spectral measurements of absorption and attenuation were conducted at 38 stations using a WET Labs ac-Spectra (ac-S) instrument. The instrument measures total absorption (a_T) and attenuation (c_T) at a 4 nm resolution between 400 and 737 nm. Given that the vessels rarely held a fixed position, a bench top sampling method was used to allow more precise measurements. Sample water was pumped from a black holding tank using a Sea-Bird SBE 5T submersible pump through the ac-S meter, first unfiltered and then through a vented Pall 0.2 µm capsule filter fitted on the absorption sensor. The filtered measurements were used to obtain absorption by CDOM (a_{CDOM}). Finally, before and after each data collection cruise the ac-S was calibrated using DI water in a laboratory setting to account for any instrument drift (Twardowski et al., 1999). The raw data were extracted using software provided by WET Labs, Inc, and original factory calibration files specific to the instrument were applied. Pure water attenuation (c_w) and absorption (a_w) coefficients, defined by Pope and Fry (1997), were subtracted from the data to produce attenuation (c_t) and absorption (a_t and a_c) values without the effects of pure water (WET Labs, 2011). Data were further corrected for temperature and salinity effects following standard procedure (Sullivan et al., 2006; WET Labs, 2011). Particulate absorption, $a_p(\lambda)$, was calculated by subtracting the corrected filtered measurement from the unfiltered,

$$a_p(\lambda) = a_t(\lambda) - a_c(\lambda), \quad (m^{-1}) \tag{2.5}$$

Additionally, particulate scattering, $b_p(\lambda)$, was acquired as the difference,

$$b_p(\lambda) = c_t(\lambda) - a_t(\lambda), \quad (m^{-1}) \tag{2.6}$$

An ECO-BB3 (WET Labs) sensor was used to measure the total volume scattering function at 117°, $\beta_t(117°)$ for 462, 532, and 650 nm. Measurements were carried out for 34 stations with the instrument mounted inside the black holding tank. Data were corrected for absorption losses along the scattered photon pathway (WET Labs, 2012). Particle backscattering, $b_b(\lambda)$, was derived for each spectra, according to Boss & Pegau, (2001), taking into account measured water temperatures and absorption corrected values. Essentially, known sea water values of the total volume scattering function were subtracted from the measured $\beta_t(117°)$ to obtain the particulate volume scattering function $\beta_p(117°)$ and a factor, χ_p, was used to proportionately link $b_b(\lambda)$ and $\beta_p(117°)$,

$$b_{bp}(\lambda) = 2\pi\chi_p(117^{\circ})\beta_p(117^{\circ}), \quad (m^{-1}) \tag{2.7}$$

2.3.3 Radiative transfer simulation

Radiative transfer modelling was performed with Hydrolight 5 (Sequoia Scientific Inc.) to estimate $R_{rs}(\lambda)$ (n = 52) when measurements were not available. As a first step (Step 1), a subgroup (n = 34) of data with a complete set of measured $R_{rs}(\lambda)$, biogeochemical, and IOP data were input into Hydro light to define the appropriate magnitude of input parameters suitable for these water conditions. These stations covered a range of differing water types, both optically and physically. With this data set, $R_{rs}(\lambda)$ spectra were modelled for 400 – 750 nm at 10nm intervals. From this step, the output modeled $R_{rs}(\lambda)$ were then compared to the measured $R_{rs}(\lambda)$ (Step 2) for the purposes of validating the assumptions of Hydrolight.

As part of Step 1, a four-component Case 2 model was used in Hydrolight, which is based on: pure water, chlorophyll bearing particles, CDOM absorption that does not vary with Chl$a$, and mineral particles. The inputs to the four components were as follows:

(1) Pure seawater component using Pope and Fry's absorption values and seawater scattering (Pope & Fry, 1997).

(2) Chl$a$ concentrations (HPLC) measured *in situ*. The absorption specification was set to the default chlorophyll-based Case 1 model and the scattering specification followed a linear relation set out by Gould et al., (1999) using an empirical constant to describe particle scattering, b_o set to 0.3. A Fournier-Forand phase function with a backscatter fraction of 0.005 was chosen for all runs, which has been shown to be suitable for phytoplankton (Mobley & Sundman, 2008).

(3) CDOM fluorescence was simulated by inputting absorbance at a reference wavelength (440 nm) from measured *in situ* spectrophotometer values. An exponential decay function was chosen for the mass specific absorption specification and a calculated slope (S_{cdom}) was specified was measured *in situ* ranges.

(4) Mineral concentration (TSM) measured *in situ*. The specific absorption coefficient was set to the default chlorophyll-based Case 1 model and the scattering was modelled using a linear relation using Gould et al. (1999) parameters with a modified b_o value optimized for each individual station. A range of suitable values for the Fournier-Forand phase function was also

optimized for each station specified by the backscatter fraction, b_b/b, which was estimated from the ac-S and ECO-BB3 measurements (Mobley et al., 2002).

Chlorophyll and CDOM fluorescence were included in all runs as well as Raman scattering. Air-water surface boundary conditions were specified with field measured wind speed values. Sky spectral radiance distribution was calculated by Hydrolight via RADTRAN by specifying the time, geographical position and cloud cover (percent) for each station. As *in situ* measurements were acquired in deep water at all stations, the water column was assumed to be infinitely deep and bottom effects were not considered to be relevant.

In Step 2, the modelled $R_{rs}(\lambda)$ spectra were statistically compared to the measured $R_{rs}(\lambda)$ spectra acquired in the field for the 34 samples to validate that $R_{rs}(\lambda)$ can be modeled in the study area given the input of *in situ* biogeochemical measurements and Hydrolight assumptions (above). For seven stations with high TSM concentrations (>10 g m^{-3}), a spectrally dependent offset was applied to the modelled $R_{rs}(\lambda)$ to account for a consistent discrepancy found in the red region of the spectrum when compared to *in situ* $R_{rs}(\lambda)$. In Step 3, after evaluating the results of Hydrolight, a specific range of input conditions (b_o and b_{bp}/b) were established, based on the range of *in situ* biogeochemical measurements used in the evaluation. In Step 4, these parameters were input into Hydrolight, together with the measured *in situ* biogeochemical concentrations to calculate $R_{rs}(\lambda)$ for the 52 stations in which $R_{rs}(\lambda)$ data was missing. This produced a simulated data set to expand (total n = 145) the complete set, which includes measured and calculated AOPs and IOPs.

2.3.4 Hierarchical clustering

An empirical orthogonal function (EOF) analysis, also referred to as principal component analysis, was applied to the *in situ* and modelled $R_{rs}(\lambda)$ spectra in an effort to understand the variability within the data set (Lubac & Loisel, 2007; Mueller, 1976; Sathyendranath et al., 1989; Toole & Siegel, 2001). Through this analysis the data are reduced to a set of linear orthogonal functions or modes (Toole & Siegel, 2001). Only the first three modes were used and ranked in order of importance, with the first EOF mode accounting for the largest amount of variability (Lubac & Loisel, 2007). To further this analysis, the relationship between the EOF modes and measured *in situ* water properties were compared using a correlation analysis to investigate how the optically significant constituents affect the shape and magnitude of the $R_{rs}(\lambda)$ spectra and to ultimately understand the primary drivers behind these differences in the Salish Sea (Toole & Siegel, 2001).

To group the $R_{rs}(\lambda)$ spectra, an unsupervised hierarchical cluster analysis (HCA) was applied using MATLAB code, Math Works Inc., to classify the 145 stations into distinct optical groups. Input vectors to the HCA analysis were created by normalizing the $R_{rs}(\lambda)$ spectra with respect to their integral,

$$\langle R_{rs}(\lambda) \rangle = \frac{R_{rs}(\lambda)}{\int_{400}^{700} R_{rs}(\lambda)\, d\lambda} \tag{2.8}$$

This was done to reduce the first order variability in the data and focus on shape rather than spectral magnitude (Craig et al., 2012; Vantrepotte et al., 2012). Previous studies, aiming at classifying spectral reflectance, have focused on raw reflectance data as input (Le et al., 2011; Moore et al., 2009) or normalized spectra with respect to a specific wavelength (Torrecilla et al., 2011). The advantage of normalizing the spectra with respect to the integrated value is to avoid artificially giving weight to a particular part of the $R_{rs}(\lambda)$ spectrum during the clustering analysis (Vantrepotte et al., 2012).

In the analysis, a distance matrix was created by comparing the pairwise distances between $\langle R_{rs}(\lambda)\rangle$ values in the input data set to define similarities or dissimilarities. The distance was computed using the cosine distance function, *d*, defined as one minus the cosine of the angle θ between each pairs of points,

$$d(x_1, x_2) = 1 - \cos\theta = 1 - \left(\frac{x_1 \cdot x_2}{\|x_1\| \times \|x_2\|}\right) \tag{2.9}$$

where x_1 and x_2 are defined as the input points and θ is the angle between them. As this angle decreases, $\cos\theta$ approaches one and the distance becomes small, resulting in more similarity between the points (Torrecilla et al., 2011). This method is relevant to the current study as it focuses on spectral shape as opposed to magnitude (Torrecilla et al., 2011). To group similar clusters of distances, an unweighted average distance linkage algorithm was used. From the linkage algorithm an agglomerative hierarchical cluster tree (dendrogram) was formed to partition the $R_{rs}(\lambda)$ input vectors into clusters of objects from which classes were formed (Berkhin, 2006). The numbers of classes, specified to the algorithm, was first selected as six and then reduced until distinct individual classes were achieved. Previous knowledge of the optical variability in the region established three dominant water classes: riverine plume, estuarine, and northern waters (Komick et al., 2009; Loos & Costa, 2010). For the present $R_{rs}(\lambda)$ dataset, four classes were found to be distinguishable.

2.4 Results

2.4.1 Biophysical and optical data

The biophysical and optical parameters of the Salish Sea are highly variable from the fall of 2012 to the fall of 2013 (Table 2-2). Concentrations of Chl$a$ varied the most during the spring months with a range of 0.10 µg l^{-1} to 7.2 µg l^{-1}, with low Chl$a$ values (0.10 µg $l^{-}1$) measured in the northern waters towards Johnstone Strait and maximum Chl$a$ values (7.20 µg l^{-1}) measured in the central SoG waters during spring phytoplankton bloom conditions. Measured TSM concentrations showed the greatest variability in the central regions during the spring months, with concentrations ranging from 0.82 mg l^{-1} in early March to 20.69 mg l^{-1} in May, corresponding to peak Fraser River discharge (Figure 2-3). Mean Fraser River discharge during data acquisition was 1564 m^3s^{-1} in late September, 7391 m^3s^{-1} (5-fold increase) for May and June, then 1734 m^3s^{-1} the following September (Figure 2-3) (Environmental Canada, 2014). High TSM concentrations were associated with high percentages of inorganic particulates (Table 2.2). POC analysis revealed a steep increase in organic carbon in late June (31.1 %), which correlated with high Fraser River discharge (7557 m^3s^{-1}) and summer phytoplankton blooms (Chl$a$ ~ 4.5 µg l^{-1}).

The optical properties showed a similar range in variability to the biophysical properties (Table 2.2). Total attenuation, $c_t(\lambda)$, was the highest in the blue wavelengths and decreased towards the red wavelengths (Figure 2-4). Attenuation was one order of magnitude higher in riverine plume influenced waters compared to lower values measured in more clear conditions in the northern SoG. The overall magnitude of $c_t(\lambda)$ was found to increase primarily with the magnitude of particulate scattering, except for stations far from the influence of plume waters. Total absorption, $a_t(\lambda)$, followed a similar spectral shape as $c_t(\lambda)$, increasing towards the blue wavelengths, indicating strong absorption by organic matter (phytoplankton pigments and CDOM). Highest $a_t(\lambda)$ values were measured within the influence of plume, sediment rich waters. Similarly, high absorption by CDOM at 443 nm (3.072 m^{-1}) was associated with plume waters during the spring, and low values (0.007 m^{-1}) found in northern oceanic waters during the summer. The Chl*a* absorption peak near 675 nm was present in waters of the central and northern regions and corresponded to high Chl*a* concentrations measured at these stations.

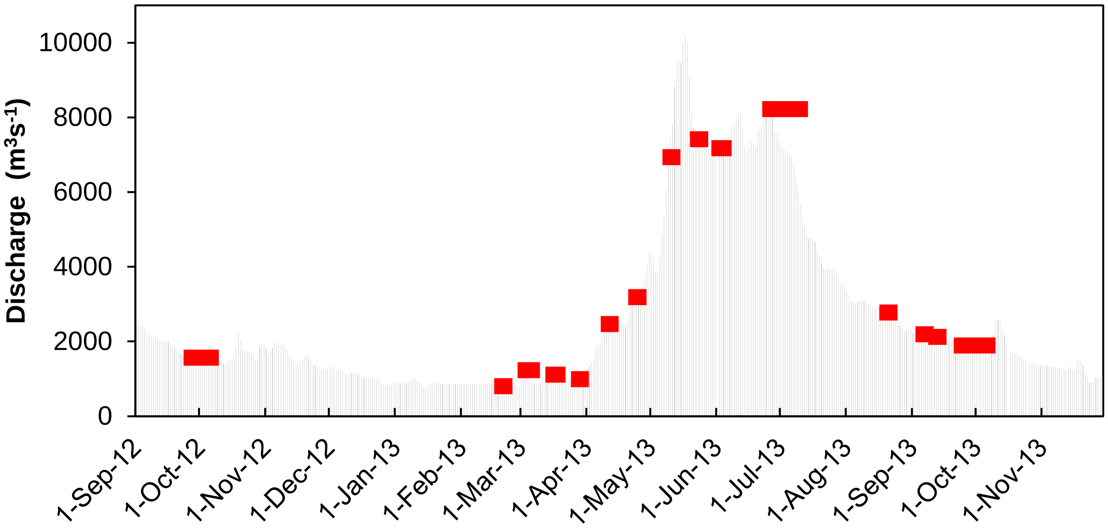

Figure 2-3 Fraser River discharge for September 2012 - December 2013 (Environment Canada, 2014) with field sampling shown as solid red bars.

Particulate scattering, $b_p(\lambda)$, showed a consistent trend throughout the study site, peak values in the blue wavelengths followed by a slight decreasing trend towards the red

Table 2-2 *In situ* bio-optical parameters separated into spring (Feb – May), summer (June – Sept) and fall (Oct – Nov) seasons. Average in bold, standard deviation in parentheses, and minimum and maximum values in square brackets.

Parameter	Overall	Spring	Summer	Fall
Chl$a$ (μg l^{-1})	**1.64** (1.51) [0.10 – 7.20] n = 142	**1.54** (1.55) [0.10 – 7.20] n = 41	**2.03** (1.78) [0.26 – 6.83] n = 54	**1.27** (0.91) [0.24 – 4.11] n = 47
TSM (mg l^{-1})	**3.09** (2.73) [0.82 – 20.69] n = 143	**4.48** (4.55) [0.82 – 20.69] n = 39	**3.03** (1.16) [1.24 – 7.56] n = 57	**2.01** (1.02) [1.05 – 5.66] n = 47
PIM (%)	**58.5** (13.2) [11.6 –91.8] n = 141	**60.8** (17.8) [11.6 – 91.8] n = 37	**56.7** (11.8) [30.0 – 80.9] n = 57	**60.2** (10.9) [40.2 – 87.8] n = 47
POM (%)	**41.3** (13.0) [8.0 – 90.8] n = 142	**39.3** (16.8) [7.99 – 90.8] n = 38	**44.3** (11.3) [17.0 – 71.8] n = 57	**39.3** (10.5) [12.2 – 60.0] n = 47
POC (%)	**11.5** (5.3) [2.0 – 31.1] n = 141	**11.8** (6.2) [2.0 – 31.1] n = 37	**13.2** (5.2) [3.7 – 29.8] n = 57	**9.1** (3.3) [3.4 – 17.2] n = 47
b_p (650) (m^{-1})	**1.316** (1.455) [0.250 – 7.450] n = 37	**2.783** (2.047) [0.588 – 7.450] n = 9	**0.844** (0.733) [0.250 – 3.599] n = 28	na
b_{bp} (650) (m^{-1})	**0.022** (0.022) [0.005 – 0.097] n = 34	**0.031** (0.023) [0.008 – 0.068] n = 9	**0.019** (0.021) [0.005 – 0.097] n = 25	na
b_{bp}/b_p	**0.020** (0.009) [0.009 – 0.054] n = 34	**0.013** (0.003) [0.010 – 0.020] n = 9	**0.022** (0.009) [0.009 – 0.054] n = 25	na
a_t (650) (m^{-1})	**0.359** (0.363) [0.095 – 2.086] n = 37	**0.684** (0.546) [0.157 – 2.086] n = 9	**0.255** (0.182) [0.095 – 0.953] n = 28	na
a_p (650) (m^{-1})	**0.345** (0.391) [0.048 – 2.020] n = 30	**0.632** (0.541) [0.096 – 2.020] n = 9	**0.223** (0.206) [0.048 – 0.894] n = 21	na
a_c (443) (m^{-1})	**0.552** (0.142) [0.261 – 0.844] n = 31	**0.638** (0.090) [0.531 – 0.834] n = 9	**0.517** (0.145) [0.261 – 0.844] n = 22	na
a_{cdom} (443) (m^{-1})	**0.525** (0.409) [0.007 – 3.072] n = 143	**0.660** (0.641) [0.127 – 3.072] n = 41	**0.531** (0.218) [0.007 – 1.044] n = 58	**0.391** (0.249) [0.120 – 1.551] n = 44
c_t (650) (m^{-1})	**1.675** (1.808) [0.371 – 9.537] n = 37	**3.467** (2.574) [0.745 – 9.537] n = 9	**1.099** (0.908) [0.371 – 4.553] n = 28	na

wavelengths. One order of variability is observed with a range of 0.573 – 7.450 m^{-1} (Table 2.2) at 650 nm. The highest magnitudes measured were in areas heavily influenced by Fraser River plume waters, characterized by high inorganic particulates.

Particulate backscattering demonstrated similar variability, 0.014 - 0.097 m^{-1} (Table 2.2), with the highest values again associated to high inorganic particulate concentrations found in plume conditions.

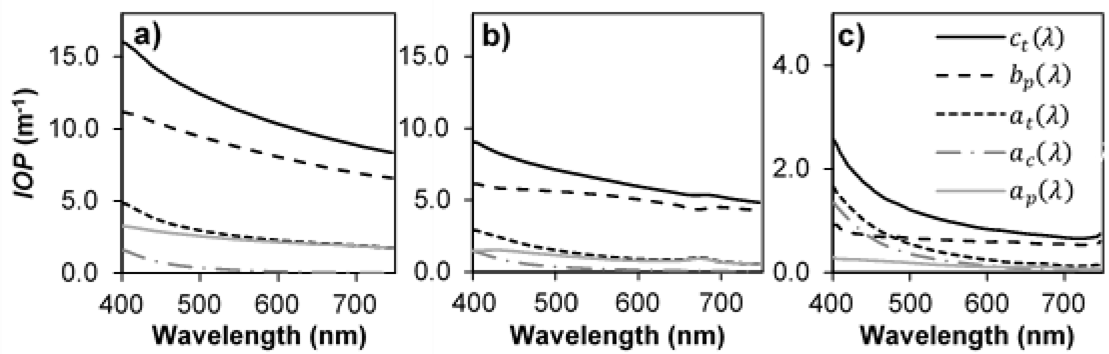

Figure 2-4 Inherent optical properties (IOPs) for typical **(a)** plume water (Stn 073), **(b)** transitional water (Stn 069), and **(c)** oceanic water (Stn 081) all measured in June 2013.

2.4.2 Remote sensing reflectance

A high variability was found in the hyperspectral $R_{rs}(\lambda)$ derived from the sampled stations (Figure 2-5a). Spectra ranged in both magnitude and shape, likely attributable to the highly variable range of water properties measured. A general trend with all the spectra can be observed: low values of $R_{rs}(400)$ increase to a peak near 580 nm and decrease until 750 nm. Some spectra show an additional peak at approximately 680 nm, corresponding to Chl$a$ fluorescence (Gower, 1980; Neville & Gower, 1977). The peak near R_{rs} (580) varies from 0.001 to 0.027 sr^{-1} with the largest $R_{rs}(580)$ magnitudes found in plume water regions between April and June, where TSM concentrations greater than 8.0 g m^{-3} were measured. Lower $R_{rs}(\lambda)$ values are typically associated with clearer, oceanic waters to the north or in regions where TSM concentrations were measured below 2.0 mg l^{-1}, such as in Puget Sound.

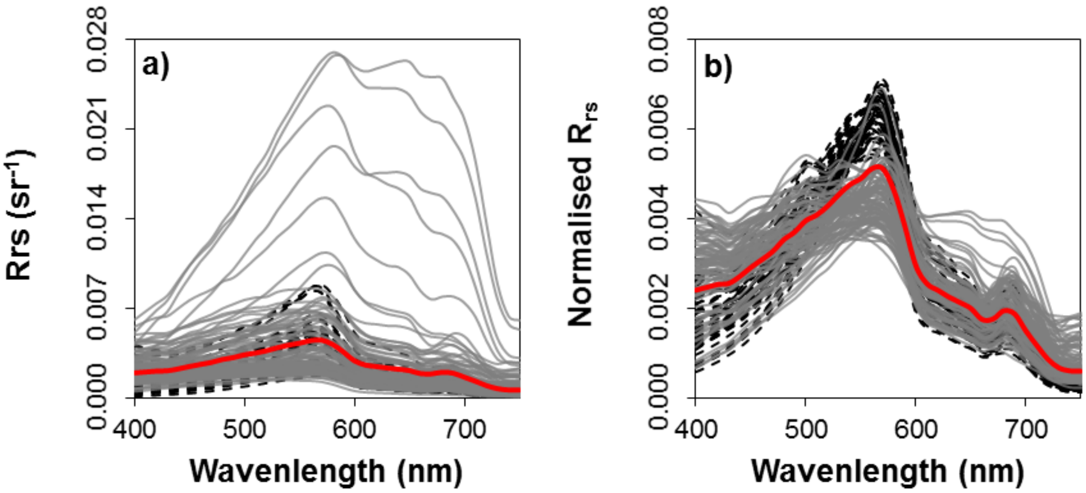

Figure 2-5 **(a)** Remote sensing reflectance, $R_{rs}(\lambda)$, in sr^{-1} for the five DFO cruises, bi-weekly ferry cruises and modelled values, **(b)** Normalized $R_{rs}(\lambda)$ to the integral. In situ values are in grey, Hydrolight modelled values are dashed, and average values are shown in red.

As part of the parameterization of Hydrolight, an interactive approach was taken to initially refine the input scattering coefficients, b_o and b_{bp}/b, so a better representation of the local water conditions could be achieved. Initial evaluation of the modeled $R_{rs}(\lambda)$ revealed a constant underestimation in the red region compared to the measured *in situ* spectra. To compensate for this, the average difference between the modelled $R_{rs}(\lambda)$ values and measured $R_{rs}(\lambda)$ was calculated for each wavelength in the red-near infrared region (600-750nm). These differences (avg 35%) were then averaged to create a wavelength dependent offset that was added to the modelled spectra for the 600-750nm range to correct the modelled spectra in the red. Finally, the modeled $R_{rs}(\lambda)$ were statistically compared to the corresponding *in situ* $R_{rs}(\lambda)$. The final results showed a strong correlation (avg R^2 = 0.90; p < 0.01), but with spectral dependence (Figure 2-6). The slopes of the linear regressions range from 0.67 – 1.05 with slopes closest to 1.0 between 550 – 600 nm, decreasing towards the blue and into the red spectra. This agreement provided confidence to use Hydrolight to simulate the 52 stations where $R_{rs}(\lambda)$ was not acquired *in situ*. Figure 2-5a shows the modeled $R_{rs}(\lambda)$ (dashed).

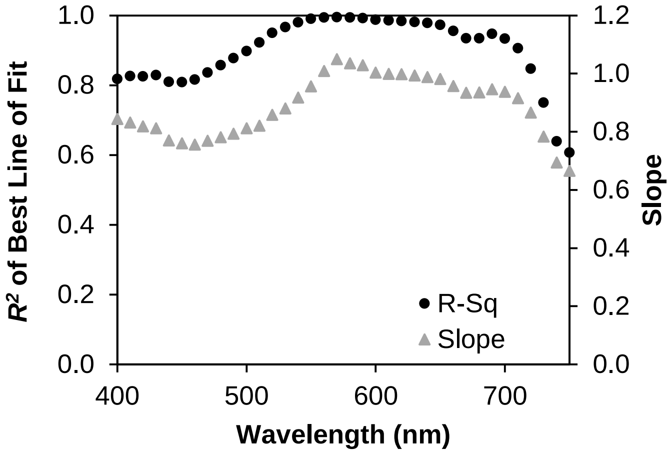

Figure 2-6 Correlation between measured in situ $R_{rs}(\lambda)$ spectra and modelled $R_{rs}(\lambda)$ using Hydrolight. R^2 is shown as closed circles and slopes are triangles.

2.4.3 Empirical orthogonal function analysis

The results of the empirical orthogonal function (EOF) analysis of the $R_{rs}(\lambda)$ data are shown in Figure 2-7. Three dominant modes were produced to represent the variance within the data set. To understand the drivers of this variability, a correlation analysis was applied between each of the EOF mode amplitude spectra, or loadings, and measured *in situ* bio-geochemical and bio-optical parameters (Figure 2-8).

The first mode, which accounts for 94.5% of the total variance, shows a positive spectral shape, similar to the mean of all $R_{rs}(\lambda)$, with the distinct peak at 580 nm (Figure 2-7). Correlation analysis shows a significant ($p < 0.01$) positive correlation between the first EOF mode and TSM ($r = 0.80$), $b_{bp}(650)$ ($r = 0.82$), and $b_p(650)$ ($r = 0.90$) (Figure 2-8), indicating that TSM, and consequently particulate scattering and backscattering are significantly affecting the variance in the total $R_{rs}(\lambda)$ dataset. POC also demonstrated positive correlation to EOF mode 1, although much lower and less significant (r = 0.28, $p < 0.01$). Additionally, $a_{cdom}(443)$ also showed a positive correlation (r = 0.30), but not statistically significant ($p > 0.05$). This suggests that EOF mode 1 is very representative of turbid water spectra where the largest variability of the data is occurring, namely in the green-red portion of the spectrum. Furthermore, there was no significant correlation between EOF mode 1 and Chl*a* (r = 0.17, $p > 0.05$), and the particulate backscattering ratio was found to be uncorrelated (r = 0.03, $p > 0.05$) (Figure 2-8).

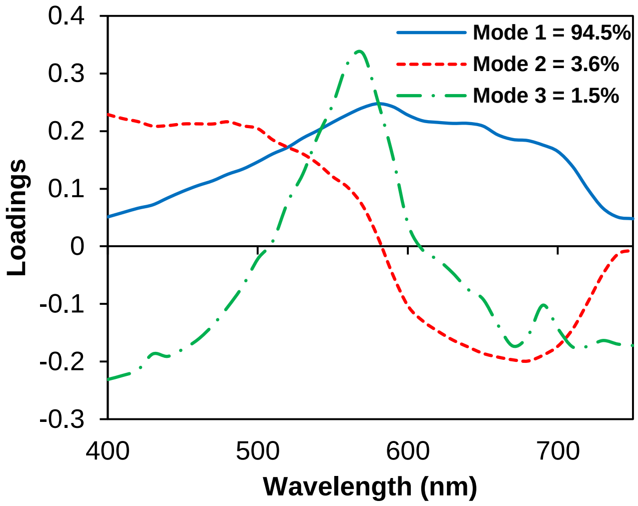

Figure 2-7 Loadings and percent variance for the first three modes of the EOF analysis of R_{rs}.

The second EOF mode, which accounts for 3.6% of the variability, shows an inverse spectral relationship in comparison to the first mode (Figure 2-7). This curve exhibits a steady decrease from 400 nm to 670 nm. Similar to EOF mode 1, this mode also shows positive correlation to particulate scattering and backscattering and a significant relationship between $b_p(650)$ is noticeable (r = 0.64; $p < 0.05$) (Figure 2-8). In contrast to EOF mode 1 however, TSM does not appear to play a role in the variability and is in fact negatively correlated (r = -0.22, p < 0.01). No significant correlation was found between EOF mode 2 and Chl*a*, POC, $a_{cdom}(443)$ and the particulate scattering ratio, indicating the composition of particulate matter is not impacting the second mode of variability (Lubac & Loisel, 2007).

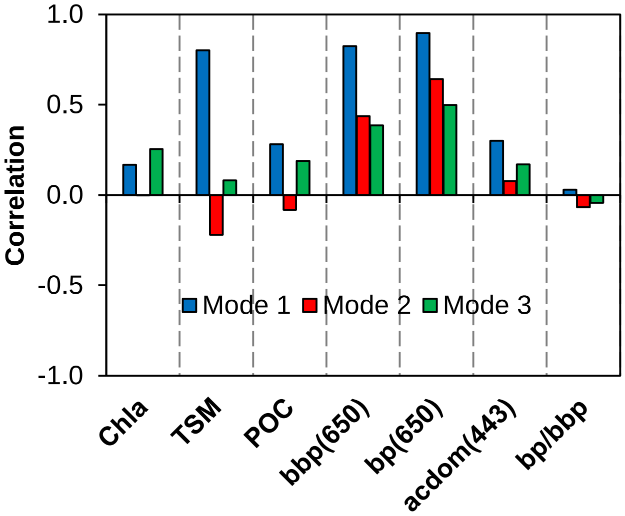

Figure 2-8 Correlation coefficients calculated between the EOF amplitude factors and the measured *in situ* biogeochemical and bio-optical parameters for EOF modes 1-3.

The third mode accounts for the least amount of variability, at 1.5%, but shows a very dominant spectral structure with peaks near 580 and 690 nm, which is representative of the majority of the spectra measured in the study site. The correlation analysis shows a moderate correlation (r = 0.25, p < 0.01) to Chl*a* between all three EOF modes and therefore the spectral peaks near 580 and 690 nm are likely related to maximum reflectance and fluorescence by Chl*a*, respectively. Similarly to EOF mode 2, the highest correlation is found for $b_{bp}(650)$ (r = 0.39, p > 0.01) and $b_p(650)$ (r =0.50, p < 0.01), although $b_{bp}(650)$ showed less significance. A low correlation was found between EOF mode 3 and POC (r = 0.19) and $a_{cdom}(443)$ (r = 0.17) and no significant correlation was found for TSM and b_{bp}/b_p. It is therefore reasonable to assume EOF mode 3 is demonstrating the role of Chl$a$ in the study area.

These results demonstrate the ability of an empirical orthogonal function analysis to assess the main modes of $R_{rs}(\lambda)$ variability and determine the main drivers of these modes. From this analysis, two dominant trends emerged: the highest variability of $R_{rs}(\lambda)$ was primarily associated with TSM, through particulate scattering and backscattering in the green and red, and secondarily through Chl$a$ influences, affecting the spectra most predominantly near 580 and 690 nm. These results suggest that two dominant optical water classes exist in the Salish Sea. This provides a necessary first step in applying a class-based approach to sub-regionalizing the optical variability.

2.4.4 $\boldsymbol{R_{rs}(\lambda)}$ classification

The results of the unsupervised hierarchical clustering analysis (HCA) of the normalized $R_{rs}(\lambda)$ spectra are shown in Figure 2-9. A total of n = 145 spectra (modelled and measured) were input into the clustering algorithm and four distinct classes were identified through a dendrogram. Partitioning the data on the basis of the normalized spectra allowed the clustering algorithm to define similarities in spectral shape rather than magnitude (Figure 2-5b), which has been demonstrated to be advantageous in other coastal regions (Craig et al., 2012; Lubac & Loisel, 2007; Vantrepotte et al., 2012).

Class 1 (n = 3) shows the highest $R_{rs}(\lambda)$ magnitudes in comparison to the other three classes, particularly in the red spectral region (Figure 2-9a). Spectra in this class are distinguishable by a steep increasing $R_{rs}(\lambda)$ from the blue to the green wavelengths, with a maximum peak at 580 nm, then a broad peak in the red spectral region. There are no discernible fluorescence peaks in the far end of the red spectra in this class. The biophysical characteristics show the highest mean TSM concentrations (15.9 ± 3.72 mg l^{-1}) and lowest mean Chl$a$ concentrations (0.47 ± 0.18 µg l^{-1}) (Table 2-3), which were measured in the Fraser River plume during the spring and summer months (Figure 2-10). This class of spectra was not present in the fall and winter months. Bio-optical data show the highest mean values of $a_{cdom}(443)$ (2.522 ± 0.552 m^{-1}), which is evident in the blue region of the spectrum where $R_{rs}(\lambda)$ values are the lowest. Unfortunately, due to logistic problems, measurements of b_p or b_{bp} were not available for stations in this class.

Class 2 (n = 16) shows similar characteristics to Class 1, with average $R_{rs}(\lambda)$ values increasing in magnitude from the blue to the green regions of the spectrum, with a pronounced peak near 580 nm. Unlike Class 1, this class does not exhibit a broad peak in the red spectra, and a secondary fluorescence peak at 690 nm is observed (Figure 2-9b). Overall, $R_{rs}(\lambda)$ magnitudes cover the widest range of variability of all four classes. Spatially, this class is well represented in the central portions of the Salish Sea throughout the spring and summer and only in Puget Sound for the fall months (Figure 2-10). The biophysical data show lower mean TSM concentrations than Class 1 (5.51 ± 4.09 mg l^{-1}) but the highest mean Chl$a$ concentration of all four classes (2.23 ± 1.95 µg l^{-1}). Bio-optical data show lower absorption by CDOM in comparison to Class 1, with a mean $a_{cdom}(443)$ of 0.864 m^{-1} (± 0.425 m^{-1}). Scattering and backscattering by particulates is the highest, 3.847 m^{-1} and 0.055 m^{-1}, respectively, among the three classes in which these variables were measured.

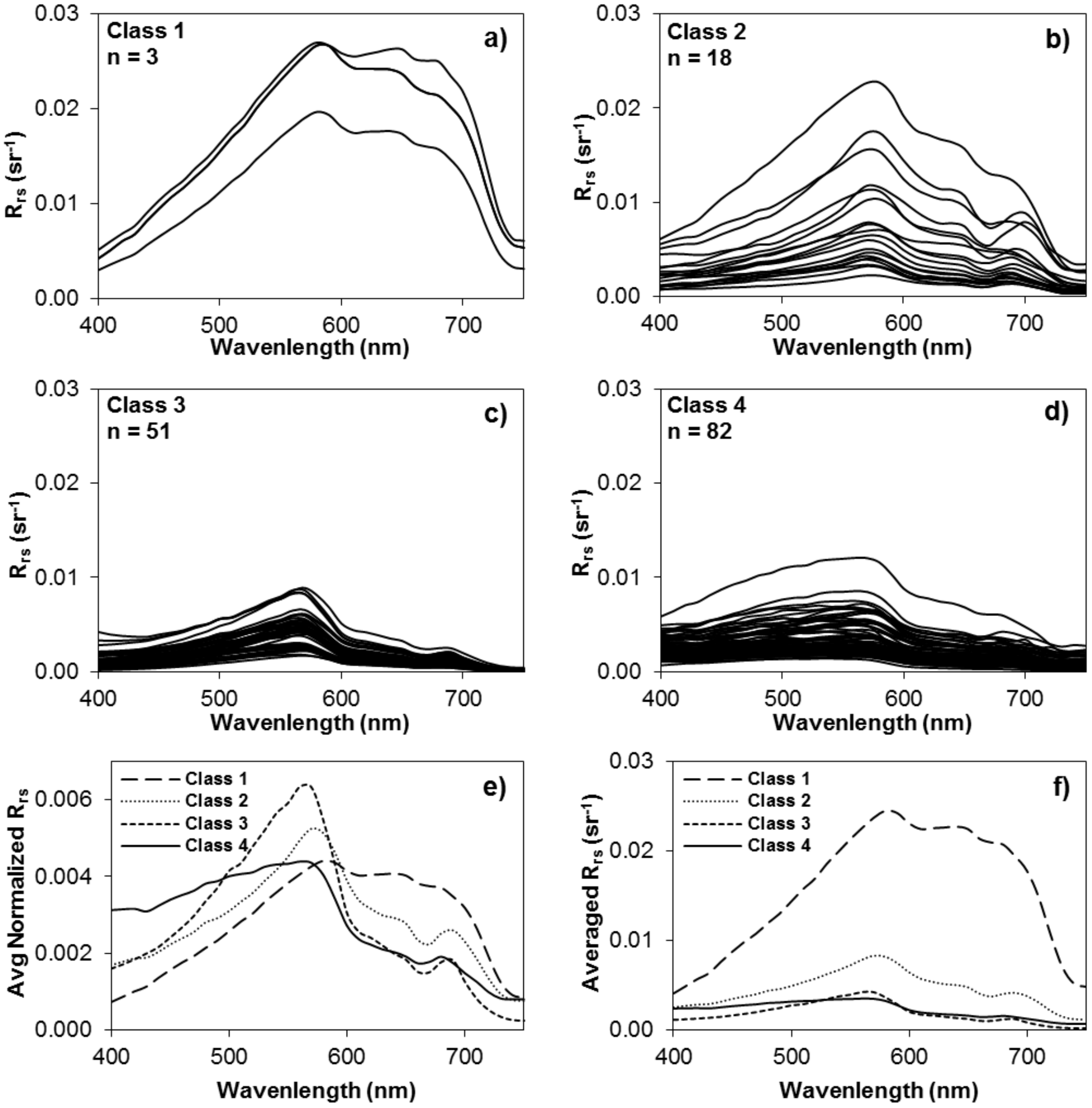

Figure 2-9 $R_{rs}(\lambda)$ spectra derived from an unsupervised hierarchical classification of *in situ* and simulated data with 4 classes **(a-d)**. For each class **(e)** average normalized $R_{rs}(\lambda)$ and **(f)** average $R_{rs}(\lambda)$.

The spectra comprising Class 3 (n = 49) are characterized by lower $R_{rs}(\lambda)$ magnitudes than Class 1 or Class 2. The spectra show similar shape as in Class 2 but with a more pronounced central peak, found earlier near 570 nm (Figure 2-9c). These stations are found in the central Salish Sea in the spring and summer months with some spectra measured in Puget Sound also during the summer. During the fall months, this class is represented in all regions of the study area, including the northern inlets and western Strait of Juan de Fuca (Figure 2-10). Average concentrations of TSM (2.35 ± 1.12 mg l^{-1}) and Chl$a$ (2.03 ± 1.71 µg l^{-1}) were lower and appear to contribute more equally to the observed spectra. Bio-optically, mean $a_{cdom}(443)$ (0.355 ± 0.223 m^{-1}) is the lowest of all the classes, which is likely contributing to the slight increase in $R_{rs}(\lambda)$ values around 400 nm. Scattering by particulates shows relatively low contribution with a mean $b_p(650)$ of 1.058 m^{-1} (± 0.429 m^{-1}) and mean $b_{bp}(650)$ of 0.021 m^{-1} (± 0.010 m^{-1}).

Class 4 captured the largest number of samples (n = 76). $R_{rs}(\lambda)$ spectra are characterized by the highest values in the blue and low values in the red spectra. A consistent spectral shape is observed in all spectra; high magnitudes observed in the blue region increasing slightly to a broad spectral peak centered around 560 – 570 nm. Spatial distribution of this class shows seasonal dependency with samples clustering in the central Salish Sea in the spring months then shifting to include the northern and southern waters during the summer (Figure 2-10). In the fall, samples in this class were only observed in the central and southern portions of the Salish Sea, close to the Gulf islands where the Fraser plume should be less influential, and in the Puget Sound. Relatively low mean TSM (2.59 ± 1.00 mg l^{-1}) and Chl$a$ (1.26 ± 1.05 µg l^{-1}) concentrations were observed, which is expressed in the overall low $R_{rs}(\lambda)$ values. Bio-optically, mean $a_{cdom}(443)$ shows low magnitude (0.498 ± 0.195 m^{-1}) as is $b_p(650)$ and $b_{bp}(650)$ with means of 0.889 m^{-1} (± 0.762 m^{-1}) and 0.017 m^{-1} (± 0.017 m^{-1}), respectively.

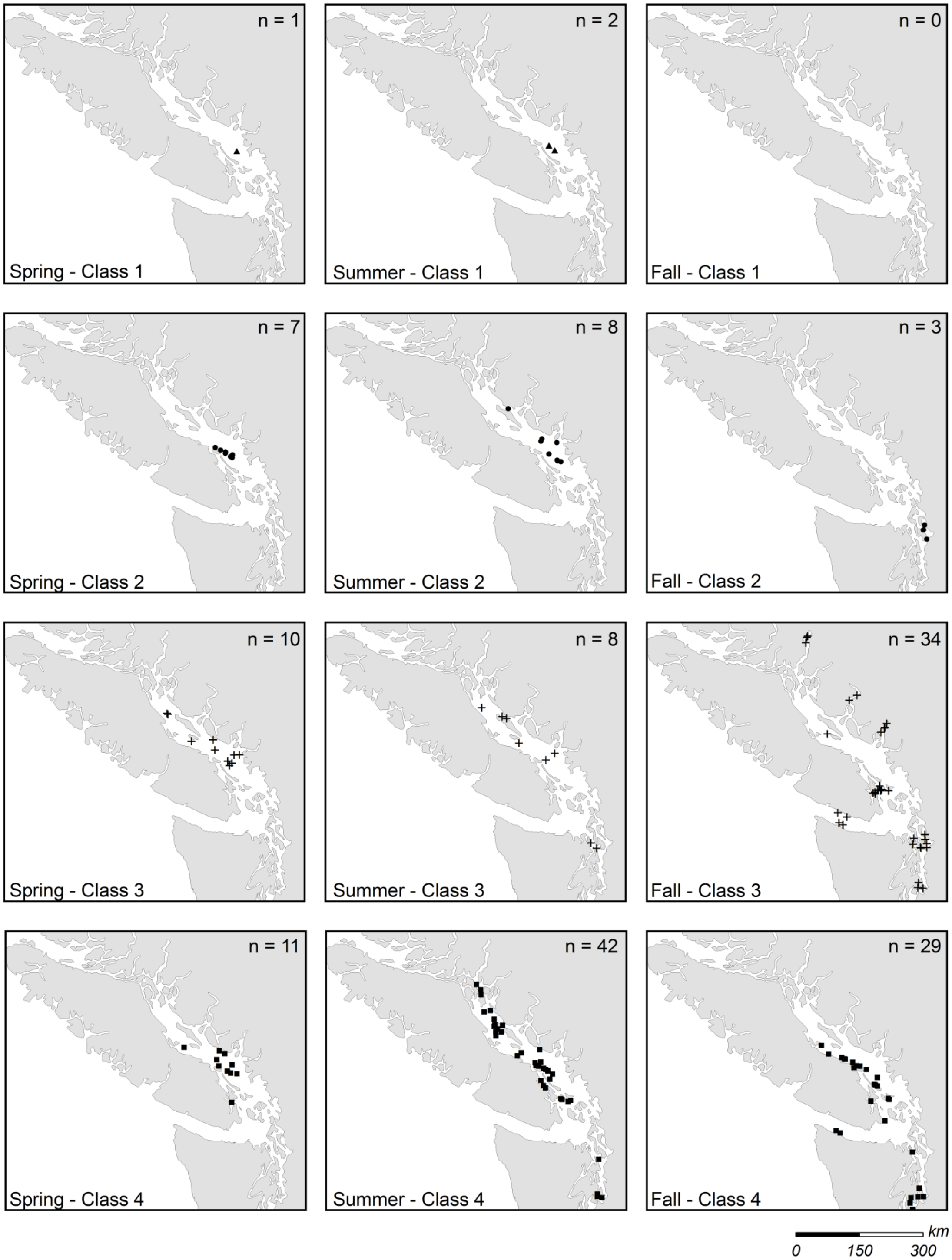

Figure 2-10 Spatial distribution of Classes 1-4 for spring, summer, and fall.

Table 2-3 *In situ* bio-optical variables separated into classes 1 - 4. Average in bold, standard deviation in brackets, and minimum and maximum values in square brackets. Largest average bio-optical variable is highlighted for each class.

Variable	Class 1	Class 2	Class 3	Class 4
Chl$a$ (µg l^{-1})	**0.47** (0.18) [0.21 – 0.63] n = 3	**2.55** (2.03) [0.42 – 7.20] n = 16	**2.03** (1.71) [0.10 – 6.83] n =49	**1.26** (1.05) [0.82 – 4.93] n = 74
TSM (g m^{-3})	**15.9** (3.72) [11.6 – 20.7] n = 3	**5.31** (4.09) [1.55 – 16.03] n = 16	**2.35** (1.12) [1.09 – 5.66] n = 49	**2.59** (1.00) [0.82 – 5.11] n = 75
PIM (%)	**85.2** (5.4) [77.6 – 89.8] n = 3	**57.5** (22.2) [11.6 – 91.8] n = 16	**59.8** (12.9) [32.8 – 88.3] n = 47	**57.3** (10.6) [30.0 – 82.6] n = 75
POM (%)	**13.0** (3.0) [10.3 – 17.1] n = 3	**40.6** (21.7) [7.99 – 90.8] n = 16	**40.8** (12.2) [12.2 – 71.8] n = 47	**43.2** (9.7) [17.4 – 62.3] n = 76
POC (%)	**2.48** (0.38) [2.15 – 3.02] n = 3	**12.3** (8.4) [2.02 – 31.2] n = 15	**12.7** (5.1) [3.4 – 29.8] n = 48	**11.0** (4.3) [3.9 – 22.7] n = 75
b_p (650) (m^{-1})	Not available (na)	**3.847** (2.236) [0.573 – 7.450] n = 5	**1.058** (0.429) [0.481 – 1.679] n = 6	**0.889** (0.762) [0.250 – 3.456] n = 26
b_{bp} (650) (m^{-1})	na	**0.055** (0.031) [0.014 – 0.097] n = 5	**0.021** (0.010) [0.008 – 0.036] n = 5	**0.017** (0.017) [0.005 – 0.068] n = 24
b_{bp}/b_p	na	**0.019** (0.005) [0.014 – 0.027] n = 5	**0.020** (0.007) [0.009 – 0.029] n = 5	**0.020** (0.010) [0.009 – 0.054] n = 24
a_t (650) (m^{-1})	na	**0.976** (0.619) [0.175 – 2.086] n = 5	**0.315** (0.101) [0.184 – 0.460] n = 6	**0.251** (0.160) [0.095 – 0.747] n = 26
a_p (650) (m^{-1})	na	**0.915** (0.619) [0.104 – 2.020] n = 5	**0.268** (0.131) [0.055 – 0.427] n = 5	**0.222** (0.176) [0.048 – 0.689] n =20
a_c (443) (m^{-1})	na	**0.702** (0.103) [0.531 – 0.834] n = 5	**0.567** (0.077) [0.418 – 0.640] n = 5	**0.513** (0.138) [0.261 – 0.844] n =21
a_{cdom} (443) (m^{-1})	**2.522** (0.552) [1.766 – 3.072] n = 3	**0.864** (0.425) [0.236 – 1.806] n = 16	**0.355** (0.223) [0.007 – 1.017] n = 49	**0.498** (0.195) [0.127 – 0.974] n = 75
c_t (650) (m^{-1})	na	**4.823** (2.838) [0.749 – 9.537] n = 5	**1.373** (0.527) [0.665 – 2.138] n = 6	**1.140** (0.908) [0.371 – 4.203] n = 26

2.5 Discussion

The scope of this research was to build a more comprehensive bio-optical characterization of the surface waters of the Salish Sea to understand the drivers of remote sensing reflectance variability. Five research cruises and twelve ferry-based surveys were conducted to cover the wide range of optical and biogeochemical conditions during the period from September, 2012 to the October, 2013. The results from the IOP, AOP, and biogeochemical measurements provided the information to build a comprehensive database, which defines the seasonal and spatial optical dynamics of this Salish Sea. These data were evaluated using an empirical orthogonal function analysis to understand the variability of above-water remote sensing reflectance in relation to the biogeochemical and optical measurements. Lastly, a hierarchical clustering analysis, applied to normalized remote sensing reflectance, enabled spectrally distinct classes to be identified.

Overall, observations showed a high variation in the biogeochemical properties in the Salish Sea, with Chla, TSM, POC, and a_{cdom} showing the most variability within the central Salish Sea, mimicking the seasonality of Fraser River discharge, consistent with previous studies in the area (Johannessen et al., 2006; Komick et al., 2009; Loos & Costa, 2010; Masson, 2002; Twardowski & Donaghay, 2001). The largest range of Chl$a$ concentrations (0.10 µg l^{-1} - 7.2 µg l^{-1}) in spring and summer aligns with known dominant phytoplankton blooms for the region, which dominate the central Salish Sea during this time period (Carswell et al., 2015; Halverson & Pawlowicz, 2013; Masson & Peña, 2009; Schweigert et al., 2013). Riverine discharge from the Fraser River is the most dominant source of particulate matter into the Salish Sea (Johannessen et al., 2003), which results in high concentrations of TSM and strong absorption by CDOM at 443 nm. This influence is significant in the central regions, consistent with previous measurements by Loos and Costa (2010).

Optically, the ranges of in-water AOPs varied considerably. Particulate scattering and backscattering, as well as absorption and attenuation showed large variation, especially in contrasting waters under different degrees of Fraser discharge influence (Table 2-2). These results are consistent with the Salish Sea initial water optical characterization by Loos and Costa (2010), and other contrasted coastal and estuarine waters including, for instance, the eastern English Channel and southern North Sea (Lubac & Loisel, 2007; Vantrepotte et al., 2012, respectively), Long Island Sound in the US (Aurin et al., 2010) and further south in Tampa Bay (Le et al., 2013b). Above-water $R_{rs}(\lambda)$ spectra also varied considerably throughout the Salish Sea. EOF and correlation analysis revealed that this variability was primarily associated with TSM concentrations, where particulate scattering and backscattering dominate, and secondarily through Chl*a* presence in more oceanic water conditions.

Waters with high TSM concentrations (> 5.0 mg l^{-1}), typically associated with plume waters, were among the most complex, both optically and biogeochemically. Prior studies estimated a high amount ($1\text{-}3 \times 10^{10}$ kg yr^{-1}) of sediment is discharged into the Salish Sea during peak runoff from the Fraser River, with limited advection out of the region into Puget Sound or the Pacific Ocean (Johannessen et al., 2003). This sediment is mostly of high inorganic nature (> 63% of the total TSM) as measured primarily in the central regions during the spring and early summer conditions, at the time of high Fraser discharge. High TSM concentrations were also commonly associated with low Chl*a* values in these plume conditions, likely because primary production is reduced by strong light attenuation (Duin et al., 2001). In fact, total attenuation, $c_t(650)$, ranged considerably (0.749 – 9.610 m^{-1}) and was on average higher than surrounding waters, as a result of the high contribution of scattering from inorganic particulates. These values are similar to those measured by Loos & Costa (2010) in the central regions during the same seasonal period (mean $c_p(650)$ = 5.14 m^{-1}) and comparable to other contrasted coastal areas, such as Chesapeake Bay (Gallegos et al., 2005) or the coastal waters of French Guiana and the Southern North Sea (Vantrepotte et al., 2012).

As illustrated in the representative samples (Figure 2-4), absorption by particles and CDOM was also highest in plume waters (2.020 m^{-1} and 0.834 m^{-1}, respectively) compared to the other sampled waters. The high fraction of inorganic material and low Chl$a$ concentrations suggests a terrigenous CDOM origin as opposed to autochthonous. Furthermore, higher than average (0.020 nm^{-1}) CDOM absorption slope coefficients, S_{cdom}, also suggest a higher ratio of fulvic to humic composition for these plume waters (Carder et al., 1989; Twardowski et al., 2004).

The measured $R_{rs}(\lambda)$ spectra demonstrated the strong effect of TSM scattering with a distinctive spectral shape that was consistently observed for waters under TSM influence. Characterized by a broad peak in reflectance near 580 nm that remained relatively high into the red, these spectra were also distinguishably higher in overall magnitude, representing the strong effects of particulate scattering and backscattering (Figure 2-5). Given the strong role of TSM, it is not surprising that the spectral shape of EOF mode 1, which explains 94.5% of the total variance, closely resembles the mean $R_{rs}(\lambda)$ spectra, especially spectra defined for water under TSM influence (Figure 2-7).

To further define the role of TSM, the particulate backscattering ratio was calculated as a proxy for the nature of particle assemblage (Boss & Pegau, 2001; Lubac & Loisel, 2007; Twardowski & Donaghay, 2001). The results showed no major variations within the samples measured, and no correlation to EOF mode 1, suggesting that the nature of backscattering material is not significant to the $R_{rs}(\lambda)$ variability but the concentration of particulate is, at least with the present data set. Additionally, the effect of absorption should be noted, particularly due to CDOM (Figure 2-8). High CDOM absorption explains the low values in the blue region of the EOF mode 1 spectrum (Craig et al., 2012; Lubac & Loisel, 2007). A low, but significant ($p < 0.05$) correlation between EOF mode 1 and Chl$a$ concentration was notable, suggesting that organic particles also contribute to light attenuation in this mode, although more data, including specific phytoplankton absorption would be needed to validate this.

Moving away from the Fraser River distributary channels, the influence of plume waters was reduced, but still notable. In these waters, TSM concentrations were still high (avg = 3.14 mg l^{-1}) but relatively lower in magnitude than those measured in plume waters (avg = 7.01 mg l^{-1}). This reduction marks an important transitional boundary between the TSM dominated plume waters and oceanic conditions. In these waters, some of the highest concentrations of Chl$a$ were measured (7.20 µg l^{-1}). Since increased primary production has been shown to be associated with increased stratification and light exposure (Collins et al., 2009; Masson & Peña, 2009; Yin et al., 1997), these waters represent optimal conditions for productivity, particularly during the spring and summer when the region is subjected to high river discharge. Furthermore, lower magnitudes of b_p, b_{bp}, a_t, and c_t compared to plume waters (Table 2-3), were also consistent with reduced TSM concentrations (Baker & Lavelle, 1984; Loos & Costa, 2010), and increased primary production due to reduced light attenuation (Allen & Wolfe, 2013; Duin et al., 2001). The fraction of scattering and absorption to attenuation, however, remained similar to those found in plume waters, with scattering dominating total attenuation (Figure 2-4b). Particulate absorption remained dominant in contribution to a_t in the green and red. This is evident in the $R_{rs}(\lambda)$ spectra, which still showed TSM influence with a broad peak near 580 nm, often masking the Chl$a$ absorption peak near 675 nm common in these waters. Lastly, absorption by CDOM accounted for nearly half of the total absorption at short wavelengths (< 500 nm), which represents an increase compared with plume waters. This resulted in low blue $R_{rs}(\lambda)$ magnitudes, producing a steeper rise in $R_{rs}(\lambda)$ from the blue to the peak in green near 580 nm.

Beyond the sediment-dominated waters in the Salish Sea, waters representing oceanic conditions showed low TSM concentrations (< 1.98 mg l^{-1}) and the lowest variability in Chl$a$ (Table 2-2), particularly in the winter months. This is consistent with the low overall magnitudes in the observed $R_{rs}(\lambda)$. In general, the optical properties showed far less variability than in the turbid and estuarine plume waters, with scattering by particles an order of magnitude less than in turbid waters, contributing more to total attenuation. Total absorption however, was dominated by CDOM absorption rather than particulates, which aligns with previous work of Loos & Costa (2010). The source of CDOM in these waters is likely autochthonous, a result of phytoplankton and detrital breakdown rather than from an allochthonous origin (Johannessen et al., 2008). The measured low values of CDOM absorption slope coefficients, S_{cdom}, further suggest a higher fulvic content (Carder et al., 1989; Twardowski et al., 2004). In fact, $a_{cdom}(\lambda)$

values were generally higher in the months following the spring phytoplankton bloom, suggesting an autochthonous dominant source of $a_{cdom}(\lambda)$ during these periods (Loos & Costa, 2010). Lastly, the magnitudes of $a_{cdom}(\lambda)$, although highly contributing to $a_t(\lambda)$, are low in comparison to waters under stronger influence of the Fraser discharge, which could explain the higher R_{rs} values in the blue.

The contribution to the overall $R_{rs}(\lambda)$ variability of the second and third EOF modes are significantly smaller (3.6% and 1.5%, respectively), but display important information regarding the $R_{rs}(\lambda)$ variation, especially in the transitional and oceanic waters described. The spectral shape of EOF mode 2 shows a near inverse relation compared to EOF mode 1, which suggests differing processes are affecting the spectra in the long and short wavelengths (Craig et al., 2012; Lubac & Loisel, 2007). This is consistent with the increased contribution of a_{cdom} to the shorter wavelengths and decreased TSM contribution to the longer wavelengths for these transitional and oceanic waters. Furthermore, particulate scatter and backscattering coefficients also demonstrate the transitional influence of TSM with a decreasing correlation from EOF mode 1 to modes 2 and 3. For EOF mode 3, which represents only 1.5% of the $R_{rs}(\lambda)$ variance, the limited but pronounced contribution of Chl*a* is revealed. The spectral shape in this mode shows well-defined peaks near 580 nm and 690 nm and a high correlation to Chl*a*, which is more significant than that of the other two modes. This is further confirmed with the red Chl*a* absorption peak near 675 nm (Chl*a* absorption) and increased pigment absorption below 450 nm, causing the blue to green reflectance ratio to decrease, while increasing the fluorescence peak (Toole & Siegel, 2001). These results suggest that the third mode represents the phytoplankton signature that is often masked by the other in-water light attenuation, such as TSM and CDOM absorption, in the majority of the $R_{rs}(\lambda)$ data collected.

The results of the hierarchical clustering analysis reveal similar results described from the EOF analysis. Of the four optical classes retrieved from HCA, two classes (Classes 1 and 2) emerged that were optically distinct, corresponding to waters linked to higher and variable TSM (Class 1) and Chl$a$ concentrations (Class 2), consistent with the EOF analysis. Again, the optical contribution of Chl$a$ to the spectra, especially in the spring, was overshadowed by the increased reflectance magnitudes from TSM when running the clustering analysis. This is consistent with the dominant spectral influence from Chl$a$ in the third EOF mode. Additionally, the influence of a_{cdom} was more noticeable in Classes 1 and 2, especially in the blue region of the spectrum and towards short wavelengths, where $R_{rs}(\lambda)$ was reduced. Although a relatively limited number of samples are available for Class 1, compared to the other classes, this class is highly representative of the plume conditions observed in the Salish Sea (Komick et al., 2009). Classes 2 and 3 represent the optically mixed transitional waters between plume and oceanic conditions, where a range of TSM influence is still strong in Class 2 and diminishes in Class 3. These two classes are characterized by high Chl$a$ concentrations (avg = 2.29 µg l^{-1}), which is often not fully represented in the $R_{rs}(\lambda)$ spectra, especially for Class 2 due to the higher TSM concentrations. Lastly, Class 4 represents the oceanic waters with the least river plume influence, characterized with seasonal low values of TSM, reduced Chl$a$ concentrations (avg = 1.26 µg l^{-1}), and consistent with low values of measured CDOM absorption. Spectrally, this class was distinguished by overall low values of $R_{rs}(\lambda)$ with higher magnitudes in the blue, again likely due to low a_{cdom} .

Seasonally, a mix of the four optical classes were found in the Salish Sea in the spring, with Classes 1 and 2 tightly confined to the central regions, Class 3 in the central and northern regions, and Class 4 in the central and southern areas (Figure 2-10). This is consistent with peak discharge of the Fraser River and strong spring phytoplankton blooms during this period (Allen & Wolfe, 2013; Carswell et al., 2015; Gower et al., 2013; Masson & Peña, 2009). Transitioning into summer months, Class 1 was still confined to the central areas, near the Fraser River, but Classes 2-4 become widely distributed throughout the study site, with Class 4 dominating, suggesting that less productive oceanic waters are more widely distributed during the summer. In the fall, Class 1 is not present, which is not surprising given the lower river discharge at this time, although this could be a function of the sampling approach missing the confined Fraser River plume. Class 2 is confined to the Puget Sound region during the fall, likely an expression of a late summer phytoplankton bloom, which are documented from May until September (Mackas & Harrison, 1997; Winter et al., 1975), although a small bloom is expected in the SoG during this period as well (Carswell et al., 2015; Masson & Peña, 2009). Lastly, Class 3 and 4 dominate throughout the study site, especially in the fall, which is again likely due to reduced river discharge. To further refine the optical characterization of these waters, more sampling would be required on higher spatial and temporal scales to refine the dominant trends observed here.

The results of the hierarchical clustering analysis on the normalized $R_{rs}(\lambda)$ spectra serve to separate the different bio-optical regimes present in the Salish Sea. Although four classes were uniquely determined from $R_{rs}(\lambda)$, two classes emerged with distinct bio-optical regimes, corresponding to a large TSM occurrence and waters less impacted by TSM. The results of this study indicate that optically the Salish Sea is dominated by two distinctly different controls on $R_{rs}(\lambda)$ variability. This suggests that a regional algorithm for Chl$a$ retrieval using $R_{rs}(\lambda)$ may be inadequate due to these inherent differences. For instance, the standard empirical OC3M model, which relies on the blue to green ratios to generate Chl$a$ concentrations, has a set of developed coefficients which were defined based on a global dataset of oceanic conditions (O'Reilly, 2000). As identified in this study, these bands are differentially impacted by TSM and CDOM influences that can vary independently of Chl$a$. Consequently, inaccurate Chl$a$ concentrations are expected under varying TSM and CDOM variations unless parameterized to accommodate these changes, which is consistent with the previous study in this region (Komick et al., 2009). This also has been the case for several coastal waters, as demonstrated by Garcia et al. (2005), Mustapha et al. (2012), Shen et al. (2010), Werdell et al. (2009), and the results in Chapter 3. Therefore, class specific inversion models would likely be more appropriate for this complex coastal region and the results of this study provide the necessary first steps towards identifying the bio-optical regimes needed for optimization.

2.6 Conclusion

The goal of this research was to characterize the spatial and temporal bio-optical and biogeochemical properties of the contrasted surface waters of the Salish Sea. While previous studies (Loos & Costa, 2010; Loos et al., 2009), have defined three optical masses: river plume, estuarine, and deep northern waters, this study aimed to expand this to a broader region and over all seasons. By characterizing the variability in remote sensing reflectance and related bio-optical and bio-geochemical regimes, this study provided a refined link to future improvements of satellite-based algorithms for Chl*a* retrievals in the Salish Sea.

Discrete hyperspectral measurements of above-water $R_{rs}(\lambda)$ provided the baseline input to understanding the trends in IOPs and bio-geochemical variables associated with these complex waters. Hierarchical clustering analysis revealed four dominant optical classes across all sub-regions in the Salish Sea throughout the year. A considerable amount of variability in the classification can be explained by the proximity to riverine discharge, with high strong influences from TSM and terrestrial CDOM, which operate on a seasonal time scale. Regions under the influence of plume waters were defined as Class 1, dominated by the highest $R_{rs}(\lambda)$ magnitudes in the study area, particularly in the red spectra, and strong absorption by CDOM in the short wavelengths. Confined to spring and summer conditions in the central Salish Sea, this water class was heavily influenced by particulate matter, most likely terrestrial sourced. Class 2 waters were defined by transitional plume conditions, with a distinct Chl*a* fluorescence peak near $R_{rs}(690)$ and a strong TSM signal in the red spectra, as evident by high particulate scattering and backscattering. These waters were also confined to the central Salish Sea during the spring and summer, but were only found in the Puget Sound during the fall, where blooms are still common. Class 3 waters showed similar traits to Class 2 with the exception of TSM playing a much smaller role on $R_{rs}(\lambda)$, resulting in a more defined fluorescence peak and low scattering and backscattering values for the samples. This class was present in the central Salish Sea during the spring, Puget Sound during the summer, and throughout the study site in the fall. Lastly, Class 4 represented clear oceanic water conditions, with low Chl$a$ and TSM concentrations, and consequently low $R_{rs}(\lambda)$ magnitudes. Low values of $a_{cdom}(\lambda)$ resulted in elevated $R_{rs}(\lambda)$ in the blue spectra, which distinguishes this class from all others.

Clustering analysis of the AOP data in the Salish Sea demonstrated that this complex estuarine water body could be simplified into four classes with specific remote sensing reflectance spectral shapes and associated bio-optical environments. Although four distinct classes were found, more *in situ* data would be useful to further refine this method, particularly for classes where sample size was small such as for Classes 1 and 2. Additionally, specific absorption coefficient data would be important to further understand the absorption budgets, which are likely influencing the current optical regimes distinguished here. This would allow a secondary clustering analysis based on IOPs to compare to the current AOP classification. The next stage in this research will focus at applying the results of this study to create sub-regional algorithms for improved satellite-based Chl$a$ retrievals. This information will provide fisheries management accurate information to study ocean primary production and biogeochemical cycles, which is ultimately linked to the health status of the fisheries on this coast.

Chapter 3 Regional chlorophyll-a algorithm evaluation for MODIS-Aqua and Sentinel-3 in the Salish Sea, Western Canada

3.1 Abstract

In this study an optical classification was used to evaluate and parameterize the OC3M, two-band ratio, FLH, and modified FLH empirical models for improved estimation of satellite derived Chl*a* in the Salish Sea, located on the west coast of Canada. *In situ* biogeochemical and optical measurements were used in conjunction with above-water hyperspectral remote sensing reflectance, $R_{rs}(\lambda)$, from five field campaigns and biweekly trips aboard a ship of opportunity to understand the localized optical variability of these Case 2 coastal waters. A method was developed to characterize water types into an estuarine or oceanic class, based on individual spectra, which enabled us to significantly increase algorithm performance by developing a regionally tuned model for each water type. Algorithms were first parameterized for the entire region and then re-parameterized for class specific data. Results showed a systematic overestimation of low Chl*a* concentrations and underestimation for higher Chl*a* values for all four models tested with the regional data, with the modified version of the standard FLH model showing the best performance (R^2 ~ 0.40). Algorithm accuracy was significantly improved for the class specific data with the two-band ratio showing high correlation (R^2 ~ 0.71) to *in situ* Chl*a* for the estuarine class waters and the modified FLH algorithm for the oceanic class conditions (R^2 ~ 0.70). These results demonstrate the benefit of using optical classification for parameterizing contrasted coastal waters in order to more accurately retrieve Chl*a* concentrations using satellite ocean-colour data. This provides valuable information for an ecosystem based approach to effectively monitor the health of the Salish Sea.

3.2 Introduction

3.2.1 Background

The use of satellite ocean colour data for deriving biophysical properties has long been recognized as a useful tool for studying ocean primary production and other biogeochemical cycles (e.g., Antoine et al., 1996; Behrenfeld et al., 2006; Boyce et al., 2010; Field, 1998). Ocean colour satellites such as the NASA Moderate Resolution Imaging Spectroradiometer (MODIS-Aqua) or the upcoming Sentinel-3 Ocean and Land Colour Instrument (S3-OLCI) can provide the opportunity to study the health of coastal and marine ecosystems at temporal and spatial scales that are otherwise difficult to obtain with direct field measurements (Mouw et al., 2015; Verrelst et al., 2012; Werdell et al., 2009). These satellites provide large-scale measurements of water-leaving radiances after interaction with the atmosphere in the visible and infrared parts of the spectrum. Generally, atmospheric attenuation and solar illumination variability are minimized through correction algorithms, thus resulting in water-leaving reflectance (Gordon & Wang, 1994). The reflectance signal is then used as input to bio-inversion algorithms to retrieve biogeochemical parameters such as Chl*a* concentrations.

Typically, empirical algorithms based on blue/green reflectance ratios have been used as input to retrieve Chl*a* in oceanic waters (i.e. Case 1 waters; e.g. Gordon & Morel, 1983; O'Reilly et al., 1998) with reasonable accuracy, but in coastal estuarine waters (i.e. Case 2; e.g. Morel & Prieur, 1977), other optically active constituents (e.g. CDOM and particulates) make it difficult to retrieve Chl*a* (Chen et al., 2012; Darecki & Stramski, 2004; Garcia et al., 2006; Joergensen, 2004; Le et al., 2013a). To overcome this challenge, recent efforts have been made to modify existing standard algorithms (e.g., Garcia et al., 2005; Gitelson et al., 2007; Le et al., 2013a; Mustapha et al., 2012; Shen et al., 2010; Werdell et al., 2009). For instance, utilizing spectral bands in the red and near-infrared, Le et al. (2013) and Moses et al. (2009) improved the Chl*a* retrieval accuracy by deriving reflectance based algorithms that are less dependent on atmospheric correction and CDOM absorption, which is typically responsible for inaccuracies of Chl*a* retrievals based on blue and green bands (Bailey & Werdell, 2006; Gitelson et al., 2007; Le et al., 2013a). These algorithms are then parameterized with regional data to calibrate the models to the localized complexities of Case 2 waters, such as high turbidity. Through this technique, a direct relation between $R_{rs}(\lambda)$ and Chl*a* concentration is established using statistical techniques, which are computationally more advantageous (Matthews, 2011). These algorithms can then be regionally tuned with coefficients that align to localized water conditions, or specific water types, which has seen success in other coastal regions with improved Chl*a* algorithm retrievals (Feng et al., 2005; Lubac & Loisel, 2007; Moore et al., 2009).

The Salish Sea, located on the west coast of Canada and northwest coast of the U.S., is a typical Case 2 type of water (Chapter 2) (Komick et al., 2009; Loos & Costa, 2010). However, significant challenges still exist in this region for accurately measuring satellite derived Chl*a* (Carswell et al., 2015; Gower et al., 2013; Komick et al., 2009). This is primarily due to high concentrations of suspended sediment input into the region, predominantly from the Fraser River, which has a mean annual sediment discharge of 1-3 × 10^{10} kg (Johannessen et al., 2003). As shown in Chapter 2, these highly turbid waters enhance $R_{rs}(\lambda)$ due to increased scattering from particulate matter (Komick et al., 2009;

Loos & Costa, 2010), which can alter the spectral features associated with Chl*a* and, as a result, influence estimates of Chl*a* (Komick et al., 2009). Additionally, terrestrial inputs of allochthonous CDOM from river runoff and autochthonous CDOM formed from *in situ* production, have been shown to confound Chl*a* estimates by dominating total absorption, especially in the short blue wavelengths (Komick et al., 2009; Loos & Costa, 2010; Twardowski & Donaghay, 2001).

The objective of this study was to improve ocean-colour Chl*a* estimates for the Salish Sea by defining reflectance-based empirical algorithms specifically for this region. Biophysical and *in situ* hyperspectral radiometric measurements were first sub-regionalized into sediment and clearer oceanic waters based on an optical classification (Chapter 2). Corresponding reflectance values were then modeled to MODIS and Sentinel-3 spectral bands and used to evaluate the following algorithms: the standard blue-green band ratio OC3M empirical algorithm (O'Reilly, 2000), a two-band ratio algorithm of the form $R_{rs}(\lambda_2)/R_{rs}(\lambda_1)$, the fluorescence line height (Gower et al., 1999), and a combined FLH and band ratio algorithm. Semi-analytical approaches were not considered here because of the results in Komick et al (2009), which showed a need of accurate corrections in the short blue, which is usually a problem due to difficulties for the atmospheric correction approach (Bailey & Werdell, 2006; Carswell et al., 2015; Darecki & Stramski, 2004).

3.2.2 Bio-optical algorithms

Ocean chlorophyll algorithm

The first empirical algorithm tested was the Ocean Chlorophyll algorithm, first developed for the SeaWiFS sensor (O'Reilly, 2000) and adapted to subsequent sensors. The MODIS version (OC3M) is derived from R_{rs} ratios as

$$Chl = 10^{\left(c_0+c_1R_{3M}+c_2R_{3M}^2+c_3R_{3M}^3+c_4R_{3M}^4\right)} \tag{3.1}$$

$$R_{3M} = \log_{10}\left(\frac{max[R_{rs}(443), R_{rs}(488)]}{R_{rs}(547)}\right) \tag{3.2}$$

where c_0-c_4 are coefficients determined from nonlinear regression between log transformed Chl*a* values and the R_{3M} ratio, defined in Eq. (3.2) as the greater of the reflectance of blue wavelengths divided by the reflectance of the green reference band. The adaptation for Sentinel-3 (OC3S3) follows that of MERIS (Werdell, 2010), with the 547 nm band replaced with 560 nm, corresponding to Sentinel-3 band 6,

$$Chl = 10^{\left(c_0+c_1R_{3S}+c_2R_{3S}^2+c_3R_{3S}^3+c_4R_{3S}^4\right)} \tag{3.3}$$

$$R_{3S} = \log_{10}\left(\frac{max[R_{rs}(443), R_{rs}(490)]}{R_{rs}(560)}\right) \tag{3.4}$$

Two-band ratio

A two-band ratio algorithm of the form $R_{rs}(\lambda_2)/R_{rs}(\lambda_1)$, where λ_1 is a green band and λ_2 is a red band was tested. It was developed by taking the regression of *in situ* Chl*a* concentrations against the log transformed band ratio of $R_{rs}(667)/R_{rs}(547)$ for MODIS and $R_{rs}(665)/R_{rs}(560)$ for Sentinel-3. The 665 nm band was chosen to capitalize on maximum Chl*a* absorption, which typically creates a minimum in R_{rs} near 665 nm

(Morel & Prieur, 1977). The 547 nm and 560 nm bands were chosen as a way to normalize this signal to the global R_{rs} maximum in an effort to accommodate the role of backscattering from water turbidity for MODIS and Sentinel-3, respectively (Gitelson et al., 2007). These bands avoid the blue wavelengths which are recognized for errors associated with atmospheric correction and absorbing aerosols in the atmosphere, as well as absorption from CDOM (Bailey & Werdell, 2006; Gitelson et al., 2007; Le et al., 2013a). Additionally, other studies have demonstrated that this simple band combination was particularly well correlated with Chl*a* concentrations in several coastal regions and inland waters (Floricioiu et al., 2003; Gitelson, 1992; Le et al., 2013a; Tzortziou et al., 2007).

Fluorescence line height

The fluorescence of *in situ* Chl*a* gives a maximum near 685 nm (Morel & Prieur, 1977), which can be used to estimate concentrations of Chl*a* (Gower, 1980). To accomplish this, the fluorescence line height (FLH) algorithm uses the height of the reflectance peak near 681 nm, calculated from an interpolated baseline representing the spectrum without fluorescence (Gower et al., 1999). In its simplest form, the baseline is determined by linear interpolation and the algorithm takes the form (Gower et al., 1999),

$$FLH_{MODIS} = R_{rs}(678) - \left(R_{rs}(746) + \frac{746-678}{746-667}\left(R_{rs}(667) - R_{rs}(746)\right)\right) \qquad (3.5)$$

$$FLH_{Sentinel-3} = R_{rs}(681) - \left(R_{rs}(709) + \frac{709-681}{709-665}\left(R_{rs}(665) - R_{rs}(709)\right)\right) \qquad (3.6)$$

The adaptation for Sentinel-3 bands follows those of MERIS, which utilizes the bands closest to 685 nm, namely the 665 and 709 nm bands for the baseline and the 681 nm band for the fluorescence. By choosing the bands closely centered around 685 nm errors can be minimized due to contamination from uncorrected atmospheric signals (Gower et al., 1999).

Combined band ratio and FLH

Previous studies have examined the impact of non-algal materials on the fluorescence signal at 678 nm; increasing CDOM absorption tends to decrease the radiance signal including fluorescence peak (McKee et al., 2007) and particle backscattering in turbid waters tends to increase radiance levels, which can mask some of the fluorescence peak (Gower et al., 1999; McKee et al., 2007). The baseline correction in the FLH algorithm effectively minimizes the effects of CDOM but it is not as effective at minimizing backscattering caused by mineral particles (Hoge et al., 2003; McKee et al., 2007). In fact, it is recognized that the FLH algorithm can underestimate Chl*a* in coastal waters due to the inability to resolve the fluorescence peak over increased background reflectance levels in turbid waters (Gower et al., 1999; McKee et al., 2007; Zhao, Temimi, & Ghedira, 2015). To address this, a factor applied to the standard FLH algorithm in the form of two-band ratio between 678 nm and 665 nm for MODIS and 681 nm and 673 nm for Sentinel-3 is proposed. This regionally adjusted FLH model has the following form,

$$ModFLH_{MODIS} = FLH \times \frac{R_{rs}(678)}{R_{rs}(667)} \tag{3.7}$$

$$ModFLH_{Sentinel-3} = FLH \times \frac{R_{rs}(681)}{R_{rs}(674)} \tag{3.8}$$

By using the ratio of the band representing the fluorescence peak to the band just prior, 665nm, we are able to capitalize on the increase in radiance around 685 nm and the absorption properties of Chl*a* (Morel & Prieur, 1977; Neville & Gower, 1977). The premise is that the Chl*a* concentration is proportional to the reflectance band for fluorescence (numerator) and inversely proportional to the Chl*a* absorption band near 665 nm (denominator). The additional band availability with Sentinel-3 allows us to utilize a band ratio closer to the fluorescence peak, which avoids some of the issues associated with the baseline correction in the FLH algorithm which is not effective at minimizing backscattering caused by mineral particles (Hoge et al., 2003; McKee et al., 2007) (Figure 3-1).

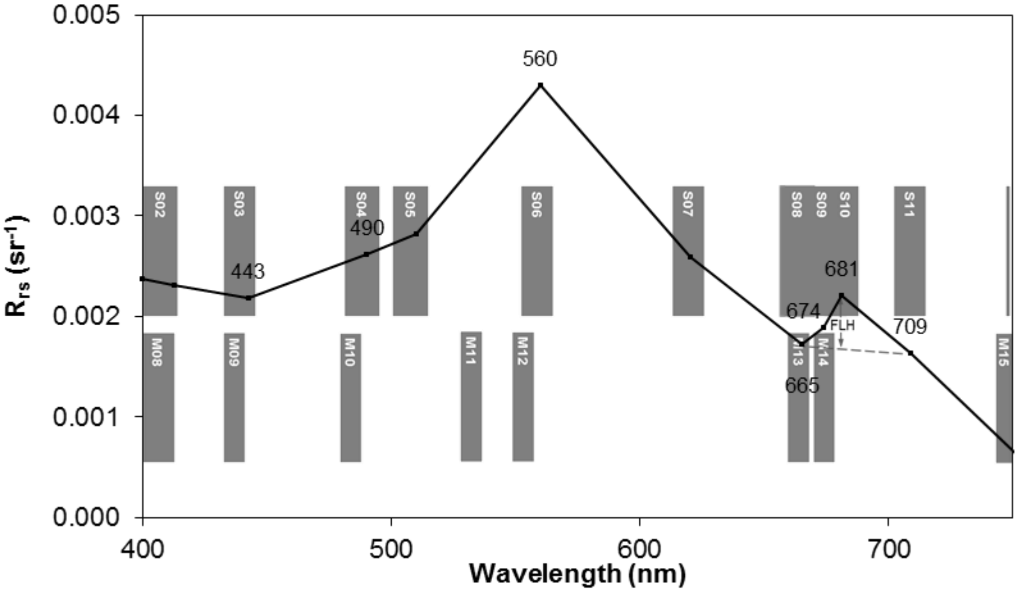

Figure 3-1 Sample R_{rs} spectra showing the fluorescence line height (FLH) and bands centered around the fluorescence peak, which were used in the modified FLH algorithm. Grey vertical bars denote the minimum and maximum boundaries for the bands of Sentinel-3 (S) and MODIS (M).

3.3 Data collection and methods

3.3.1 Study Area

The Strait of Georgia (SoG), Puget Sound, and Strait of Juan de Fuca, collectively defined as the *Salish Sea*, compose a large semi-enclosed estuarine system located on the west coast of Canada and the Pacific Northwest portion of the U.S.A. (Figure 3-2). In many coastal estuaries, dominant nutrient fluxes occur through the open ocean, but in the Salish Sea connections to the Pacific Ocean are restricted through the Strait of Juan de Fuca in the south and the Johnstone Strait in the north, therefore nutrients are predominantly from deep water exchange in the Juan de Fuca Strait (Mackas & Harrison, 1997). In the southern system, the Puget Sound behaves like a partially mixed estuary, exchanging flow into the Juan de Fuca Strait, along with the SoG (Sutherland et al., 2011). Strong fresh water influxes drive estuarine circulations in these regions which are then subject to wind stresses and strong tidal mixing (Li et al., 2000; Sutherland et al., 2011). In the SoG, the most dominant discharge is from the Fraser River into the SoG, which typically peaks in mid-June during the freshet (average ~ 7000 m^3s^{-1}) (Masson, 2002; Sutherland et al., 2011). In the Puget Sound, the Skagit and Snohomish river systems provide a similar freshwater influx (average ~ 7000 m^3s^{-1}) peaking around June (Sutherland et al., 2011; USGS, 2015). These riverine systems, along with tidal mixing, have been shown to largely influence the productivity in these waters (Johannessen et al., 2003). In the SoG, for instance, phytoplankton blooms typically occur in the spring in conjunction to peak Fraser River outflow, followed by a smaller bloom in the fall (Allen

& Wolfe, 2013; Carswell et al., 2015; Collins et al., 2009; Gower et al., 2013; Masson & Peña, 2009).

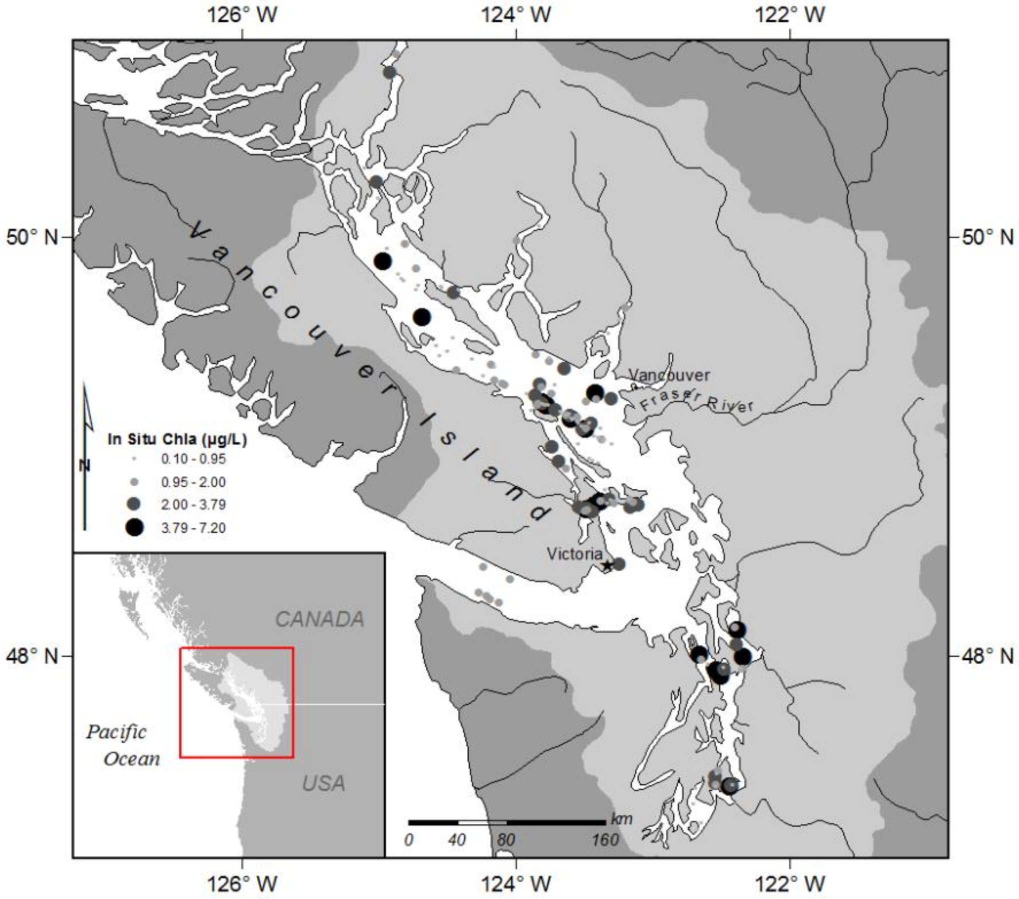

Figure 3-2 Study area map showing spatial distribution of the Chl*a* data set in the Salish Sea. Values for Chl*a* concentrations are shown as proportional symbols.

3.3.2 In situ datasets

In order to test standard and develop new models, *in situ* data were collected on five research cruises aboard the W.E. Ricker and bi-weekly trips on the BC Ferry Queen of Alberni from September of 2012 to October of 2013. A total of 145 stations were sampled for water property and bio-optical data. At each station above-water remote sensing reflectance, $R_{rs}(\lambda)$, was measured and processed with scientific-communityaccepted protocols (Hooker & Morel, 2003; Ruddick et al., 2006). Additionally, water samples were collected at surface depths (< 0.5 m) and processed in triplicates, within four hours, for concentrations of Chl$a$ and associated pigments, total suspended matter (TSM), and $a_{cdom}(\lambda)$.

Water Samples

To measure Chl$a$ and associated pigment concentrations, water samples were passed through 0.7 µm Whatman GF/F 47mm filters under low vacuum and rinsed with 100 mL of deionized (DI) water before being stored at -20°C for further analysis. Once in the laboratory, samples were extracted in 10 mL of 90% acetone solution under dim light conditions, stored for 24 h at -4°C, and centrifuged to minimize cellular debris (Arar, 1997). 2 mL of each sample were then transferred to amber vials using a syringe fitted with a 0.45 µm inline filter and placed into a Dionex HPLC analyzer to be processed with an eluent gradients for determining Chl$a$ and other pigment concentrations. Standard stocks of Chl$a$ and Chl$b$, obtained from DHI Water & Environmental (Denmark) were used to calibrate the measurements, along with a multiple pigment standards with an additional certified Chl$a$ standard for comparison.

For TSM concentrations, surface water samples were filtered through pre-combusted and pre-weighed 0.7 µm Whatham GF/F 47 mm filters. After filtration, filters were dried at 60ºC for six hours then weighed. This process was repeated three times or until a constant weight was achieved (Eaton et al., 2005). Weights were normalized to the amount of water filtered to give a final TSM concentration. Filtrate from the TSM samples was then filtered a second time through 0.2 µm PALL Supor ® membrane disk filters and processed with an Ocean Optics USB 4000 spectrophotometer (300-850 nm, 0.2 nm resolution), for CDOM absorption. Absorption was derived using Beer-Lambert's Law,

$$a_{cdom}(\lambda) = 2.303\frac{A(\lambda)}{l}, \quad (m^{-1}) \tag{3.9}$$

where $A(\lambda)$ is spectral absorbance and l is the length of the instrument cuvette (Pegau et al., 2003). Residual offsets were removed by subtracting the average absorption coefficient from 790 to 800 nm according to Mitchell et al. (2002). Lastly, the slope of the absorbance spectrum, S_{cdom}, was calculated by fitting a single exponential decay function to the spectra in the range of 400 to 700 nm (Del Vecchio & Blough, 2002).

Optical measurements

$R_{rs}(\lambda)$ was measured for 93 stations using a Satlantic HyperSAS (351-797, 1 nm resolution) sensor array which includes sensors for water-surface radiance, $L_t(\lambda)$, sky radiance, $L_s(\lambda)$, and sky irradiance, $E_s(\lambda)$, all mounted on a platform conforming to a fixed geometry outlined by Hooker and Morel (2003). Field data were converted to $R_{rs}(\lambda)$ according to Ruddick et al (2006)

$$R_{rs}(\lambda) = \frac{L_t(\lambda) - \rho_{sky}L_s(\lambda)}{E_s(\lambda)}, \quad (sr^{-1}) \tag{3.10}$$

$$\rho_{sky} = 0.0256 + 0.00039W + 00000034W^2, when\ \frac{L_s(750)}{E_s(750)} < 0.05 \tag{3.11}$$

$$\rho_{sky} = 0.0256, when\ \frac{L_s(750)}{E_s(750)} \geq 0.05 \tag{3.12}$$

where ρ_{sky} is the proportion of sky radiance that is reflected off the surface of the water, dependent on wind speed, W, measured in the field, and the proportion of cloud cover identified by the sky radiance measurements. For the remaining 52 stations where *in situ*

$R_{rs}(\lambda)$ measurements could not be made, Hydrolight 5 (Sequoia Scientific Inc.) was used to simulate these values using radiative transfer theory. A four-component Case 2 model was chosen, which is based on pure water, chlorophyll bearing particles, CDOM absorption that does not co-vary with Chl*a*, and mineral particles. A subgroup (n = 34) of data, with a complete set of *in situ* $R_{rs}(\lambda)$, biogeochemical, and optical data was used to validate the assumptions used in Hydrolight. Beyond 600 nm, a constant underestimation was observed for the modelled $R_{rs}(\lambda)$ spectra. This was accounted for by applying a derived offset to the modelled spectra (Chapter 2).

Final $R_{rs}(\lambda)$ values were aggregated to represent the signals that would be measured by satellite sensors, $R_{rs}(\lambda_i)$, at band *i*, centered at wavelength λ_i. The signal response functions (SRF(λ)) of MODIS (Feldman, 2012) and Sentinel-3 (Pelloquin & Nieke, 2012) were used to weight the ranges of *in situ* $R_{rs}(\lambda)$ for each band according to:

$$R_{Sensor\ Band\ i} = C \times \sum_{\lambda_{min}}^{\lambda_{max}} R_{in\ situ}(\lambda) \times SRF_{Sensor\ Band\ i}(\lambda) \tag{3.13}$$

where C is the inverse sum of the $SRF_{Sensor\ Band\ i}(\lambda)$, and λ_{min}, λ_{max} are the minimum and maximum wavelengths in the given band. These simulated bands were then used as inputs for the implementation of the tested algorithms (Table 3-1).

Table 3-1 Empirical algorithms tested in this study.

Sensor	Algorithm Form	Abbreviation
MODIS	$max\{R_{rs}(443), R_{rs}(488)\}/R_{rs}(547)$	OC3M
Sentinel-3	$max\{R_{rs}(443), R_{rs}(490)\}/R_{rs}(560)$	OC3S3
MODIS	$R_{rs}(667)/R_{rs}(547)$	MODIS R_{547}^{667}
Sentinel-3	$R_{rs}(665)/R_{rs}(560)$	S3 R_{560}^{665}
MODIS	$R_{rs}(678) - 0.860R_{rs}(667) - 0.140R_{rs}(746)$	$\text{FLH}_{\text{MODIS}}$
Sentinel-3	$R_{rs}(681) - 0.636R_{rs}(665) - 0.364R_{rs}(709)$	FLH_{S3}
MODIS	$FLH \times R_{rs}(678)/R_{rs}(667)$	$\text{ModFLH}_{\text{MODIS}}$
Sentinel-3	$FLH \times R_{rs}(681)/R_{rs}(674)$	$\text{ModFLH}_{\text{S3}}$

3.3.3 Chl*a* algorithm development

As a first step to evaluate the empirical reflectance-based Chl*a* algorithms listed in Table 3-1, the entire set of MODIS and Sentinel-3 simulated $R_{rs}(\lambda)$ bands was used to define a regional algorithm for the Salish Sea. For each tested algorithm, a regression was applied between the reflectance signal algorithm form (i.e. band ratio, FLH, or ModFLH) and *in situ* Chl*a* values. Because the Chl*a* data ranged over nearly two orders of magnitude, a regression was also performed between the log transformed data sets (O'Reilly et al., 1998). A non-linear function was then fitted to regression data to define the optimal relationship between the two variables.

The second step considered the distinct optical classes of the Salish Sea, with defined bio-physical ranges, based on above water spectral $R_{rs}(\lambda)$ defined in the previous chapter, to evaluate possible improved accuracy of the reflectance-based Chl*a* retrievals. Using hierarchical clustering analysis (HCA) on normalised $R_{rs}(\lambda)$ spectra, we defined four classes. Classes 1 and 2 were characterized by overall high reflectance values, particularly in the red ($R_{rs}(560)$ ~ 0.03 sr^{-1}), with moderate to high TSM concentrations (average 7.01 mg l^{-1}), indicating turbid estuarine waters. Classes 3 and 4 were less influenced by TSM, as indicative of lower TSM concentrations (average 2.49 mg l^{-1}) and lower overall $R_{rs}(\lambda)$ magnitudes ($R_{rs}(560)$ avg 0.004 sr^{-1}), but showed relatively stronger fluorescence signals. For the purposes of this study, simulated $R_{rs}(\lambda)$ MODIS and Sentinel-3 band signals (B) were used to evaluate the suitability of class-specific algorithms. Given the spectral similarity of classes 1 & 2 and 3 & 4, and for simplification of the analysis, the classification scheme considered two classes: a estuarine class comprised of classes 1 and 2, and an oceanic class comprised of classes 3 and 4. $R_{rs}(\lambda)$ thresholds were then defined for each class, estuarine and oceanic, to separate the spectra into either class using a two-step approach. For MODIS this was defined as,

Step 1:

If (B11/B12) $R_{rs}(530)/R_{rs}(547)$ $\geq 0.92 \rightarrow$ **Oceanic Class**
$< 0.92 \rightarrow$ proceed to step 2

Step 2:

If (B13/B12) $R_{rs}(667)/R_{rs}(547)$ $> 0.35 \rightarrow$ **Estuarine Class**
$\leq 0.35 \rightarrow$ **Oceanic Class**

And similarly for Sentinel-3,

Step 1:

If (B5/B5) $R_{rs}(510)/R_{rs}(560)$ $\geq 0.79 \rightarrow$ **Oceanic Class**
$< 0.79 \rightarrow$ proceed to step 2

Step 2:

If (B13/B12) $R_{rs}(665)/R_{rs}(560)$ $> 0.32 \rightarrow$ **Estuarine Class**
$\leq 0.32 \rightarrow$ **Oceanic Class**

The models listed in Table 3-1 were then re-evaluated for both the estuarine and the oceanic classes using the same regression techniques as above.

To evaluate the performance of the algorithm derived Chl*a* compared to *in situ* measured Chl*a*, the Root-Mean-Square-Log-Error (*RMSE$_{log}$*) was calculated, defined as (Garcia et al., 2005; Moore et al., 2014),

$$RMSE_{log} = \sqrt{\frac{\sum_{i=1}^{N}\left(\log_{10} Chl_{alg} - \log_{10} Chl_{meas}\right)^2}{N}} \tag{3.14}$$

where Chl_{alg} is the ith algorithm derived Chl*a* concentration and Chl_{meas} is the ith *in situ* Chl*a* measurement. N is the number of valid retrievals. The error, δ, associated with each data point and the mean error, or bias, was defined as (Moore et al., 2014; Mustapha et al., 2012; Szeto et al., 2011),

$$\delta_i = \log Chl_{alg} - \log Chl_{meas} \tag{3.15}$$

$$bias = \frac{1}{N}\sum_{i=1}^{N} (\log_{10} Chl_{alg} - \log_{10} Chl_{meas}) \tag{3.16}$$

The slope (*S*), intercept (*I*) and the coefficient of determination (R^2) were also computed to test the performance of the algorithms using linear regression between the estimated Chl*a* values and those measured *in situ* (IOCCG, 2006; O'Reilly et al., 1998).

3.4 Results

3.4.1 Bio-optical properties

Overall a wide variability in the bio-optical water properties was observed in the Salish Sea. Table 3-2 summarizes the statistical parameters of each measured property for the regional data set as well as the class specific ranges. Chl*a* concentrations varied one order of magnitude throughout the study site and in each water class. The maximum Chl*a* values (7.20 µg l^{-1}) were measured in the central Salish Sea during the spring phytoplankton blooms and the lowest Chl*a* concentrations were observed in the north towards Johnstone Strait. TSM concentrations varied significantly with a range of 0.82 mg l^{-1} in early March to 20.69 mg l^{-1} in May, corresponding to peak Fraser River discharge in the central Salish Sea. Absorption by CDOM at 443 nm, $a_{cdom}(443)$, also varied significantly (0.007 – 3.072 m^{-1}), with higher values of allochthonous CDOM absorption (avg S_{cdom} = 0.020 nm^{-1}) associated with high sediment concentrations in plume influenced waters, and autochthonous CDOM absorption (avg S_{cdom} = 0.018 nm^{-1}) found in more oceanic waters, where Chl$a$ concentrations were higher.

Table 3-2 Summary of in situ bio-optical variables measured and separated into estuarine and oceanic classes. Average in bold, standard deviation in brackets, and minimum and maximum values in square brackets.

Variable	**Regional**	**Estuarine Class**	**Oceanic Class**
Chl$a$ (µg l^{-1})	**1.64** (1.51) [0.10 – 7.20] n = 142	**2.15** (2.05) [0.21 – 7.20] n = 19	**1.56** (1.39) [0.10 – 6.83] n = 123
TSM (g m^{-3})	**3.09** (2.73) [0.82 – 20.69] n = 143	**7.01** (5.55) [1.55 – 20.69] n = 19	**2.49** (1.07) [0.82 – 5.66] n = 124
a_{cdom} (443) (m^{-1})	**0.525** (0.409) [0.007 – 3.072] n = 143	**1.008** (0.785) [0.182 – 3.072] n = 19	**0.451** (0.238) [0.007 – 1.551] n = 124
S_{cdom} (nm^{-1})	**0.018** (0.004) [0.009 – 0.028] n = 143	**0.020** (0.003) [0.017 – 0.028] n = 19	**0.018** (0.004) [0.009 – 0.027] n = 124

3.4.2 Remote sensing reflectance

Figure 3-3 shows the above-water $R_{rs}(\lambda)$ spectra obtained for the range of 400 – 750 nm, separated into the defined estuarine and oceanic classes, using the thresholds defined in section 3.3.3. In Step 1 of this method, spectra representing high TSM (high reflectance peak near 560 nm) and or strong CDOM absorption (low blue reflectance) were distinguished with $R_{rs}(530)/R_{rs}(547)$ < 0.92 for MODIS and $R_{rs}(510)/R_{rs}(560)$ < 0.79 for Sentinel-3, indicating estuarine waters (Figure 3-3a). Ratios greater than these defined thresholds indicated TSM and CDOM absorption influence was low, and spectra were classified as oceanic waters (Figure 3-3b). In Step 2, spectra designated as estuarine class were re-evaluated for a strong Chl$a$ absorption (reduced reflectance near 665 nm) feature. If Chl$a$ presence was high, Chl$a$ absorption was expected to be high, resulting in low ratios, $R_{rs}(667)/R_{rs}(547) \leq 0.35$ for MODIS and $R_{rs}(665)/R_{rs}(560)$

≤ 0.32 for Sentinel-3, and spectra were re-classified as oceanic (Figure 3-3b). The final result produced two distinct trends in the spectral shapes, corresponding to different water classes: (1) estuarine waters (high TSM, wide-ranging Chl*a*, high CDOM) (Figure 3a); (2) oceanic waters (low TSM, moderate Chl*a*, low CDOM) (Figure 3-3b).

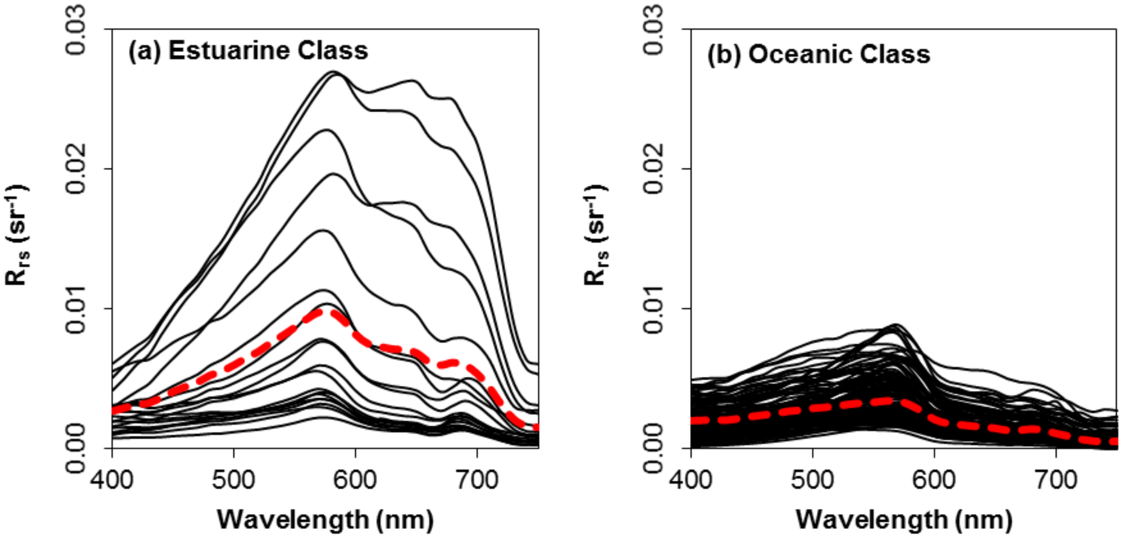

Figure 3-3 $R_{rs}(\lambda)$ spectra for **(a)** estuarine class and **(b)** oceanic class. Averages for each class are shown as red dashed lines.

The reflectance in the blue for the estuarine class is generally low relative to green and red, likely due to absorption by CDOM and phytoplankton. In contrast, the oceanic class spectra (Figure 3-3b) show higher values in the blue compared to the green, likely because Chl*a* absorption is more influential than CDOM absorption in these waters. For both classes a large variability in the spectra is observed in both the green and red wavelengths with increases in chlorophyll pigments. For high Chl*a* samples, reflectance peaks between 560 – 580 nm are well-defined (narrow) with a decrease near 665 nm, corresponding to Chl*a* absorption. For samples with lower Chl*a* concentrations, the peak in the green is less pronounced (broad) and tends to mask the decrease in reflectance near

665 nm. Further into the red wavelengths, many spectra showed a prominent peak near 680 – 690 nm, corresponding to Chl*a* fluorescence (Gower, 1980; Huot et al., 2005; Neville & Gower, 1977). Variability in TSM concentration is significant to the magnitude variability of $R_{rs}(\lambda)$, with scattering by particles contributing to an increase in the overall magnitude of the observed spectra and the peak near 580 nm, most notably for the estuarine class (Figure 3-3a). This is consistent with other studies in turbid productive waters (Gitelson et al., 2007; Novoa et al., 2011; Shen et al., 2010). $R_{rs}(\lambda)$ values remained high in the red spectra for high TSM concentrated waters, producing the broad maximum peak shown. This increase in $R_{rs}(\lambda)$ masks the Chl*a* induced variations in the green and red when TSM concentrations are high.

3.4.3 Algorithm development and calibration

Regional Chla algorithm

The regional $R_{rs}(\lambda)$ data set was used to establish a relation between *in situ* Chl*a* concentration and the four algorithms from Table 3-1, for both MODIS and Sentinel-3. A regression-based approach was adopted to derive a relation between $R_{rs}(\lambda)$ and Chl*a* using raw or log transformed data, when data ranged several orders of magnitude (O'Reilly et al., 1998). The regression analysis included applying a non-linear equation to establish a functional form that produced the highest correlation (R^2 value), (Cannizzaro & Carder, 2006; Nagamani et al., 2008; O'Reilly et al., 1998), which in most cases resulted in a second or third order polynomial (Table 3-3).

The results revealed the OC models (OC3M and OC3S3) were poorly related to Chl*a* (R^2 ~ 0.13) with substantial dispersion across the entire concentration range. The 2-

band approach also yielded poor results, which were statistically insignificant (R^2 ~ 0.07). A significant relationship was found for the FLH algorithm against Chl*a* (R^2 ~ 0.39; $p < 0.001$). Multiplication of the FLH algorithm by the 2-band ratio, $R_{rs}(678)/R_{rs}(667)$ for MODIS and $R_{rs}(681)/R_{rs}(674)$ for Sentinel-3, slightly improved this relation (R^2 ~ 0.42; $p < 0.001$).

Table 3-3 Summary of the empirical models developed using regional data (n = 142) to form regression equations (X) with in situ Chl*a*. The resulting best fit non-linear equation produces the derived Chl*a* equation shown.

Empirical Algorithm	**Algorithm Form**	**Derived Chl*a* Equation (regression)**	R^2	**p-value**
$OC3M$ MODIS	$X = \log_{10}\left[\frac{max\{R_{rs}(443,488)\}}{R_{rs}(547)}\right]$	$Chla = 10^{(-0.109-0.818X+2.50X^2)}$	0.13	<0.001
$OC3S3$ Sentinel-3	$X = \log_{10}\left[\frac{max\{R_{rs}(443,490)\}}{R_{rs}(560)}\right]$	$Chla = 10^{(-0.120-0.753X+2.09X^2)}$	0.16	<0.001
R_{667}/R_{547} MODIS	$X = \log_{10}\left[\frac{R_{rs}(667)}{R_{rs}(547)}\right]$	$Chla = 0.066 - 9.44X - 11.0X^2$	0.07	>0.001
R_{665}/R_{560} Sentinel-3	$X = \log_{10}\left[\frac{R_{rs}(665)}{R_{rs}(560)}\right]$	$Chla = -0.374 - 9.73X - 10.3X^2$	0.06	>0.01
FLH MODIS	$X = \log_{10}[R_{rs}(678) - 0.860R_{rs}(667) - 0.140R_{rs}(746)]$	$Chla = 10^{(-7.70-4.99X-0.782X^2)}$	0.39	<0.001
FLH Sentinel-3	$X = \log_{10}[R_{rs}(681) - 0.636R_{rs}(665) - 0.364R_{rs}(709)]$	$Chla = 10^{(-8.36-5.49X-0.874X^2)}$	0.37	<0.001
$ModFLH$ MODIS	$X = FLH \times \frac{R_{rs}(678)}{R_{rs}(667)}$	$Chla = -0.682 + 1.1E04X - 9.5E06X^2 - 2.0E09X^3$	**0.42**	<0.001
$ModFLH$ Sentinel-3	$X = FLH \times \frac{R_{rs}(681)}{R_{rs}(674)}$	$Chla = -0.496 + 8218X - 4.2E06X^2$	**0.40**	<0.001

Class specific Chla algorithm

Relationships between *in situ* Chl*a* and the four algorithms were established for the estuarine and oceanic class data. Table 3-4 summarizes the algorithms, which were derived by fitting a non-linear equation and reporting the functional form with the highest correlation, similar to the regional regression (Cannizzaro & Carder, 2006; Nagamani et al., 2008; O'Reilly et al., 1998). In general, the results showed improved results for the class-based algorithms defined above. For the estuarine class, Chl*a* data were found to be significantly correlated ($R^2 \sim 0.62$, $p < 0.001$) to the 2-band ratio algorithm for both MODIS and Sentinel-3 versions (Figure 3-4a). Lower correlations were defined with the FLH and the ModFLH algorithms (not shown). For the oceanic class, the ModFLH algorithm exhibited the highest correlation ($R^2 > 0.70$, $p < 0.001$) (Figure 3-4b) for both MODIS and Sentinel-3 derived versions. The FLH algorithm also showed a marked improvement ($R^2 > 0.61$; $p < 0.001$) for the oceanic class. The OC algorithms (OC3M and OC3S3) showed a slight improvement in correlation when compared with the regional versions, although not as significant ($p > 0.01$) as the results of the other class-specific algorithms.

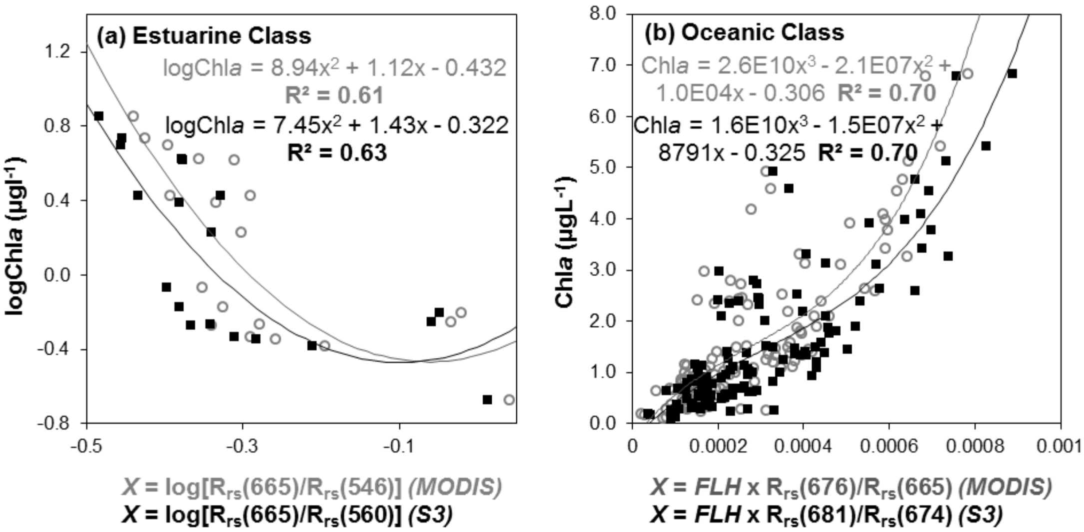

Figure 3-4 Class-specific reflectance-based algorithm results for **(a)** estuarine class waters and **(b)** oceanic class waters. MODIS values are shown in gray, Sentinel-3 values in black. Note the shown relationships are the most significant relationships and do not include all algorithms in the analysis.

Table 3-4 Summary of the empirical algorithms developed using class specific data sets for estuarine (n = 19) and oceanic class (n = 124) data to form the regression equation (X) with *in situ* Chl*a*. The resulting non-linear best fit equation produces the Chla equation shown.

Empirical Algorithm	**Input**	**Algorithm Form**	**Derived Chl*a* Equation (regression)**	***R*²**	**p-value**
$OC3M$ MODIS	Estuarine	$X = \log_{10}\left[\frac{max\{R_{rs}(443,488)\}}{R_{rs}(547)}\right]$	$Chla = -3.84 - 101X - 349X^2$	0.25	>0.01
	Oceanic		$Chla = 10^{(-0.116-0.746X+3.48X^2)}$	0.19	<0.001
$OC3S3$ Sentinel-3	Estuarine	$X = \log_{10}\left[\frac{max\{R_{rs}(443,490)\}}{R_{rs}(560)}\right]$	$Chla = -5.77 - 83.4X - 210X^2$	0.10	>0.1
	Oceanic		$Chla = 10^{(-0.123-0.701X+2.61X^2)}$	0.21	<0.001
R_{667}/R_{547} MODIS	Estuarine	$X = \log_{10}\left[\frac{R_{rs}(667)}{R_{rs}(547)}\right]$	$Chla = 10^{(-0.432+1.12X+8.94X^2)}$	**0.61**	<0.001
	Oceanic		$Chla = -0.209 - 9.53X - 10.9X^2$	0.05	>0.01
R_{665}/R_{560} Sentinel-3	Estuarine	$X = \log_{10}\left[\frac{R_{rs}(665)}{R_{rs}(560)}\right]$	$Chla = 10^{(-0.322+1.43X+7.45X^2)}$	**0.63**	<0.001
	Oceanic		$Chla = -0.616 - 10.0X - 10.3X^2$	0.03	>0.1
FLH MODIS	Estuarine	$X = \log_{10}[R_{rs}(678) - 0.860R_{rs}(667) - 0.140R_{rs}(746)]$	$Chla = 10^{(-10.0-5.61X-0.761X^2)}$	0.30	>0.05
	Oceanic		$Chla = 10^{(11.3-4.89X-0.493X^2)}$	0.62	<0.001
FLH Sentinel-3	Estuarine	$X = \log_{10}[R_{rs}(681) - 0.636R_{rs}(665) - 0.364R_{rs}(709)]$	$Chla = 10^{(-23.0-13.9X-2.08X^2)}$	0.28	>0.01
	Oceanic		$Chla = 10^{(13.7-6.29X-0.692X^2)}$	0.61	<0.001
$(FLH \times R_{678}/R_{667})$ MODIS	Estuarine	$X = \log_{10}\left[FLH \times \frac{R_{rs}(678)}{R_{rs}(667)}\right]$	$Chla = 10^{(-15.5-9.30X-1.37X^2)}$	0.27	>0.05
	Oceanic	$X = FLH \times \frac{R_{rs}(678)}{R_{rs}(667)}$	$Chla = -0.306 + 1.0E04X - 2.1E07X^2 + 2.6E10X^3$	**0.70**	<0.001
$(FLH \times R_{681}/R_{674})$ Sentinel-3	Estuarine	$X = \log_{10}\left[FLH \times \frac{R_{rs}(681)}{R_{rs}(674)}\right]$	$Chla = 10^{(-30.1-18.7X-2.87X^2)}$	0.27	>0.01
	Oceanic	$X = FLH \times \frac{R_{rs}(681)}{R_{rs}(674)}$	$Chla = -0.325 + 8791X - 1.5E07X^2 + 1.6E10X^3$	**0.70**	<0.001

3.4.4 Algorithm evaluation using *in situ* data

Regional Chla algorithm

Statistical analysis comparing algorithm-retrieved and *in situ* Chl*a* concentrations was used to evaluate the performance of the regional empirical algorithms (Table 3-3). For the four algorithms, the relationship between algorithm-retrieved Chl$a$ concentrations and measured *in situ* Chl$a$ concentrations and associated TSM data and $a_{cdom}(443)$ data are shown in Figures 3-5 and 3-6, respectively, and the error distribution plots in Figure 3-7.

As expected, the accuracy of the tested models using the regional data set is poor. The slope and intercept data indicated a poor comparison with *in situ* data (low slopes and intercepts away from 0). Substantial data scatter occurred for all four models tested with higher errors related to increases in both TSM and $a_{cdom}(443)$ magnitudes (Figure 3-5 and 3-6, respectively). This is related to a general overestimation of low Chl$a$ values and underestimation of high Chl$a$ concentrations, in particular for the OC (OC3M and OC3S3) (R^2 ~ 0.19; *RMSE* ~ 0.37; slope (S) ~ 0.13; intercept (I) ~ 0.96 µg l^{-1}) and 2-band ratio (R^2 ~ 0.07; *RMSE* ~ 0.41; S ~ 0.07; I ~ 1.53 µg l^{-1}) algorithms (Figure 3-5). Error plots are also strongly skewed for these models and mean errors are high (Figure 3-7a,b, Table 3-5). The FLH algorithm showed an improvement over the OC and 2-Band ratio algorithms with a stronger correlation to *in situ* Chl$a$ (R^2 ~ 0.37; *RMSE* ~ 0.31; S ~ 0.19; I ~ 0.93 µg l^{-1}) and lower bias (-0.001 for MODIS and 0.093 for Sentinel-3) (Figure 3-5c,g, respectively). This relation is slightly improved with the modified FLH algorithm for both MODIS (R^2 = 0.42; *RMSE* = 0.29; S = 0.40; I = 1.00 µg l^{-1}) and Sentinel-3 (R^2 = 0.40; *RMSE* = 0.30; S = 0.38; I = 1.05 µg l^{-1}), which is accounting for some of the outlying data seen in the FLH model, resulting in the lowest bias reported (0.066 for MODIS, 0.082 for Sentinel-3) (Table 3-5).

Table 3-5 Statistical results of the empirical algorithms using the regional data.

Empirical Algorithm	**Input Data**	***N***	***R***	***RMSE***	**p-value**	**Bias**	**Slope**	**Intercept**
$OC3M$ MODIS	Regional	145	0.19	0.37	<0.001	0.001	0.13	0.96
$OC3S3$ Sentinel-3	Regional	145	0.22	0.39	<0.001	0.132	0.22	1.28
R_{667}/R_{547} MODIS	Regional	145	0.07	0.41	0.001	0.146	0.07	1.53
R_{665}/R_{560} Sentinel-3	Regional	145	0.06	0.42	0.003	0.150	0.05	1.56
FLH MODIS	Regional	145	0.37	0.31	<0.001	-0.001	0.19	0.93
FLH Sentinel-3	Regional	145	0.37	0.32	<0.001	0.093	0.35	1.11
$(FLH \times R_{678}/R_{667})$ MODIS	Regional	145	**0.42**	0.29	<0.001	0.066	0.40	1.00
$(FLH \times R_{681}/R_{674})$ Sentinel-3	Regional	145	**0.40**	0.30	<0.001	0.082	0.38	1.05

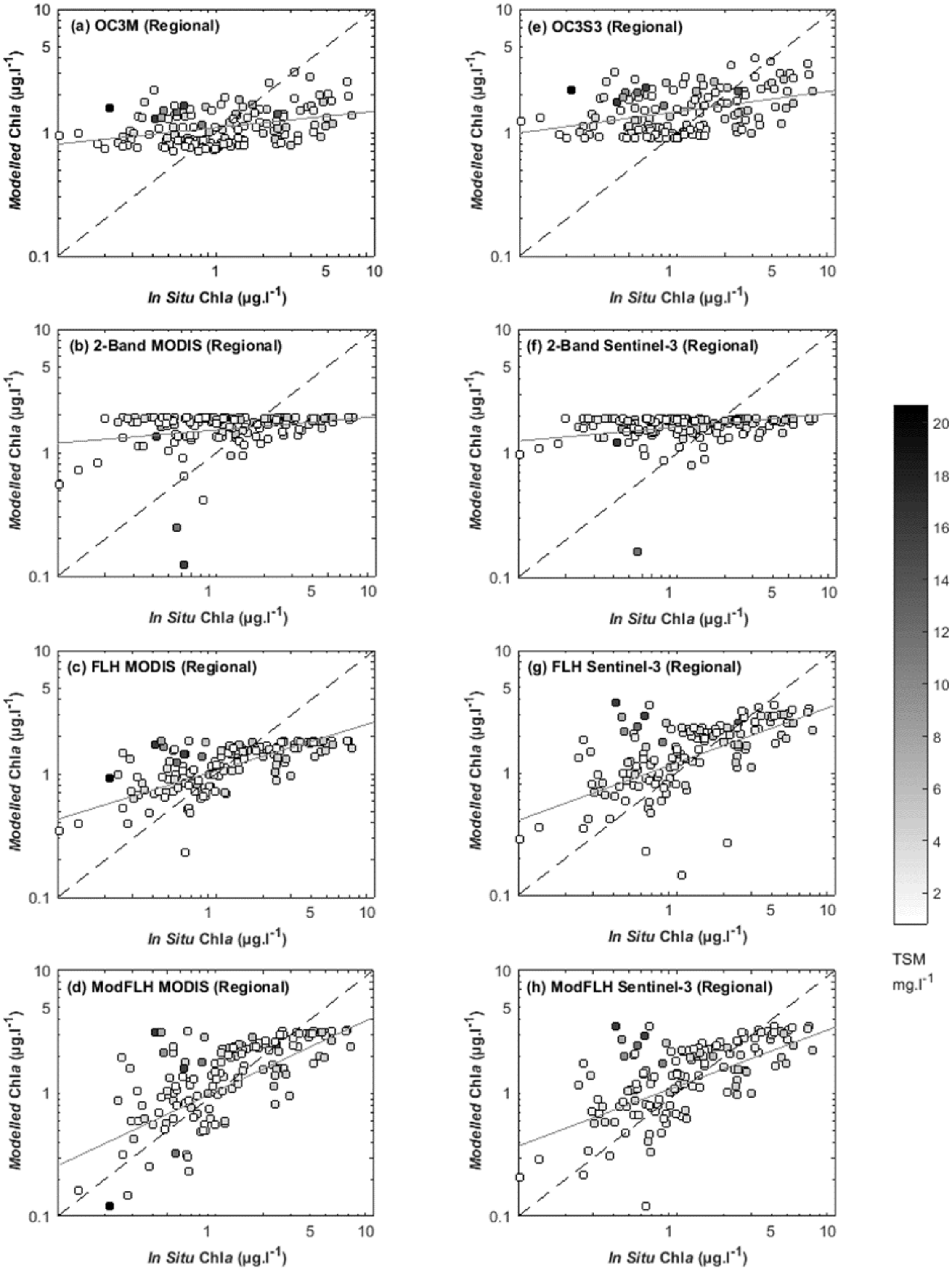

Figure 3-5 Linear regression between measured in situ Chl*a* values and modelled Chl*a* values that were derived with the regional data set using the four algorithms for **(a-d)** MODIS and **(e-h)** Sentinel-3. TSM concentrations for each point are shown as proportional gray symbols.

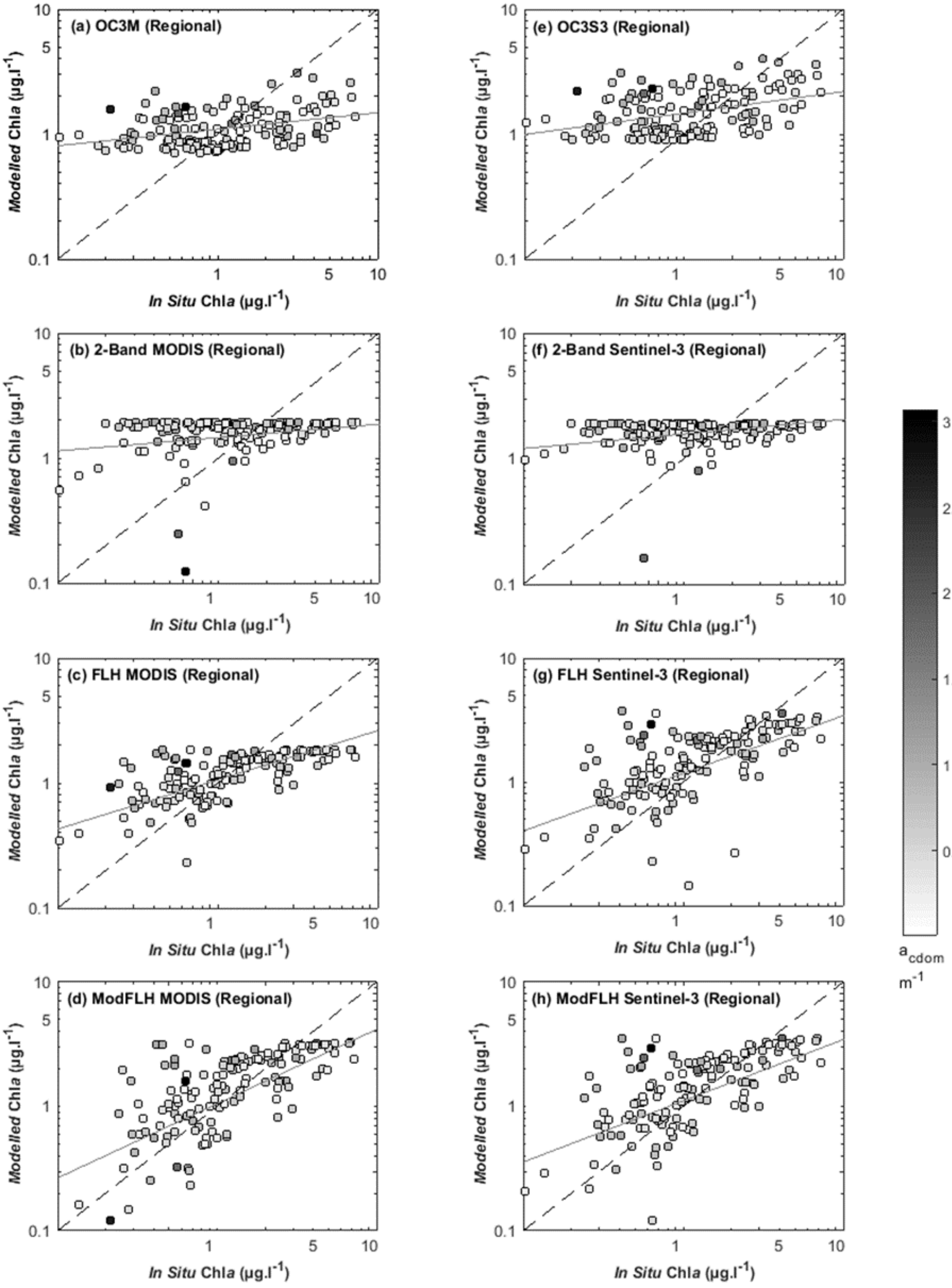

Figure 3-6 Linear regression between measured in situ Chl*a* values and modelled Chl*a* values that were derived with the regional data set using the four algorithms for **(a-d)** MODIS and **(e-h)** Sentinel-3. $a_{cdom}(443)$ coefficients for each point are shown as proportional symbols.

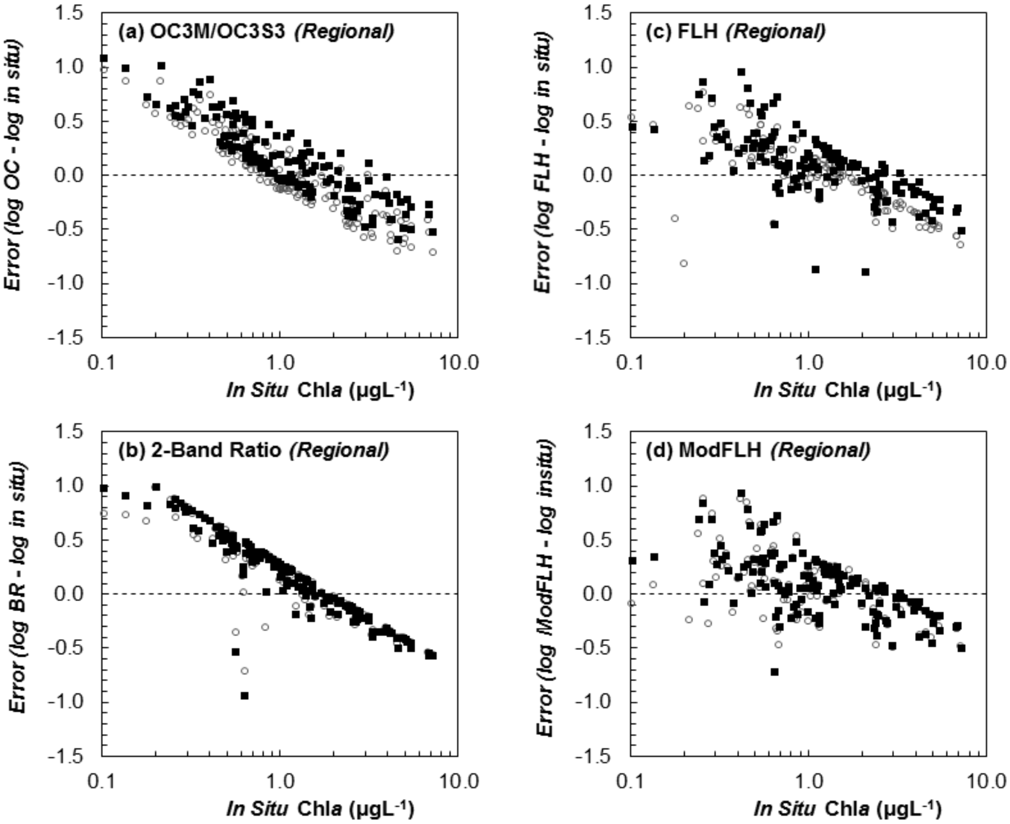

Figure 3-7 Error plots showing the difference between modelled Chl*a* and in situ Chl*a* for **(a)** OC3M/OC3S3, **(b)** 2-band ratio, **(c)** FLH and **(d)** ModFLH regional algorithms.

Class specific Chla algorithm

Using class specific data the algorithms were re-parameterized to produce estuarine and oceanic class specific algorithms (Table 3-4). Figure 3-8a-d shows the comparison between $R_{rs}(\lambda)$ retrieved Chl*a* concentrations and *in situ* Chl*a* for the estuarine class data, with corresponding error distributions (Figure 3-8e-h). In nearly all cases, higher correlations were observed compared to the equivalent regional algorithms. For the estuarine class, the 2-band ratio algorithm showed the best statistical results for MODIS using R_{547}^{667} (R^2 = 0.72; *RMSE* = 0.30; S = 0.66; I = 0.37 μg l^{-1}) and for Sentinel-3 using R_{560}^{665} (R^2 = 0.71; *RMSE* = 0.33; S = 0.54; I = 0.55 μg l^{-1}) (Figure 3-8b). These *RMSE* values were reduced (28%) from the regional 2-band algorithms (Table 3-6). The regression slopes also showed a marked improvement over the regional algorithms, consistent with the reduced intercepts. Errors for this algorithm were randomly and normally distributed with the mean error, or bias, below 0.49 for both the MODIS and Sentinel-3 versions (Figure 3-8f).

The results of the 2-band ratio algorithm, however, were not statistically significant ($p > 0.01$) for the oceanic class (Figure 3-9b). Instead, the ModFLH algorithm showed the best statistical results for this water class, for both MODIS and Sentinel-3 (R^2 ~ 0.70; *RMSE* ~ 0.25; S ~ 0.70; I ~ 0.49 µg l^{-1}) (Figure 3-9d). *RMSE* values were approximately 15% lower compared to the regional parameterizations, corresponding to the low reported errors (Figure 3-9h). The FLH algorithm also performed well for the oceanic class (R^2 ~ 0.67; *RMSE* ~ 0.23; S ~ 0.62; I ~ 0.43), although not as strong as the modified FLH algorithm. Both the FLH and ModFLH models showed poor performance with the estuarine class data (R^2 ~ 0.16; *RMSE* ~ 0.41; S ~ 0.09; I ~ 1.23 µg l^{-1}) and the OC3M/OC3S3 algorithm only showed a slight improvement when parameterized for class specific data. Again, a systematic overestimation in the low Chl*a* range and underestimation for higher Chl*a* values was observed (Figure 3-8a, 3-9a).

Table 3-6 Statistical results of the empirical algorithms using the class specific data.

Empirical Algorithm	**Input Data**	**N**	***R*²**	***RMSE***	**p-value**	**bias**	**Slope**	**Intercept**
$OC3M$ MODIS	Estuarine Class	19	0.25	0.48	0.03	0.147	0.25	1.61
	Oceanic Class	125	0.27	0.37	<0.001	0.121	0.27	1.15
$OC3S3$ Sentinel-3	Estuarine Class	22	0.08	0.52	0.20	0.177	0.08	1.87
	Oceanic Class	122	0.30	0.34	<0.001	0.000	0.24	0.81
R_{667}/R_{547} MODIS	Estuarine Class	19	**0.72**	0.30	<0.001	0.000	0.66	0.37
	Oceanic Class	125	0.05	0.40	0.01	0.146	0.05	1.49
R_{665}/R_{560} Sentinel-3	Estuarine Class	22	**0.71**	0.33	<0.001	0.000	0.54	0.55
	Oceanic Class	122	0.03	0.41	0.05	0.153	0.03	1.51
FLH MODIS	Estuarine Class	19	0.21	0.40	0.05	0.000	0.12	1.20
	Oceanic Class	125	0.67	0.23	<0.001	0.000	0.62	0.43
FLH Sentinel-3	Estuarine Class	22	0.13	0.42	0.10	0.000	0.08	1.24
	Oceanic Class	122	0.66	0.25	<0.001	0.066	0.66	0.53
$(FLH \times R_{678}/R_{667})$ MODIS	Estuarine Class	19	0.16	0.41	0.09	0.000	0.09	1.23
	Oceanic Class	125	**0.70**	0.25	<0.001	0.065	0.70	0.49
$(FLH \times R_{681}/R_{674})$ Sentinel-3	Estuarine Class	22	0.12	0.42	0.10	0.000	0.08	1.23
	Oceanic Class	122	**0.70**	0.26	<0.001	0.056	0.70	0.47

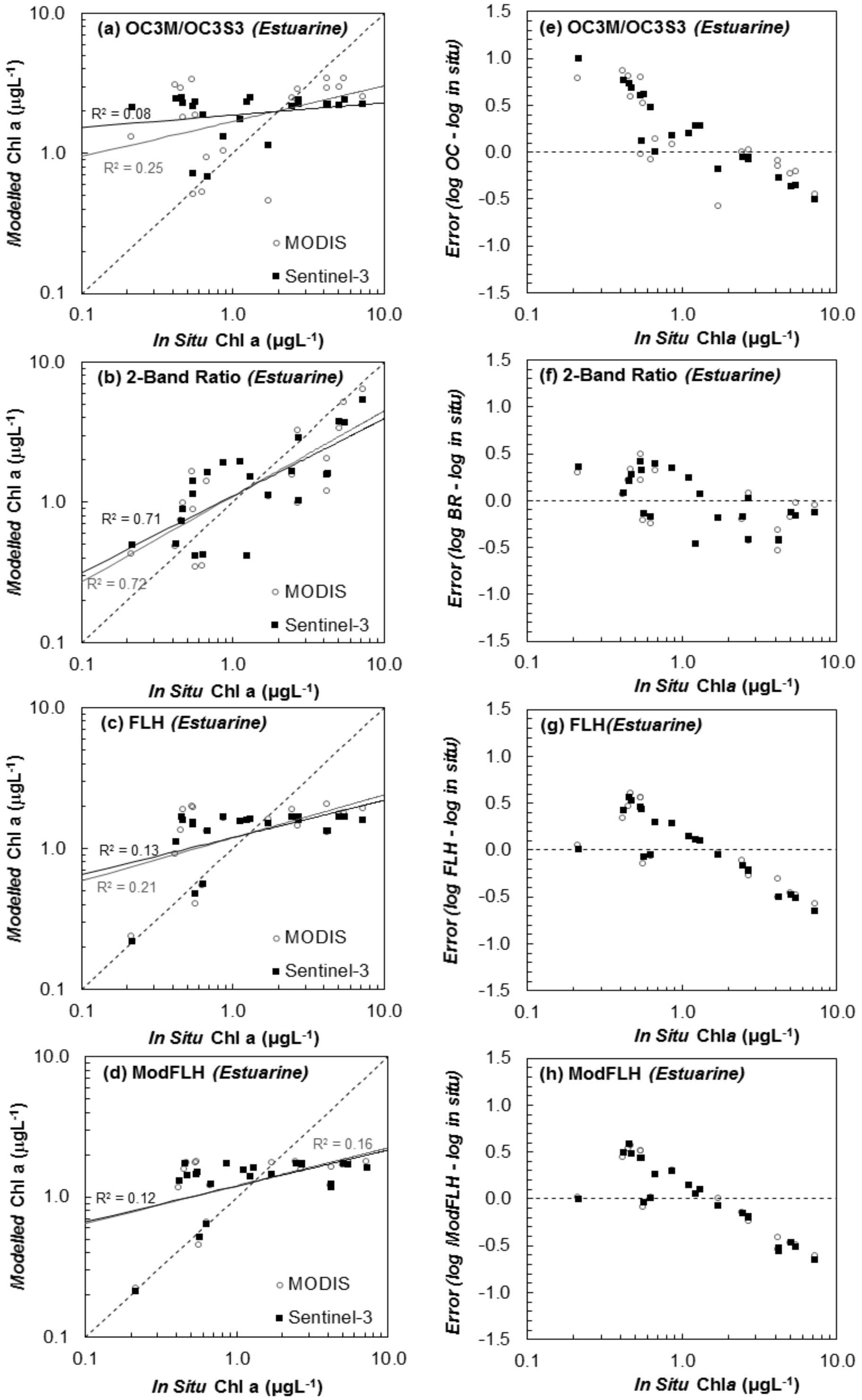

Figure 3-8 Linear regression between measured *in situ* Chl*a* values and modelled Chl*a* values that were derived with the *estuarine class* data set using **(a)** OC3M/OC3S3, **(b)** 2-Band Ratio, **(c)** FLH and **(d)** the Modified FLH algorithms. Corresponding error plots are shown for each algorithm **(e-h)**. MODIS results are shown as grey circles and Sentinel-3 as black squares.

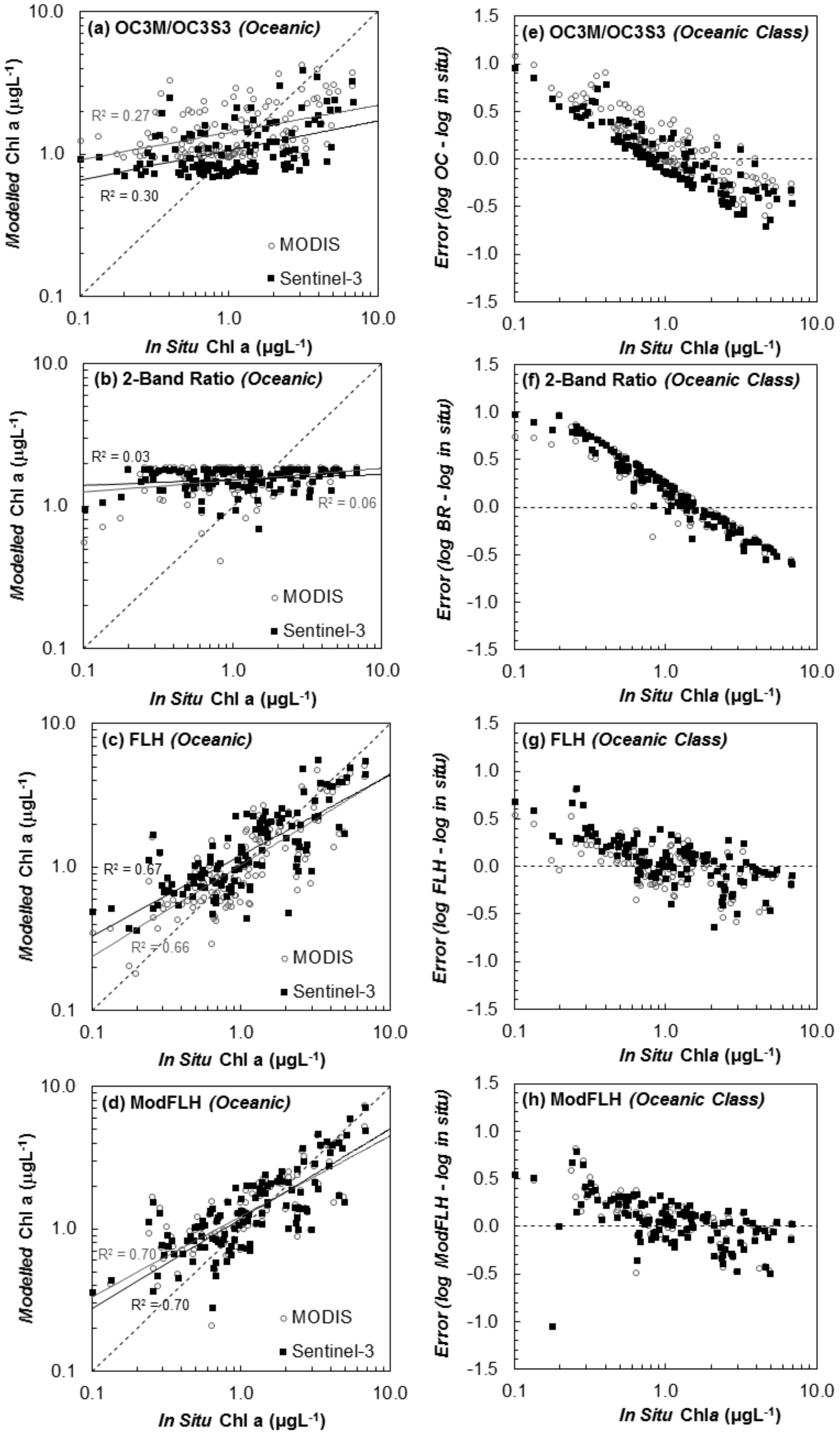

Figure 3-9 Linear regression between measured *in situ* Chl*a* values and modelled Chl*a* values that were derived with the *oceanic class* data set using **(a)** OC3M/OC3S3, **(b)** 2-Band Ratio, **(c)** FLH and **(d)** the Modified FLH algorithms. Corresponding error plots are shown for each algorithm **(e-h)**. MODIS results are shown as grey circles and Sentinel-3 as black squares.

3.5 Discussion

As a first step on improving the ocean colour satellite retrievals of Chl*a* for the Salish Sea, this research focused on developing and testing standard ocean colour reflectance-based algorithms with adapted coefficients and other reflectance-based algorithms based on regional and class-specific datasets. Global ocean colour Chl*a* algorithms, such as empirical algorithms (OCX algorithms, Gordon & Morel, 1983; O'Reilly, 2000) or semi-analytical algorithms (GSM algorithm, Maritorena et al., 2002; the QAA algorithm, Lee & Carder, 2002), are typically developed from a global dataset, and as such they are often less accurate in coastal regions due to the regional-specific variability of in-water optically active constituents (Harding et al., 2005; Le et al., 2013a; Mélin & Vantrepotte, 2015; Moses et al., 2009a; Mustapha et al., 2012). This is particularly the case in the Salish Sea, which experiences a high influx of riverine sediment with associated suspended particulate matter and allochthonous CDOM, coupled with a highly variable but productive ecosystem (Johannessen et al., 2003; Komick et al., 2009; Loos & Costa, 2010; Masson & Perry, 2013). To overcome these challenges, we first tested the accuracy of four empirical algorithms with coefficients adapted to localized conditions, as represented by the regional data set, and then modified to sub-regionalized conditions based on an optical water classification. Optical waters types were segregated into two classes, estuarine and oceanic waters, based on the dominating spectral properties as a simplification of the four separate optical classes defined in chapter 2. This parameterization of the models allowed the coefficients to be adjusted to better represent the regional IOP variability, which has been successfully demonstrated in other coastal studies (Feng et al., 2005; Lubac & Loisel, 2007; Moore et al., 2009; Mustapha et al., 2012). The results demonstrate the advantage of optimized reflectance based empirical models for Chl*a* retrievals in the coastal waters off the west coast of Canada.

The results of using the standard OC3M and OC3S3 adapted algorithms (Table 3-1) with the regional Salish Sea data set showed a consistent deviation with overestimations for lower Chl*a* concentrations and underestimations for higher Chl*a* (Figure 3-5a,e). This is similar to previous studies in the region (Komick et al, 2009) and other Case 2 coastal sites, for instance, in the Gulf of Finland and Chesapeake Bay (Vazyulya et al., 2014; Werdell et al., 2009, respectively). Although the coefficients were parameterized to local data in the Salish Sea, the OC3M/OC3S3 and 2-band algorithms performed the poorest among the evaluated algorithms, showing high uncertainty (*RMSE* ~ 0.37) for both Sentinel-3 and MODIS versions, with the 2-band algorithm demonstrating the greatest bias (*RMSE* ~ 0.41) (Table 3-4). The large inaccuracies of these algorithms are a result of the variability in the concentrations of optical water constituents in the Salish Sea; i.e., waters under strong influence of TSM and or CDOM and disparate concentrations of Chl*a*. Specifically, TSM concentrations seem to play a role on these algorithm accuracies, with a general trend of increasing error with increasing inorganic TSM observed. For the 2-band algorithm, which uses the red to green bands, the high TSM concentrations of inorganic nature (>73% of total TSM) induced error produces increased reflectances through scattering and backscattering effects (Yacobi et al., 2011), as opposed to increases in Chl*a* absorption being maximal as expected in the red spectra (Morel & Prieur, 1977). Thus when TSM concentrations are high the increased reflectance in the red will underestimate Chl*a* values by masking the Chl*a* absorption signal. During the spring in the central Salish Sea, a significant increase in scattering and backscattering was observed ($b_p(650) = 2.783 \pm 2.047$m^{-1}, or 80% of total attenuation, and $b_{bp}(650) = 0.031 \pm 0.023$ m^{-1}), corresponding to high average TSM concentrations (4.48 ± 4.55 mg l^{-1}), compared to oceanic waters in the summer when magnitudes were reduced ($b_p(650) = 0.844 \pm 0.733$ m^{-1}; $b_{bp}(650) = 0.019 \pm 0.021$ m^{-1}; TSM avg = 3.03 ± 1.16 mg l^{-1}). This large gradient is consistent with the high errors associated with the regional 2-band algorithm, especially when parameterized based on assumptions of waters with similar optical characteristics, when TSM effects are highly variable both spatially and temporally.

To further understand the impact of particle composition associated with these turbid waters, the backscattering ratio, b_{bp}/b_p, was analyzed (Chapter 2). Although limited to n = 34 samples, the data showed relatively high backscattering ratios (avg = 0.020), indicating a dominance of inorganic particles in measured samples (Sullivan et al., 2005). For a limited number of samples (n = 4), relative lower backscattering ratios (<0.010) were measured, indicating a shift to larger organic phytoplankton particles dominating the particle assemblage (Sullivan et al., 2005). More data would be required to expand this further, including acquiring data under fall conditions, which was missing due to instrument failure. Additional information on particle size distribution and refractive index, both dependent on particle assemblage, would also be important since these properties can affect mass-specific absorption and backscattering coefficients, producing large variations in reflectance (Twardowski et al., 2001; Wozniak & Stramski, 2004). Adding this information could prove useful for tuning the OC or 2-band algorithms within the estuarine waters in order to achieve higher accuracies.

Additional errors related to the regional algorithm performance show evidence attributed to strong CDOM absorption in the short blue and green wavelengths, which the OC3M model, for example, depends on (Komick et al., 2009; Le et al., 2013a; O'Reilly, 2000; Sathyendranath et al., 2001). As shown in Figure 3-6, $a_{cdom}(443)$ demonstrated a similar pattern as TSM, with high errors in the regressions between modelled and *in situ* Chl*a* typically related to increasing CDOM absorption. The results of Chapter 2 show the dominant source of CDOM is allochthonous from the Fraser River, which is associated with TSM concentrations, and therefore does not always co-vary with Chl*a* (Loos & Costa, 2010). Consequently, the high mean CDOM absorption coefficient in this study ($a_{\mathrm{cdom}}(443) = 0.525\ \mathrm{m}^{-1} \pm 0.409\ \mathrm{m}^{-1}$), which is slightly higher than previously measured in the region ($a_{\mathrm{cdom}}(443) = 0.31 \pm 0.38\ \mathrm{m}^{-1}$, Komick et al, 2009), explains the inaccuracies of the OC3M algorithm in these conditions, as it has been demonstrated in Komick et al. (2009) and other studies in turbid waters (Chen & Quan, 2013; Mustapha et al., 2012). Thus, these findings suggest that a regional two band algorithm of the form OC3M or red to green ratio is not able overcome the effects of CDOM and or TSM and is therefore not accurate for the Salish Sea.

Parameterizing the OC3M/OC3S3 algorithm to class specific data had minimal effect on algorithm performance. A slight improvement for the oceanic class (R^2 ~ 0.27; *RMSE* ~ 0.37; S ~ 0.27; I ~ 1.15 $\mu\mathrm{g\ l}^{-1}$) was observed (Figure 3-9a), presumably a result of the exclusion of waters with high TSM, consistent with Komick et al. (2009) and Pan et al. (2008). For the present data set, the high TSM concentrated waters in the estuarine class showed no significant correlation between OC3M and *in situ* Chl*a*, particularly for lower concentrations (< 1 $\mu\mathrm{g\ l}^{-1}$), and in fact resulted in the highest measured error

(>1.000) among all the tested models (Figure 3-8a,e). Parameterizing the 2-band algorithm however, to class specific data, resulted in more accurate retrievals, especially for the estuarine class data (Figure 3-8b). Data are limited in this class to less than 22 samples but the results showed a strong agreement to *in situ* Chl*a* values (R^2 = 0.72 for MODIS and 0.71 for Sentinel-3; $p < 0.001$; *RMSE* ~ 0.30; S ~ 0.66; I ~ 0.37 µg l^{-1}) with errors well below 0.49 that were randomly and normally distributed (Figure 3-8f). These results suggest a 2-band algorithm, focused on red and green bands, is suitable for Chl*a* estimations in the turbid waters of the Salish Sea, which is comparable to other studies in turbid coastal waters using a similar approach (R^2 = 0.69 – 0.74; Mustapha et al., 2012; Tilstone et al., 2011; Vazyulya et al., 2014).

As an alternative approach, and to minimize the spectral interference of TSM, the Chl*a* fluorescence maximum near 685 nm was used in the FLH algorithm to retrieve Chl*a* (Gower et al., 1999, 2004). Using regional data the FLH algorithm was parameterized with coefficients to align with the localized conditions to improve results (R^2 ~ 0.37; *RMSE* ~ 0.31; S ~ 0.19; I < 0.93 µg l^{-1}) compared to OC and 2-band algorithms (R^2 ~ 0.19; *RMSE* ~ 0.37; S ~ 0.13; I ~ 0.96 µg l^{-1} and R^2 ~ 0.07; *RMSE* ~ 0.41; S ~ 0.07; I ~ 1.53 µg l^{-1}, respectively). A performance difference between the results of the MODIS and Sentienl-3 versions was observed, likely attributable to the sensors have differing band specifications, which would alter the location to define the baseline calculation in the FLH algorithm. The linear regressions between *in situ* Chl*a* and those modeled from FLH again show a systematic overestimation of Chl*a* below 2 µg l^{-1} and underestimation for higher Chl*a* concentrations, linked to increasing TSM (Figure 3-5c,g) and increased allochthonous CDOM absorption (Figure 3-6c,g). This can be attributed to particulate scattering and backscattering increasing background radiance levels, causing a red-shift which can mask the fluorescence signal and cause underestimations for high Chl$a$ concentrations and overestimations for low values (Gower et al., 1999; McKee et al., 2007; Zhao et al., 2015). Additionally, a decrease in photosynthetically available radiation (PAR), attenuated by CDOM and non-algal particulate (NAP) absorption, in combination to the NAP backscattering, is likely causing the underestimation in the fluorescence peak and thus the underestimates in the high Chl$a$ concentrations observed (Gilerson et al., 2007; Ioannou et al., 2009; McKee et al., 2007).

Parameterizing the FLH algorithm to class specific data isolated the above issues to some degree. As expected, oceanic class data showed stronger agreement in the FLH model (R^2 ~ 0.67; *RMSE* ~ 0.23; S ~ 0.62; I ~ 0.43 µg l^{-1}), due to reduced TSM induced errors (Figure 3-9c). Estuarine class data, however, was not statistically significant and a systematic overestimation of low and underestimation of high Chl$a$ concentrations was still prominent (Figure 3-8c), compared to the regional FLH algorithm. This was expected given the increased reflectances associated with particulate backscattering and CDOM and NAP absorption in this class. Errors related to CDOM and NAP absorption were reduced in the oceanic class data: however, a significant range of CDOM was still observed ($a_{cdom}(443)$ = 0.007 – 1.551 m^{-1}). For these waters, CDOM absorption slopes (Table 3-2) were lower on average (S_{cdom} avg = 0.018 nm^{-1}), indicating autochthonous CDOM sources are more prevalent and typically expected to co-vary with Chl$a$ (Carder et al., 1989; Helms et al., 2008; Twardowski et al., 2004). However, within this class, 34% of the samples showed S_{cdom} > 0.020, indicating allochthonous CDOM presence, which can reduce the fluorescence signal due to increased attenuation, and therefore produce unreliable FLH estimates (Gilerson et al., 2008)(Figure 3-9d).

The inaccuracies associated with the standard FLH algorithm are largely improved by applying an optical classification scheme, but Chl*a* underestimations still need to be addressed. To correct for this, the modified FLH algorithm utilizes a correction factor to improve Chl*a* concentration estimates. The ratio between the Chl*a* fluorescence band near 678 nm or 681 nm to the maximum Chl*a* absorption band near 665 nm was applied to FLH in the form of R_{667}^{678} and R_{674}^{681} for MODIS and Sentinel-3, respectively. The premise is that both R_{667}^{678} and R_{674}^{681} increase with increasing Chl*a* concentrations due to the generally expected increase in Chl*a* fluorescence (numerator) and increase in Chl*a* maximum absorption near 665nm (minimum in R_{rs}). In this way, shifts in the fluorescence maximum, which can be caused by other constituents, especially inorganics and therefore not fully represented by just the contribution of Chl*a* fluorescence can be accounted for (Gilerson et al., 2007; Le et al., 2009; Schalles et al., 2002). As shown in Figure 3-3, this shift was significant in the present data set, particularly in the estuarine class spectra, where the fluorescence peak shifts nearly 20 nm between some spectra.

In practice, the ModFLH algorithm demonstrated improved results for the regional data set with parameterization. Comparing the retrieved Chl*a* values to *in situ* Chl*a* concentrations showed the highest correlation (R^2 ~ 0.42; *RMSE* ~ 0.29; S ~ 0.40; I ~ 1.00 µg l^{-1}) among the four tested algorithms (Table 3-5). Parameterizing this algorithm to the estuarine class data, as expected, decreased the accuracy (R^2 ~ 0.16; *RMSE* ~ 0.42; S ~ 0.08; I ~ 1.23 µg l^{-1}), compared to the regional version, with strong overestimations in the low Chl*a* range and underestimations for higher values. Again, increased TSM in this class, and related particulate scattering and backscattering, are most likely responsible for the algorithms inability to resolve the fluorescence peak as reflectance values are increased in this class, including near 665nm where the ModFLH model depends on, resulting in the large underestimations of Chl*a* observed. The additional band availability for Sentinel-3 (B9 near 674 nm) was used in the Sentinel-3 version of the ModFLH algorithm in an attempt to avoid this interference near 665 nm, however similar inaccuracies were still observed. For the oceanic class data the results were significantly improved. When comparing the modelled Chl*a* to *in situ* Chl*a* a robust correlation (R^2 ~ 0.70; *RMSE* ~ 0.25) was found for both MODIS and Sentinel-3, and the data showed a good fit (S ~ 0.70, I ~ 0.49 µg l^{-1}) (Figure 3-9d). This was a strong improvement over the regional ModFLH algorithm (Figure 3-5d), again a result of minimizing high TSM influences and the ability to parameterize the algorithm to data suitable for the defined optical water class, in this case the oceanic class. Future work would need to expand the present data set to fine-tune the coefficients further. Ioannou et al. (2009) have developed another modified FLH algorithm called the Ratio Fluorescence Height (RFH) in which a similar band ratio to that in our ModFLH algorithm is used and correlated to the blue green ratio, usually used as a proxy for Chl*a* in many ocean colour algorithms, such as the OC3M (O'Reilly et al., 1998). Future studies in the Salish Sea should look into this approach as a potential extension of our ModFLH algorithm for improving Chl*a* accuracies even further.

3.6 Conclusion

The goal of this research was to improve ocean colour Chl$a$ retrievals in the Case 2 coastal waters of the Salish Sea by calibrating and validating empirical algorithms specifically for this region. Biophysical and *in situ* hyperspectral $R_{rs}(\lambda)$ measurements, collected under spring, summer, and fall conditions for 2012-2013 (145 stations), provided training data under a wide range of spatial and temporal conditions found in this region. Corresponding reflectance values were modeled to MODIS and Sentinel-3 bands and used to develop refined coefficients for the OC3M, 2-band ratio, FLH, and modified FLH algorithms.

Results showed all four algorithms were poorly correlated to *in situ* Chl$a$ for the regional data set. Consistent overestimations of modeled Chl$a$ values for low concentrations and underestimations for higher values were reported throughout all four algorithms. The modified FLH algorithm showed the strongest results for a regional algorithm (R^2 ~ 0.40) but Chl$a$ estimates were still largely impacted by high TSM concentrations and CDOM absorption. In order to improve algorithm Chl$a$ retrievals, a hierarchical clustering analysis of the hyperspectral $R_{rs}(\lambda)$ was used to isolate two dominant optical water types: an estuarine and oceanic class. For simplification, a $R_{rs}(\lambda)$ threshold was defined to separate individual spectra into either class appropriately. Algorithms were then re-parameterized and refined to align with the two optical classes. Results showed classification improved algorithm performance for nearly all four algorithms tested. For the OC algorithms the improvements were not significant, even for oceanic class waters where high turbid waters were excluded, as suggested by Komick et al (2009). The 2-band model, however, showed very strong correlation (R^2 ~

0.71; *RMSE* ~ 0.33; S ~ 0.54; I ~ 0.55 µg l^{-1}) for estuarine classified waters. Further data would be needed to make this model more robust, especially to account for reflectance variations caused by particle size distributions, which could affect Chl*a* signal variations (Wozniak & Stramski, 2004).

For oceanic class data the FLH algorithms proved most effective. FLH as a stand-alone model was more correlated (R^2 ~ 0.66; *RMSE* ~ 0.25; S ~ 0.66; I ~ 0.53 µg l^{-1}) to oceanic class *in situ* Chl*a* than the regional version (R^2 ~ 0.37; *RMSE* ~ 0.32; S ~ 0.35; I ~ 1.11 µg l^{-1}), again highlighting the success of classifying water types. This accuracy was further improved in the modified FLH model (R^2 ~ 0.70; *RMSE* ~ 0.26; S ~ 0.70; I ~ 0.47 µg l^{-1}), which took into account the systematic underestimations that the standard FLH model has been documented for (Ioannou et al., 2009; McKee et al., 2007; Zhao et al., 2015). By focusing on Chl*a* absorption near 665 nm, instead of just peak fluorescence, the ModFLH model was less impacted by underlying particulate backscattering and CDOM absorption interference, which can mask the true fluorescence signal (Gower et al., 1999; McKee et al., 2007; Zhao et al., 2015).

In conclusion, the results in this study suggest that an optical classification is an effective way to improve remote sensing Chl*a* retrievals in the Salish Sea. By developing a method to characterize water types into estuarine and oceanic classes, based on individual spectra, we were able to significantly increase the algorithm performance by developing a class-specific algorithm for each water type. These results are not only significant for these coastal waters but could also prove effective for other contrasted coastal Case 2 waters where a similar optical classification likely exists (Mélin & Vantrepotte, 2015). Future work in this study area should involve testing these models with reflectance data from spaceborne sensors, such as MODIS, VIIRS, and the future Sentinel-3, as well as collecting more *in situ* measurements to build model robustness. This information will provide useful primary production information to fisheries management with greater accuracy, which will enable an ecosystem based approach to fisheries management on this coast. Additionally, these results have the potential to extend to other turbid coastal regions which can further our knowledge to effectively monitor the health of the coastal oceans.

Chapter 4 **Conclusion**

The goal of this research was to build a more comprehensive characterization of the optical and biogeochemical properties of the surface waters in the Salish Sea to understand the drivers of remote sensing variability aiming to improve reflectance based algorithms to retrieve surface Chl*a* concentrations. First, spatially and temporally diverse waters were classified according to similar bio-optical regimes. The results of optical classification were then used to validate and parameterize class-specific simulated MODIS-Aqua and Sentinel-3 reflectance based empirical algorithms for deriving Chl*a* with improved accuracy. For estuarine and oceanic classified waters, the 2-band algorithm and the ModFLH algorithms were shown to be the most robust (R^2 ~ 0.72, R^2 ~ 0.70, respectively). This research provided an important characterization of the Salish Sea, which demonstrates the advantage of optimized reflectance based empirical models for achieving more accurate Chl*a* retrievals, not previously done at this scale in this region before.

The Salish Sea is biogeochemically a highly variable coastal system, with Chl*a*, TSM, POC, and CDOM absorption demonstrating a strong spatial and temporal variability, linked to riverine discharge. Dominant phytoplankton blooms were represented by high Chl*a* concentrations (7.2 µg l^{-1}) in the central Salish Sea during the spring, and to a lesser extent in the fall (0.2 µg l^{-1}). A high source of inorganic particulate matter is brought into the region through riverine discharge, which was characterized by high TSM concentrations (20.69 mg l^{-1}). The riverine discharge also contributes with high allochthonous CDOM ($a_{cdom}(443) = 3.072$ m^{-1}; $S_{cdom} = 0.020$ nm^{-1}). Similarly, the optical properties mimicked this variability. Under plume influenced waters, particulate scattering and backscattering were significantly higher (3.084 m^{-1} and 0.042 m^{-1}) than more oceanic conditions (0.514 m^{-1} and 0.015 m^{-1}, respectively) and particle absorption dominated total absorption, confirming the dominant role of riverine systems in this region. Further away from plume influence, waters in the northern and southern regions during summer months showed lower average Chl$a$ (1.07 μg l^{-1}) and TSM concentrations (1.49 mg l^{-1}). This was consistent with the lower magnitudes in scattering (0.514 m^{-1}), backscattering (0.015 m^{-1}), absorption (0.234 m^{-1}) and attenuation (0.756 m^{-1}) observed, although total absorption was dominated by CDOM ($a_{cdom}(443) = 0.344$ m^{-1}; $S_{cdom} = 0.018$ nm^{-1}) in these waters, likely autochthonous from detrital and phytoplankton breakdown (Loos & Costa, 2010).

Based on a statistical hierarchical clustering analysis of normalized remote sensing reflectance, the surface waters of the Salish Sea were separated into four optical classes. Class 1 and 2 were representative of estuarine plume conditions with overall high reflectance magnitudes, particularly in the red, linked to moderate to high TSM concentrations and strong particulate scattering and backscattering that dominated the spectra. Strong attenuation and absorption dominated by particles and allochthonous CDOM was also well defined for these water classes, due to a high fraction of fine inorganic material introduced from riverine discharge. Class 3 demonstrated similar traits to Class 2, representing transitional waters between plume and oceanic conditions under varying TSM influence. TSM concentrations were reduced and high Chl$a$ concentrations were common as light limitations and total attenuation were reduced.

Spectrally distinct $R_{rs}(\lambda)$ in this class was notable, through Chl$a$ absorption and fluorescence features, not masked by TSM as in Class 1. Class 4 signified oceanic waters, with the lowest influence from river plume waters. These waters were characterized by low TSM concentrations and lower Chl$a$ variability, resulting in lower overall $R_{rs}(\lambda)$ magnitudes. Total absorption was low in these waters and dominated by CDOM, as opposed to particulate absorption in Class 1 and 2, which resulted in elevated $R_{rs}(\lambda)$ in the blue spectra, which distinguished this class from all others.

Spectral similarities of the four classes identified through hierarchical clustering, and the results of the EOF analysis revealed that TSM and related scattering and backscattering were responsible for the bulk variation (95%) in $R_{rs}(\lambda)$. This justified a simplification of the classification scheme into two classes: an estuarine class, representing Classes 1 and 2, and an oceanic class comprised of Classes 3 and 4. Following this, thresholds were defined to characterize water types into either classes, based on individual spectra. These thresholds exploited the TSM scattering and CDOM absorption induced $R_{rs}(\lambda)$ variations for the estuarine class, and Chl$a$ absorption features for the oceanic class, which were revealed in the EOF analysis to have high correlation to $R_{rs}(\lambda)$ variability, and subsequent classifications.

Using knowledge of the biogeochemical and optical properties, defined in Chapter 2, reflectance based empirical algorithms were defined and evaluated for retrieving Chl$a$ concentrations. The empirical OC3M/OC3S3, 2-band, FLH and MODFLH algorithms were first parameterized to regional *in situ* biogeochemical and $R_{rs}(\lambda)$ measurements modelled to MODIS Aqua and Sentinel-3 bands based on the regional data set, and then to class-specific data set. The results of regional parameterization showed poor performance for all tested algorithms, largely due to overestimations of lower Chl*a* concentrations caused by TSM scattering and strong CDOM absorption affecting the short blue and green wavelengths. The modified FLH algorithm showed the strongest results for a regional data set (R^2 ~ 0.42) but Chl*a* estimates were still affected by high TSM concentrations and CDOM absorption. A remarked improvement in algorithm performance was achieved through class-specific parameterizations. For the estuarine class waters the 2-band algorithm showed the best statistical results (R^2 ~ 0.72; *RMSE* ~ 0.30; S ~ 0.66; I ~ 0.37 μg l^{-1}). For the ocean class data set the FLH algorithm had an improved correlation (R^2 ~ 0.67), as was expected by removing high TSM and CDOM data. For the oceanic class waters, further improvement was obtained in the ModFLH algorithm (R^2 ~ 0.70; *RMSE* ~ 0.25; S ~ 0.70; I ~ 0.49 μg l^{-1}), which utilizes a 2-band ratio factor to increase Chl*a* estimates in the higher range where the standard FLH algorithm underestimated values. This modification capitalizes on the Chl*a* absorption feature near 665 nm as well as the fluorescence peak near 685 nm to amplify the values retrieved from the standard FLH algorithm.

In summary, the results of this research demonstrate a viable solution to improving ocean colour remote sensing retrievals of Chl*a* in the Case 2 coastal waters of the Salish Sea through reflectance classification. Our results show the FLH and ModFLH model are only moderately effective (R^2 ~ 0.42) at accurately retrieving Chl*a* concentrations in the Salish Sea when parameterized as a regional model. Assumptions that the Salish Sea behaves as one bio-optical region are not valid in these complex coastal waters, as shown in the data presented here. By classifying the optical water properties of this region, we were able to significantly improve algorithm performance through class-specific parametrizations. With this classification a 2-band ratio, focused on red to green bands, and a modified FLH algorithm, were found to be most effective at retrieving Chl*a* for estuarine and oceanic classified waters, respectively. Thus, these results demonstrate original findings for this region on how effective regionalizing algorithms with class-specific data can be for improved Chl*a* retrievals.

Additionally, this research contributes to a growing body of knowledge on the improvement of the use of ocean colour data for defining and monitoring productivity in coastal waters by optical classification. To expand this research further, more data would be required to improve the robustness of the algorithm coefficients, and an application of this technique to real satellite data would be the next step towards validating the accuracies presented here.

The results of this research serve to improve our ability to monitor primary productivity in this coastal environment. With improved estimates of Chl*a*, the ability to effectively monitor the health of the Salish Sea, through an ecosystem-based approach, is possible. By providing this information on spatial and temporal scales, which have traditionally been difficult to obtain, we will be able to more accurately explain fish presence and abundance in our ocean waters towards developing a sustainable fisheries management approach that will ultimately benefit the large portion of the earth's population relying on these rich coastal systems.

Chapter 5 **Bibliography**

Allen, S. E., & Wolfe, M. A. (2013). Hindcast of the timing of the spring phytoplankton bloom in the Strait of Georgia, 1968–2010. *Strait of Georgia Ecosystem Research Initiative (ERI)*, *115*(0), 6–13. http://doi.org/http://dx.doi.org.ezproxy.library.uvic.ca/10.1016/j.pocean.2013.05.026

Andres Araujo, H., Holt, C., Curtis, J. M. R., Perry, R. I., Irvine, J. R., & Michielsens, C. G. J. (2013). Building an ecosystem model using mismatched and fragmented data: A probabilistic network of early marine survival for coho salmon Oncorhynchus kisutch in the Strait of Georgia. *Strait of Georgia Ecosystem Research Initiative (ERI)*, *115*(0), 41–52. http://doi.org/http://dx.doi.org/10.1016/j.pocean.2013.05.022

Antoine, D. (2005). Bridging ocean color observations of the 1980s and 2000s in search of long-term trends. *Journal of Geophysical Research*, *110*(C6), C06009. http://doi.org/10.1029/2004JC002620

Antoine, D., André, J.-M., & Morel, A. (1996). Oceanic primary production: 2. Estimation at global scale from satellite (Coastal Zone Color Scanner) chlorophyll. *Global Biogeochemical Cycles*, *10*(1), 57–69. http://doi.org/10.1029/95GB02832

Arar, E. J. (1997). Determination of chlorophylls a and b and identification of other pigments of interest in marine and freshwater algae using high performance liquid chromatography with visible wavelength detection. *Methods for the Determination of Chemical Substances in Marine and Estuarine Environmental Matrices*, *447*, 1–20.

Aurin, D. A., Dierssen, H. M., Twardowski, M. S., & Roesler, C. S. (2010). Optical complexity in Long Island Sound and implications for coastal ocean color remote sensing. *Journal of Geophysical Research: Oceans (1978–2012)*, *115*(C7).

Bailey, S. W., & Werdell, P. J. (2006). A multi-sensor approach for the on-orbit validation of ocean color satellite data products. *Remote Sensing of Environment*, *102*(1-2), 12–23. http://doi.org/10.1016/j.rse.2006.01.015

Baker, E. T., & Lavelle, J. W. (1984). The effect of particle size on the light attenuation coefficient of natural suspensions. *Journal of Geophysical Research: Oceans (1978–2012)*, *89*(C5), 8197–8203.

Barille-Boyer, A.-L., Barille, L., Masse, H., Razet, D., & Heral, M. (2003). Correction for particulate organic matter as estimated by loss on ignition in estuarine ecosystems. *Estuarine, Coastal and Shelf Science*, *58*(1), 147–153.

Beamish, R. J., Neville, C., Sweeting, R., & Lange, K. (2012). The Synchronous Failure of Juvenile Pacific Salmon and Herring Production in the Strait of Georgia in 2007 and the Poor Return of Sockeye Salmon to the Fraser River in 2009. *Marine and Coastal Fisheries*, *4*(1), 403–414. http://doi.org/10.1080/19425120.2012.676607

Behrenfeld, M. J., O'Malley, R. T., Siegel, D. A., McClain, C. R., Sarmiento, J. L., Feldman, G. C., … Boss, E. S. (2006). Climate-driven trends in contemporary ocean productivity. *Nature*, *444*(7120), 752–5. http://doi.org/10.1038/nature05317

Berger, M., Moreno, J., Johannessen, J. A., Levelt, P. F., & Hanssen, R. F. (2012). ESA's sentinel missions in support of Earth system science. *Remote Sensing of Environment*, *120*, 84–90. http://doi.org/10.1016/j.rse.2011.07.023

Berkhin, P. (2006). A survey of clustering data mining techniques. In *Grouping multidimensional data* (pp. 25–71). Springer.

Bierman, P., Lewis, M., Ostendorf, B., & Tanner, J. (2011). A review of methods for analysing spatial and temporal patterns in coastal water quality. *Ecological Indicators*, *11*(1), 103–114. http://doi.org/10.1016/j.ecolind.2009.11.001

Bisutti, I., Hilke, I., & Raessler, M. (2004). Determination of total organic carbon–an overview of current methods. *TrAC Trends in Analytical Chemistry*, *23*(10), 716–726.

Boss, E., & Pegau, W. S. (2001). Relationship of light scattering at an angle in the backward direction to the backscattering coefficient. *Applied Optics*, *40*(30), 5503–5507.

Boyce, D. G., Lewis, M. R., & Worm, B. (2010). Global phytoplankton decline over the past century. *Nature*, *466*(7306), 591–596. http://doi.org/10.1038/nature09268

Brewin, R. J. W., Sathyendranath, S., Müller, D., Brockmann, C., Deschamps, P.-Y., Devred, E., … White, G. N. (2015). The Ocean Colour Climate Change Initiative: III. A round-robin comparison on in-water bio-optical algorithms. *Remote Sensing of Environment*, *162*, 271–294. http://doi.org/10.1016/j.rse.2013.09.016

Cannizzaro, J. P., & Carder, K. L. (2006). Estimating chlorophyll a concentrations from remote-sensing reflectance in optically shallow waters. *Remote Sensing of Environment*, *101*(1), 13–24. http://doi.org/10.1016/j.rse.2005.12.002

Carder, K. L., Chen, F. R., Lee, Z. P., Hawes, S. K., & Kamykowski, D. (1999). Semianalytic Moderate-Resolution Imaging Spectrometer algorithms for chlorophyll a and absorption with bio-optical domains based on nitrate-depletion temperatures.

Journal of Geophysical Research, *104*(C3), 5403. http://doi.org/10.1029/1998JC900082

Carder, K. L., Steward, R. G., Harvey, G. R., & Ortner, P. B. (1989). Marine humic and fulvic acids: Their effects on remote sensing of ocean chlorophyll. *Limnology and Oceanography*, *34*(1), 68–81. http://doi.org/10.4319/lo.1989.34.1.0068

Carswell, T., Costa, M., & Gower, J. (2015). *Analysis of MODIS-Aqua imagery to determine spring phytoplankton phenology in the Strait of Georgia, Canada*. University of Victoria.

Chassot, E., Bonhommeau, S., Reygondeau, G., Nieto, K., Polovina, J. J., Huret, M., … Demarcq, H. (2011). Satellite remote sensing for an ecosystem approach to fisheries management. *ICES Journal of Marine Science*, *68*(4), 651–666. http://doi.org/10.1093/icesjms/fsq195

Chen, J., Hu, X. F., & Quan, W. T. (2012). A multi-band semi-analytical algorithm for estimating chlorophyll-a concentration in the Yellow River Estuary, China. *Water Environ.Res*.

Chen, J., & Quan, W. (2013). An improved algorithm for retrieving chlorophyll-a from the Yellow River Estuary using MODIS imagery. *Environmental Monitoring and Assessment*, *185*(3), 2243–55. http://doi.org/10.1007/s10661-012-2705-y

Collins, A. K., Allen, S. E., & Pawlowicz, R. (2009). The role of wind in determining the timing of the spring bloom in the Strait of Georgia. *Canadian Journal of Fisheries and Aquatic Sciences*, *66*(9), 1597–1616.

Craig, S. E., Jones, C. T., Li, W. K. W., Lazin, G., Horne, E., Caverhill, C., & Cullen, J. J. (2012). Deriving optical metrics of coastal phytoplankton biomass from ocean colour. *Remote Sensing of Environment*, *119*(0), 72–83. http://doi.org/http://dx.doi.org/10.1016/j.rse.2011.12.007

Dall’Olmo, G., Gitelson, A. A., Rundquist, D. C., Leavitt, B., Barrow, T., & Holz, J. C. (2005). Assessing the potential of SeaWiFS and MODIS for estimating chlorophyll concentration in turbid productive waters using red and near-infrared bands. *Remote Sensing of Environment*, *96*(2), 176–187. http://doi.org/10.1016/j.rse.2005.02.007

Darecki, M., & Stramski, D. (2004). An evaluation of MODIS and SeaWiFS bio-optical algorithms in the Baltic Sea. *Remote Sensing of Environment*, *89*(3), 326–350. http://doi.org/10.1016/j.rse.2003.10.012

Del Vecchio, R., & Blough, N. V. (2002). Photobleaching of chromophoric dissolved organic matter in natural waters: kinetics and modeling. *Marine Chemistry*, *78*(4), 231–253. http://doi.org/10.1016/S0304-4203(02)00036-1

Diaz, R. J., & Rosenberg, R. (2008). Spreading dead zones and consequences for marine ecosystems. *Science (New York, N.Y.)*, *321*(5891), 926–9. http://doi.org/10.1126/science.1156401

Doney, S. C., Ruckelshaus, M., Duffy, J. E., Barry, J. P., Chan, F., English, C. A., … Talley, L. D. (2012). Climate change impacts on marine ecosystems. *Annual Review of Marine Science*, *4*, 11–37. http://doi.org/10.1146/annurev-marine-041911-111611

Donlon, C., Berruti, B., Buongiorno, A., Ferreira, M.-H., Féménias, P., Frerick, J., … Sciarra, R. (2012). The Global Monitoring for Environment and Security (GMES) Sentinel-3 mission. *Remote Sensing of Environment*, *120*, 37–57. http://doi.org/10.1016/j.rse.2011.07.024

Duin, E. H. S. Van, Blom, G., Los, F. J., Maffione, R., Zimmerman, R., Cerco, C. F., … Best, E. P. H. (2001). Modeling underwater light climate in relation to sedimentation, resuspension, water quality and autotrophic growth. *Hydrobiologia*, *444*(1-3), 25–42. http://doi.org/10.1023/A:1017512614680

Eaton, A. D., Clesceri, L. S., Rice, E. W., Greenberg, A. E., & Franson, M. (2005). 2540D. Total suspended solids dried at 103–105 C. *Standard Methods for the Examination of Water and Wastewater*, *21*.

Environmental Canada. (2014). Retrieved from http://wateroffice.ec.gc.ca

Esaias, W. E., Abbott, M. R., Barton, I., Brown, O. B., Campbell, J. W., Carder, K. L., … Minnett, P. J. (1998). An overview of MODIS capabilities for ocean science observations. *IEEE Transactions on Geoscience and Remote Sensing*, *36*(4), 1250–1265. http://doi.org/10.1109/36.701076

Feldman, G. C. (2012). OceanColor Documents.

Feng, H., Campbell, J., Dowell, M., & Moore, T. (2005). Modeling spectral reflectance of optically complex waters using bio-optical measurements from Tokyo Bay. *Remote Sensing of Environment*, *99*(3), 232–243. http://doi.org/10.1016/j.rse.2005.08.015

Field, C. B. (1998). Primary Production of the Biosphere: Integrating Terrestrial and Oceanic Components. *Science*, *281*(5374), 237–240. http://doi.org/10.1126/science.281.5374.237

Floricioiu, D., Rott, H., Rott, E., Dokulil, M., & Defrancesco, C. (2003). Retrieval of limnological parameters of perialpine lakes by means of MERIS data. *Limnology*, *16*(09), 44.

Frette, Ø., Stamnes, J. J., & Stamnes, K. (1998). Optical Remote Sensing of Marine Constituents in Coastal Waters: A Feasibility Study. *Applied Optics*, *37*(36), 8318. http://doi.org/10.1364/AO.37.008318

Gallegos, C. L., Jordan, T. E., Hines, A. H., & Weller, D. E. (2005). Temporal variability of optical properties in a shallow, eutrophic estuary: Seasonal and interannual variability. *Estuarine, Coastal and Shelf Science*, *64*(2), 156–170. http://doi.org/10.1016/j.ecss.2005.01.013

Garcia, C. A. E., Garcia, V. M. T., & McClain, C. R. (2005). Evaluation of SeaWiFS chlorophyll algorithms in the Southwestern Atlantic and Southern Oceans. *Remote Sensing of Environment*, *95*(1), 125–137. http://doi.org/10.1016/j.rse.2004.12.006

Garcia, V. M. T., Signorini, S., Garcia, C. A. E., & McClain, C. R. (2006). Empirical and semi-analytical chlorophyll algorithms in the south-western Atlantic coastal region (25–40°S and 60–45°W). *International Journal of Remote Sensing*, *27*(8), 1539–1562. http://doi.org/10.1080/01431160500382857

Gattuso, J.-P., Frankignoulle, M., & Wollast, R. (2003). Carbon and carbonate metabolism in coastal aquatic ecosystems. Retrieved from http://www.annualreviews.org.ezproxy.library.uvic.ca/doi/abs/10.1146/annurev.ecolsys.29.1.405

Gilerson, A., Zhou, J., Hlaing, S., Ioannou, I., Gross, B., Moshary, F., & Ahmed, S. (2008). Fluorescence Component in the Reflectance Spectra from Coastal Waters. II. Performance of retrieval algorithms. *Optics Express*, *16*(4), 2446. http://doi.org/10.1364/OE.16.002446

Gilerson, A., Zhou, J., Hlaing, S., Ioannou, I., Schalles, J., Gross, B., … Ahmed, S. (2007). Fluorescence component in the reflectance spectra from coastal waters. Dependence on water composition. *Optics Express*, *15*(24), 15702. http://doi.org/10.1364/OE.15.015702

Gitelson, A. (1992). The peak near 700 nm on radiance spectra of algae and water: relationships of its magnitude and position with chlorophyll concentration. *International Journal of Remote Sensing*, *13*(17), 3367–3373. http://doi.org/10.1080/01431169208904125

Gitelson, A. A., Schalles, J. F., & Hladik, C. M. (2007). Remote chlorophyll-a retrieval in turbid, productive estuaries: Chesapeake Bay case study. *Remote Sensing of Environment*, *109*(4), 464–472. http://doi.org/10.1016/j.rse.2007.01.016

Gordon, H. R., Brown, O. B., Evans, R. H., Brown, J. W., Smith, R. C., Baker, K. S., &

Clark, D. K. (1988). A semianalytic radiance model of ocean color. *Journal of Geophysical Research: Atmospheres (1984–2012), 93*(D9), 10909–10924.

Gordon, H. R., & Morel, A. Y. (1983). Remote assessment of ocean color for interpretation of satellite visible imagery: A review. Retrieved from http://ntrs.nasa.gov/search.jsp?R=19840054510

Gordon, H. R., & Wang, M. (1994). Retrieval of water-leaving radiance and aerosol optical thickness over the oceans with SeaWiFS: a preliminary algorithm. *Applied Optics*, *33*(3), 443. http://doi.org/10.1364/AO.33.000443

Gould, R. W., Arnone, R. A., & Martinolich, P. M. (1999). Spectral dependence of the scattering coefficient in case 1 and case 2 waters. *Applied Optics*, *38*(12), 2377–2383.

Gower, J. (1980). Observations of in situ fluorescence of chlorophyll-a in Saanich Inlet. *Boundary-Layer Meteorology*, *18*(3), 235–245.

Gower, J., Brown, L., & Borstad, G. A. (2004). Observation of chlorophyll fluorescence in west coast waters of Canada using the MODIS satellite sensor. *Canadian Journal of Remote Sensing*, *30*(1), 17–25. http://doi.org/10.5589/m03-048

Gower, J., Doerffer, R., & Borstad, G. A. (1999). Interpretation of the 685nm peak in water-leaving radiance spectra in terms of fluorescence, absorption and scattering, and its observation by MERIS. *International Journal of Remote Sensing*. Retrieved from http://www-tandfonline-com.ezproxy.library.uvic.ca/doi/abs/10.1080/014311699212470

Gower, J., King, S., Statham, S., Fox, R., & Young, E. (2013). The Malaspina Dragon: A newly-discovered pattern of the early spring bloom in the Strait of Georgia, British Columbia, Canada. *Progress in Oceanography*, *115*, 181–188. http://doi.org/10.1016/j.pocean.2013.05.024

Halpern, B. S., Frazier, M., Potapenko, J., Casey, K. S., Koenig, K., Longo, C., … Walbridge, S. (2015). Spatial and temporal changes in cumulative human impacts on the world's ocean. *Nature Communications, 6*, 7615. http://doi.org/10.1038/ncomms8615

Halverson, M. J., & Pawlowicz, R. (2013). High-resolution observations of chlorophyll-a biomass from an instrumented ferry: Influence of the Fraser River plume from 2003 to 2006. *Continental Shelf Research*, *59*, 52–64. http://doi.org/10.1016/j.csr.2013.04.010

Harding, L. W., Magnuson, A., & Mallonee, M. E. (2005). SeaWiFS retrievals of chlorophyll in Chesapeake Bay and the mid-Atlantic bight. *Estuarine, Coastal and Shelf Science*, *62*(1-2), 75–94. http://doi.org/10.1016/j.ecss.2004.08.011

Harrison, P. J., Fulton, J. D., Taylor, F. J. R., & Parsons, T. R. (1983). Review of the biological oceanography of the Strait of Georgia: pelagic environment. *Canadian Journal of Fisheries and Aquatic Sciences*, *40*(7), 1064–1094.

Harvey, E. T., Kratzer, S., & Philipson, P. (2015). Satellite-based water quality monitoring for improved spatial and temporal retrieval of chlorophyll-a in coastal waters. *Remote Sensing of Environment*, *158*, 417–430. http://doi.org/10.1016/j.rse.2014.11.017

Helms, J. R., Stubbins, A., Ritchie, J. D., Minor, E. C., Kieber, D. J., & Mopper, K. (2008). Absorption spectral slopes and slope ratios as indicators of molecular weight, source, and photobleaching of chromophoric dissolved organic matter. *Limnology and Oceanography*, *53*(3), 955–969. http://doi.org/10.4319/lo.2008.53.3.0955

Hoge, F. E., Lyon, P. E., Swift, R. N., Yungel, J. K., Abbott, M. R., Letelier, R. M., & Esaias, W. E. (2003). Validation of Terra-MODIS Phytoplankton Chlorophyll Fluorescence Line Height. I. Initial Airborne Lidar Results. *Applied Optics*, *42*(15), 2767. http://doi.org/10.1364/AO.42.002767

Hooker, S. B., & McClain, C. R. (2000). The calibration and validation of SeaWiFS data. *Progress in Oceanography*, *45*(3-4), 427–465. http://doi.org/10.1016/S0079-6611(00)00012-4

Hooker, S. B., & Morel, A. (2003). Platform and environmental effects on above-water determinations of water-leaving radiances. *Journal of Atmospheric and Oceanic Technology*, *20*(1), 187–205.

Huot, Y., Brown, C. A., & Cullen, J. J. (2005). New algorithms for MODIS sun-induced chlorophyll fluorescence and a comparison with present data products. *Limnology and Oceanography: Methods*, *3*(2), 108–130. http://doi.org/10.4319/lom.2005.3.108

Ioannou, I., Zhou, J., Gilerson, A., Gross, B., Moshary, F., & Ahmed, S. (2009). New Algorithm for MODIS chlorophyll Fluorescence Height Retrieval: performance and comparison with the current product. In C. R. Bostater, Jr., S. P. Mertikas, X. Neyt, & M. Velez-Reyes (Eds.), *SPIE Europe Remote Sensing* (pp. 747309–747309–9). International Society for Optics and Photonics. http://doi.org/10.1117/12.830630

IOCCG. (2006). *Remote sensing of inherent optical properties: Fundamentals, tests of algorithms, and applications. International Ocean-Colour Coordinating Group*

(Vol. 5). Dartmouth, Canada.

Joergensen, P. V. (2004). SeaWiFS data analysis and match-ups with in situ chlorophyll concentrations in Danish waters. *International Journal of Remote Sensing*, *25*(7-8), 1397–1402.

Johannessen, S. C., Macdonald, R. W., & Paton, D. W. (2003). A sediment and organic carbon budget for the greater Strait of Georgia. *Estuarine, Coastal and Shelf Science*, *56*(3), 845–860.

Johannessen, S. C., Potentier, G., Wright, C. A., Masson, D., & Macdonald, R. W. (2008). Water column organic carbon in a Pacific marginal sea (Strait of Georgia, Canada). *Marine Environmental Research*, *66*, S49–S61.

Johannessen, S., Masson, D., & Macdonald, R. W. (2006). Distribution and cycling of suspended particles inferred from transmissivity in the strait of Georgia, ham strait and Juan de Fuca Strait. *Atmosphere-Ocean*, *44*(1), 17–27.

Jun Chen, Minwei Zhang, Tingwei Cui, & Zhenhe Wen. (2013). A Review of Some Important Technical Problems in Respect of Satellite Remote Sensing of Chlorophyll-a Concentration in Coastal Waters. *IEEE Journal of Selected Topics in Applied Earth Observations and Remote Sensing*, *6*(5), 2275–2289. http://doi.org/10.1109/JSTARS.2013.2242845

Komick, N. M., Costa, M. P. F., & Gower, J. (2009). Bio-optical algorithm evaluation for MODIS for western Canada coastal waters: An exploratory approach using in situ reflectance. *Remote Sensing of Environment*, *113*(4), 794–804. http://doi.org/10.1016/j.rse.2008.12.005

Lavender, S. J., Pinkerton, M. H., Froidefond, J.-M., Morales, J., Aiken, J., & Moore, G. F. (2004). SeaWiFS validation in European coastal waters using optical and bio-geochemical measurements. *International Journal of Remote Sensing*, *25*(7-8), 1481–1488. http://doi.org/10.1080/01431160310001592481

Le, C., Hu, C., Cannizzaro, J., English, D., Muller-Karger, F., & Lee, Z. (2013a). Evaluation of chlorophyll-a remote sensing algorithms for an optically complex estuary. *Remote Sensing of Environment*, *129*, 75–89. http://doi.org/10.1016/j.rse.2012.11.001

Le, C., Hu, C., English, D., Cannizzaro, J., Chen, Z., Kovach, C., … Carder, K. L. (2013b). Inherent and apparent optical properties of the complex estuarine waters of Tampa Bay: what controls light? *Estuarine, Coastal and Shelf Science*, *117*, 54–69.

Le, C., Li, Y., Zha, Y., Sun, D., Huang, C., & Lu, H. (2009). A four-band semi-analytical model for estimating chlorophyll a in highly turbid lakes: The case of Taihu Lake, China. *Remote Sensing of Environment*, *113*(6), 1175–1182. http://doi.org/10.1016/j.rse.2009.02.005

Le, C., Li, Y., Zha, Y., Sun, D., Huang, C., & Zhang, H. (2011). Remote estimation of chlorophyll a in optically complex waters based on optical classification. *Remote Sensing of Environment*, *115*(2), 725–737. http://doi.org/10.1016/j.rse.2010.10.014

Li, M., Gargett, A., & Denman, K. (2000). What Determines Seasonal and Interannual Variability of Phytoplankton and Zooplankton in Strongly Estuarine Systems? *Estuarine, Coastal and Shelf Science*, *50*(4), 467–488.

Loisel, H., Lubac, B., Dessailly, D., Duforet-Gaurier, L., & Vantrepotte, V. (2010). Effect of inherent optical properties variability on the chlorophyll retrieval from ocean color remote sensing: an in situ approach. *Optics Express*, *18*(20), 20949–20959.

Loos, E. A., & Costa, M. (2010). Inherent optical properties and optical mass classification of the waters of the Strait of Georgia, British Columbia, Canada. *Progress in Oceanography*, *87*(1-4), 144–156. http://doi.org/10.1016/j.pocean.2010.09.004

Loos, E., Costa, M., Niemann, O., Johannessen, S., & Brolo, A. (2009). *Optical properties of the waters of the Strait of Georgia, BC, Canada*.

Lubac, B., & Loisel, H. (2007). Variability and classification of remote sensing reflectance spectra in the eastern English Channel and southern North Sea. *Remote Sensing of Environment*, *110*(1), 45–58.

Mackas, D., Galbraith, M., Faust, D., Masson, D., Young, K., Shaw, W., … El-Sabaawi, R. (2013). Zooplankton time series from the Strait of Georgia: Results from year-round sampling at deep water locations, 1990–2010. *Strait of Georgia Ecosystem Research Initiative (ERI)*, *115*(0), 129–159. http://doi.org/http://dx.doi.org/10.1016/j.pocean.2013.05.019

Mackas, D. L., & Harrison, P. J. (1997). Nitrogenous Nutrient Sources and Sinks in the Juan de Fuca Strait/Strait of Georgia/Puget Sound Estuarine System: Assessing the Potential for Eutrophication. *Estuarine, Coastal and Shelf Science*, *44*(1), 1–21. http://doi.org/10.1006/ecss.1996.0110

Macoun, P., Dewey, R., & Round, A. (2010). VENUS-a bottom up approach to building an ocean observing system. In *OCEANS 2010 IEEE-Sydney* (pp. 1–9). IEEE.

Maritorena, S., Siegel, D. A., & Peterson, A. R. (2002). Optimization of a semianalytical ocean color model for global-scale applications. *Applied Optics*, *41*(15), 2705. http://doi.org/10.1364/AO.41.002705

Masson, D. (2002). Deep Water Renewal in the Strait of Georgia. *Estuarine, Coastal and Shelf Science*, *54*(1), 115–126. http://doi.org/10.1006/ecss.2001.0833

Masson, D., & Peña, A. (2009). Chlorophyll distribution in a temperate estuary: The Strait of Georgia and Juan de Fuca Strait. *Estuarine, Coastal and Shelf Science*, *82*(1), 19–28. http://doi.org/10.1016/j.ecss.2008.12.022

Masson, D., & Perry, R. I. (2013). The Strait of Georgia Ecosystem Research Initiative: An overview. *Progress in Oceanography*, *115*, 1–5. http://doi.org/10.1016/j.pocean.2013.05.009

Matthews, M. W. (2011). A current review of empirical procedures of remote sensing in inland and near-coastal transitional waters. *International Journal of Remote Sensing*, *32*(21), 6855–6899. http://doi.org/10.1080/01431161.2010.512947

McCain, C., Hooker, S., Feldman, G., & Bontempi, P. (2006). Satellite data for ocean biology, biogeochemistry, and climate research. *Eos, Transactions American Geophysical Union*, *87*(34), 337. http://doi.org/10.1029/2006EO340002

McKee, D., Cunningham, A., Wright, D., & Hay, L. (2007). Potential impacts of nonalgal materials on water-leaving Sun induced chlorophyll fluorescence signals in coastal waters. *Applied Optics*, *46*(31), 7720. http://doi.org/10.1364/AO.46.007720

Mélin, F., & Vantrepotte, V. (2015). How optically diverse is the coastal ocean? *Remote Sensing of Environment*, *160*, 235–251. http://doi.org/10.1016/j.rse.2015.01.023

Mitchell, B. G., Kahru, M., Wieland, J., & Stramska, M. (2002). Determination of spectral absorption coefficients of particles, dissolved material and phytoplankton for discrete water samples. *Ocean Optics Protocols for Satellite Ocean Color Sensor validation.Revision*, *3*, 231–257.

Mobley, C. D., & Sundman, L. K. (2008). Hydrolight 5, Ecolight 5, Technical documentation. Sequoia Scientific. *Inc, Bellevue*.

Mobley, C. D., Sundman, L. K., & Boss, E. (2002). Phase function effects on oceanic light fields. *Applied Optics*, *41*(6), 1035–1050.

Moore, T. S., Campbell, J. W., & Dowell, M. D. (2009). A class-based approach to characterizing and mapping the uncertainty of the MODIS ocean chlorophyll product. *Remote Sensing of Environment*, *113*(11), 2424–2430.

Moore, T. S., Dowell, M. D., Bradt, S., & Verdu, A. R. (2014). An optical water type framework for selecting and blending retrievals from bio-optical algorithms in lakes and coastal waters. *Remote Sensing of Environment*, *143*, 97–111. http://doi.org/10.1016/j.rse.2013.11.021

Morel, A., & Prieur, L. (1977). Analysis of variations in ocean color. *Limnology and Oceanography*, *22*(4), 709–722. http://doi.org/10.4319/lo.1977.22.4.0709

Moses, W. J., Gitelson, A. A., Berdnikov, S., & Povazhnyy, V. (2009a). Estimation of chlorophyll- a concentration in case II waters using MODIS and MERIS data—successes and challenges. *Environmental Research Letters*, *4*(4), 045005. http://doi.org/10.1088/1748-9326/4/4/045005

Moses, W. J., Gitelson, A. A., Berdnikov, S., & Povazhnyy, V. (2009b). Satellite Estimation of Chlorophyll-a Concentration Using the Red and NIR Bands of MERIS—The Azov Sea Case Study. *IEEE Geoscience and Remote Sensing Letters*, *6*(4), 845–849. http://doi.org/10.1109/LGRS.2009.2026657

Mouw, C. B., Greb, S., Aurin, D., DiGiacomo, P. M., Lee, Z., Twardowski, M., … Craig, S. E. (2015). Aquatic color radiometry remote sensing of coastal and inland waters: Challenges and recommendations for future satellite missions. *Remote Sensing of Environment*, *160*, 15–30. http://doi.org/10.1016/j.rse.2015.02.001

Mueller, J. L. (1976). Ocean color spectra measured off the Oregon coast: characteristic vectors. *Applied Optics*, *15*(2), 394–402.

Mueller, J. L., McClain, G. S. F. C. R., Mueller, J. L., Bidigare, R. R., Trees, C., Balch, W. M., … Van, L. (2003). Ocean optics protocols for satellite ocean color sensor validation, revision 5, volume V: Biogeochemical and bio-optical measurements and data analysis protocols. *NASA Tech.Memo*, *211621*, 36.

Mustapha, S. Ben, Bélanger, S., & Larouche, P. (2012). Evaluation of ocean color algorithms in the southeastern Beaufort Sea, Canadian Arctic: New parameterization using SeaWiFS, MODIS, and MERIS spectral bands. *Canadian Journal of Remote Sensing*, *38*(5), 535–556. http://doi.org/10.5589/m12-045

Nagamani, P. V., Chauhan, P., & Dwivedi, R. M. (2008). Development of Chlorophyll-a Algorithm for Ocean Colour Monitor Onboard OCEANSAT-2 Satellite. *IEEE Geoscience and Remote Sensing Letters*, *5*(3), 527–531. http://doi.org/10.1109/LGRS.2008.923213

Neville, R. A., & Gower, J. F. R. (1977). Passive remote sensing of phytoplankton via chlorophyll α fluorescence. *Journal of Geophysical Research*, *82*(24), 3487–3493.

Novoa, S., Chust, G., Valencia, V., Froidefond, J.-M., & Morichon, D. (2011).

Estimation of chlorophyll- a concentration in waters over the continental shelf of the Bay of Biscay: a comparison of remote sensing algorithms. *International Journal of Remote Sensing*, *32*(23), 8349–8371. http://doi.org/10.1080/01431161.2010.540588

O'Reilly, J. E. (2000). *SeaWiFS Postlaunch Technical Report Series: SeaWiFS Postlaunch Calibration and Validation Analyses, Part 3*. National Aeronautics and Space Administration, Goddard Space Flight Center.

O'Reilly, J. E., Maritorena, S., Mitchell, B. G., Siegel, D. A., Carder, K. L., Garver, S. A., … McClain, C. (1998). Ocean color chlorophyll algorithms for SeaWiFS. *Journal of Geophysical Research*, *103*(C11), 24937. http://doi.org/10.1029/98JC02160

Oliver, M. J. (2004). Deriving in situ phytoplankton absorption for bio-optical productivity models in turbid waters. *Journal of Geophysical Research*, *109*(C7), C07S11. http://doi.org/10.1029/2002JC001627

Pan, X., Mannino, A., Russ, M. E., & Hooker, S. B. (2008). Remote sensing of the absorption coefficients and chlorophyll a concentration in the United States southern Middle Atlantic Bight from SeaWiFS and MODIS-Aqua. *Journal of Geophysical Research*, *113*(C11), C11022. http://doi.org/10.1029/2008JC004852

Pauly, D., Christensen, V., Guénette, S., Pitcher, T. J., Sumaila, U. R., Walters, C. J., … Zeller, D. (2002). Towards sustainability in world fisheries. *Nature*, *418*(6898), 689–95. http://doi.org/10.1038/nature01017

Pawlowicz, R., Riche, O., & Halverson, M. (2007). The circulation and residence time of the strait of Georgia using a simple mixing-box approach. *Atmosphere-Ocean*, *45*(4), 173–193. http://doi.org/10.3137/ao.450401

Pegau, S., Zaneveld, J. R. V, Mitchell, B. G., Mueller, J. L., Kahru, M., Wieland, J., & Stramska, M. (2003). Ocean optics protocols for satellite ocean color sensor validation, Revision 4, Volume IV: Inherent optical properties: instruments, characterizations, field measurements, and data analysis protocols. *NASA Tech.Memo*, *211621*.

Pelloquin, C., & Nieke, J. (2012). *Sentinel-3 OLCI and SLSTR simulated spectral response functions*.

Pope, R. M., & Fry, E. S. (1997). Absorption spectrum (380–700 nm) of pure water. II. Integrating cavity measurements. *Applied Optics*, *36*(33), 8710–8723.

Preikshot, D., Beamish, R. J., Sweeting, R. M., Neville, C. M., & Beacham, T. D. (2012). The Residence Time of Juvenile Fraser River Sockeye Salmon in the Strait of

Georgia. *Marine and Coastal Fisheries*, *4*(1), 438–449. http://doi.org/10.1080/19425120.2012.683235

Riche, O., Johannessen, S. C. C., & Macdonald, R. W. W. (2014). Why timing matters in a coastal sea: Trends, variability and tipping points in the Strait of Georgia, Canada. *Journal of Marine Systems*, *131*, 36–53. http://doi.org/10.1016/j.jmarsys.2013.11.003

Ruddick, K., De Cauwer, V., Park, Y.-J., & Moore, G. (2006). Seaborne measurements of near infrared water-leaving reflectance: The similarity spectrum for turbid waters.

Sathyendranath, S., Cota, G., Stuart, V., Maass, H., & Platt, T. (2001). Remote sensing of phytoplankton pigments: A comparison of empirical and theoretical approaches. *International Journal of Remote Sensing*, *22*(2-3), 249–273. http://doi.org/10.1080/014311601449925

Sathyendranath, S., Prieur, L., & Morel, A. (1989). A three-component model of ocean colour and its application to remote sensing of phytoplankton pigments in coastal waters. *International Journal of Remote Sensing*, *10*(8), 1373–1394.

Sathyendranath, S., Stuart, V., Irwin, B. D., Maass, H., Savidge, G., Gilpin, L., & Platt, T. (1999). Seasonal variations in bio-optical properties of phytoplankton in the Arabian Sea. *Deep Sea Research Part II: Topical Studies in Oceanography*, *46*(3-4), 633–653. http://doi.org/10.1016/S0967-0645(98)00121-0

Sauer, M. J., Roesler, C. S., Werdell, P. J., & Barnard, A. (2012). Under the hood of satellite empirical chlorophyll a algorithms: revealing the dependencies of maximum band ratio algorithms on inherent optical properties. *Optics Express*, *20*(19), 20920–20933.

Schalles, J. F., Rundquist, D. C., & Schiebe, F. R. (2002). The influence of suspended clays on phytoplankton reflectance signatures and the remote estimation of chlorophyll. *Verhandlungen Der Internationalen Vereinigung Für Theoretische Und Angewandte Limnologie*, *27*(6), 3619–3625.

Schweigert, J. F., Thompson, M., Fort, C., Hay, D. E., Therriault, T. W., & Brown, L. N. (2013). Factors linking Pacific herring (Clupea pallasi) productivity and the spring plankton bloom in the Strait of Georgia, British Columbia, Canada. *Strait of Georgia Ecosystem Research Initiative (ERI)*, *115*(0), 103–110. http://doi.org/http://dx.doi.org/10.1016/j.pocean.2013.05.017

Shen, F., Zhou, Y.-X., Li, D.-J., Zhu, W.-J., & Suhyb Salama, M. (2010). Medium resolution imaging spectrometer (MERIS) estimation of chlorophyll- a concentration in the turbid sediment-laden waters of the Changjiang (Yangtze) Estuary. *International Journal of Remote Sensing*, *31*(17-18), 4635–4650. http://doi.org/10.1080/01431161.2010.485216

Small, C., & Nicholls, R. (2003). A Global Analysis of Human Settlement in Coastal Zones on JSTOR. *Journal of Coastal Research*, *19*(3), 584–599.

Stavn, R. H., Rick, H. J., & Falster, A. V. (2009). Correcting the errors from variable sea salt retention and water of hydration in loss on ignition analysis: Implications for studies of estuarine and coastal waters. *Estuarine, Coastal and Shelf Science*, *81*(4), 575–582.

Steinacher, M., Joos, F., Frölicher, T. L., Bopp, L., Cadule, P., Cocco, V., … Segschneider, J. (2010). Projected 21st century decrease in marine productivity: a multi-model analysis. *Biogeosciences*, *7*(3), 979–1005. http://doi.org/10.5194/bg-7-979-2010

Sullivan, J. M., Twardowski, M. S., Donaghay, P. L., & Freeman, S. A. (2005). Use of optical scattering to discriminate particle types in coastal waters. *Applied Optics*, *44*(9), 1667. http://doi.org/10.1364/AO.44.001667

Sullivan, J. M., Twardowski, M. S., Zaneveld, J. R. V, Moore, C. M., Barnard, A. H., Donaghay, P. L., & Rhoades, B. (2006). Hyperspectral temperature and salt dependencies of absorption by water and heavy water in the 400-750 nm spectral range. *Applied Optics*, *45*(21), 5294–5309.

Sutherland, D. A., MacCready, P., Banas, N. S., & Smedstad, L. F. (2011). A Model Study of the Salish Sea Estuarine Circulation*. *Journal of Physical Oceanography*, *41*(6), 1125–1143. http://doi.org/10.1175/2011JPO4540.1

Swaney, D. P., Hong, B., Ti, C., Howarth, R. W., & Humborg, C. (2012). Net anthropogenic nitrogen inputs to watersheds and riverine N export to coastal waters: a brief overview. *Current Opinion in Environmental Sustainability*, *4*(2), 203–211. http://doi.org/10.1016/j.cosust.2012.03.004

Szeto, M., Werdell, P. J., Moore, T. S., & Campbell, J. W. (2011). Are the world's oceans optically different? *Journal of Geophysical Research*, *116*, C00H04. http://doi.org/10.1029/2011JC007230

Thomson, R. E., Beamish, R. J., Beacham, T. D., Trudel, M., Whitfield, P. H., & Hourston, R. A. S. (2012). Anomalous Ocean Conditions May Explain the Recent Extreme Variability in Fraser River Sockeye Salmon Production. *Marine and Coastal Fisheries*, *4*(1), 415–437. http://doi.org/10.1080/19425120.2012.675985

Tilstone, G. H., Angel-Benavides, I. M., Pradhan, Y., Shutler, J. D., Groom, S., & Sathyendranath, S. (2011). An assessment of chlorophyll-a algorithms available for SeaWiFS in coastal and open areas of the Bay of Bengal and Arabian Sea. *Remote Sensing of Environment*, *115*(9), 2277–2291. http://doi.org/10.1016/j.rse.2011.04.028

Toole, D. A., & Siegel, D. A. (2001). Modes and mechanisms of ocean color variability in the Santa Barbara Channel. *Journal of Geophysical Research: Oceans (1978–2012)*, *106*(C11), 26985–27000.

Torrecilla, E., Stramski, D., Reynolds, R. A., Millán-Núñez, E., & Piera, J. (2011). Cluster analysis of hyperspectral optical data for discriminating phytoplankton pigment assemblages in the open ocean. *Remote Sensing of Environment*, *115*(10), 2578–2593.

Twardowski, M. S., Boss, E., Macdonald, J. B., Pegau, W. S., Barnard, A. H., & Zaneveld, J. R. V. (2001). A model for estimating bulk refractive index from the optical backscattering ratio and the implications for understanding particle composition in case I and case II waters. *Journal of Geophysical Research*, *106*(C7), 14129. http://doi.org/10.1029/2000JC000404

Twardowski, M. S., Boss, E., Sullivan, J. M., & Donaghay, P. L. (2004). Modeling the spectral shape of absorption by chromophoric dissolved organic matter. *Marine Chemistry*, *89*(1-4), 69–88. http://doi.org/10.1016/j.marchem.2004.02.008

Twardowski, M. S., & Donaghay, P. L. (2001). Separating in situ and terrigenous sources of absorption by dissolved materials in coastal waters. *Journal of Geophysical Research*, *106*(C2), 2545. http://doi.org/10.1029/1999JC000039

Twardowski, M. S., Sullivan, J. M., Donaghay, P. L., & Zaneveld, J. R. V. (1999). Microscale quantification of the absorption by dissolved and particulate material in coastal waters with an ac-9. *Journal of Atmospheric and Oceanic Technology*, *16*(6), 691–707.

Tzortziou, M., Subramaniam, A., Herman, J. R., Gallegos, C. L., Neale, P. J., & Harding, L. W. (2007). Remote sensing reflectance and inherent optical properties in the mid Chesapeake Bay. *Estuarine, Coastal and Shelf Science*, *72*(1-2), 16–32. http://doi.org/10.1016/j.ecss.2006.09.018

USGS. (2015). National Water Information System. Retrieved October 1, 2015, from http://waterdata.usgs.gov/

Vantrepotte, V., Loisel, H., Dessailly, D., & Mériaux, X. (2012). Optical classification of contrasted coastal waters. *Remote Sensing of Environment*, *123*, 306–323.

Vazyulya, S., Khrapko, A., Kopelevich, O., Burenkov, V., Eremina, T., & Isaev, A. (2014). Regional algorithms for the estimation of chlorophyll and suspended matter concentration in the Gulf of Finland from MODIS-Aqua satellite data. *Oceanologia, 56*(4), 737–756. http://doi.org/10.5697/oc.56-4.737

Verrelst, J., Muñoz, J., Alonso, L., Delegido, J., Rivera, J. P., Camps-Valls, G., & Moreno, J. (2012). Machine learning regression algorithms for biophysical parameter retrieval: Opportunities for Sentinel-2 and -3. *Remote Sensing of Environment, 118*, 127–139. http://doi.org/10.1016/j.rse.2011.11.002

Voss, M., Dippner, J. W., Humborg, C., Hürdler, J., Korth, F., Neumann, T., … Venohr, M. (2011). History and scenarios of future development of Baltic Sea eutrophication. *Estuarine, Coastal and Shelf Science*, *92*(3), 307–322. http://doi.org/10.1016/j.ecss.2010.12.037

Werdell, P. J. (2010). Ocean Color Chlorophyll (OC) v6. Retrieved August 6, 2015, from http://oceancolor.gsfc.nasa.gov/REPROCESSING/R2009/ocv6/

Werdell, P. J., Bailey, S. W., Franz, B. A., Harding Jr, L. W., Feldman, G. C., & McClain, C. R. (2009). Regional and seasonal variability of chlorophyll-a in Chesapeake Bay as observed by SeaWiFS and MODIS-Aqua. *Remote Sensing of Environment*, *113*(6), 1319–1330.

WET Labs. (2011). *Ac Meter Protocol*. Philomath, OR.

WET Labs. (2012). *ECO 3-Measurement Sensor User's Guide*. Philomath, OR.

Winter, D. F., Banse, K., & Anderson, G. C. (1975). The dynamics of phytoplankton blooms in puget sound a fjord in the Northwestern United States. *Marine Biology, 29*(2), 139–176. http://doi.org/10.1007/BF00388986

Wozniak, S. B., & Stramski, D. (2004). Modeling the Optical Properties of Mineral Particles Suspended in Seawater and their Influence on Ocean Reflectance and Chlorophyll Estimation from Remote Sensing Algorithms. *Applied Optics, 43*(17), 3489. http://doi.org/10.1364/AO.43.003489

Woźniak, S. B., Stramski, D., Stramska, M., Reynolds, R. A., Wright, V. M., Miksic, E. Y., … Cieplak, A. M. (2010). Optical variability of seawater in relation to particle concentration, composition, and size distribution in the nearshore marine environment at Imperial Beach, California. *Journal of Geophysical Research, 115*(C8), C08027. http://doi.org/10.1029/2009JC005554

Yacobi, Y. Z., Moses, W. J., Kaganovsky, S., Sulimani, B., Leavitt, B. C., & Gitelson, A.

A. (2011). NIR-red reflectance-based algorithms for chlorophyll-a estimation in mesotrophic inland and coastal waters: Lake Kinneret case study. *Water Research*, *45*(7), 2428–36. http://doi.org/10.1016/j.watres.2011.02.002

Yin, K., Goldblatt, R., Harrison, P., StJohn, M., Clifford, P., & Beamish, R. (1997). Importance of wind and river discharge in influencing nutrient dynamics and phytoplankton production in summer in the central Strait of Georgia. *Marine Ecology Progress Series*, *161*, 173–183. http://doi.org/10.3354/meps161173

Zhao, J., Temimi, M., & Ghedira, H. (2015). Characterization of harmful algal blooms (HABs) in the Arabian Gulf and the Sea of Oman using MERIS fluorescence data. *ISPRS Journal of Photogrammetry and Remote Sensing*, *101*, 125–136. http://doi.org/10.1016/j.isprsjprs.2014.12.010